CHALMERS
UNIVERSITY OF TECHNOLOGY

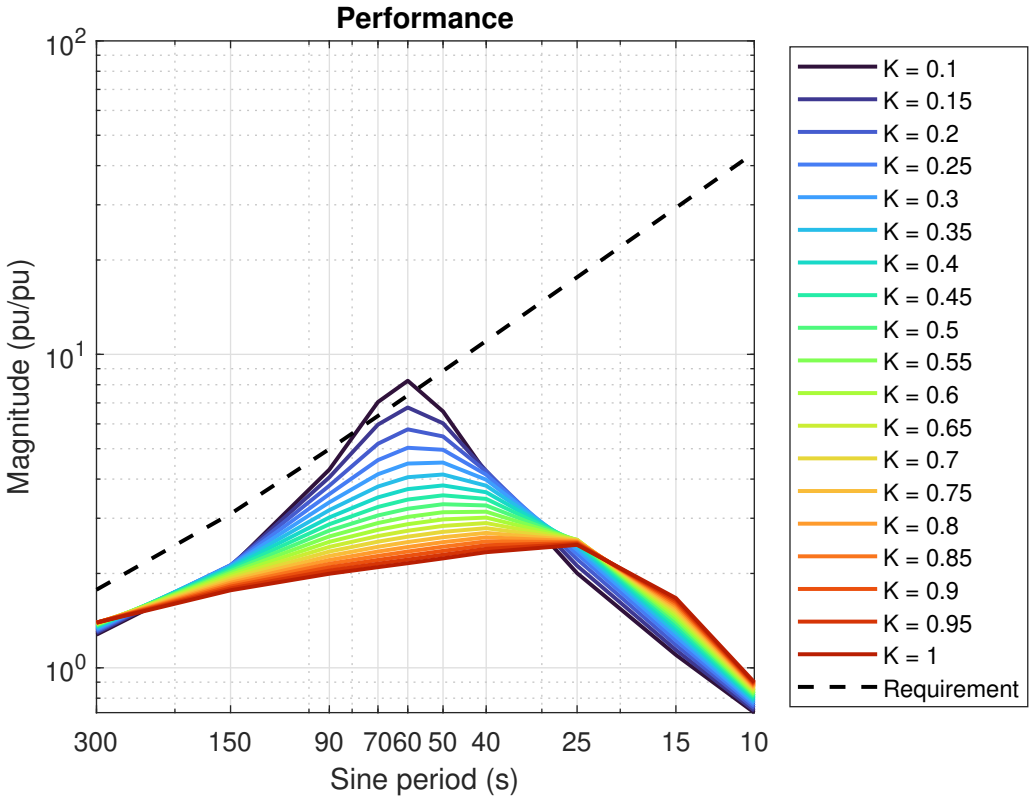

A Model for Simulating FCR Prequalification Tests for Kaplan Turbines

Master's thesis in Sustainable Electric Power Engineering and Electromobility

EDDIE ERIKSSON

DEPARTMENT OF ELECTRICAL ENGINEERING
CHALMERS UNIVERSITY OF TECHNOLOGY
Gothenburg, Sweden 2024
www.chalmers.se

Master's thesis 2024

A Model for Simulating FCR Prequalification Tests for Kaplan Turbines

EDDIE ERIKSSON

CHALMERS
UNIVERSITY OF TECHNOLOGY

Department of Electrical Engineering
Chalmers University of Technology
Gothenburg, Sweden 2024

A Model for Simulating FCR Prequalification Tests for Kaplan Turbines
EDDIE ERIKSSON

Supervisor: Christian Ekstrand, M.Sc.
Solvina AB
Examiner: Peiyuan Chen, Ph.D.
Department of Electrical Engineering

Master's thesis 2024
Department of Electrical Engineering
Division of Electric Power Engineering
Chalmers University of Technology
SE-412 96 Gothenburg
Sweden
Telephone +46 31 772 1000

Cover: The impact the FCR controller's proportional gain has on disturbance suppression. In the Nordic Synchronous Area, damping the 60 s oscillations is one of the key tasks of the primary frequency control. For further information, see Figure 4.32.

Typeset in LaTeX
Gothenburg, Sweden 2024

A Model for Simulating FCR Prequalification Tests for Kaplan Turbines
EDDIE ERIKSSON
Department of Electrical Engineering
Chalmers University of Technology

Abstract

A Kaplan turbine was modeled in Simulink with the purpose of simulating prequalification tests for Frequency Containment Reserve (FCR) provision, based on technical requirements for FCR introduced in 2023. The model did not successfully predict fulfillment of steady-state requirements, and was too optimistic in its prediction of fulfillment of dynamic requirements. However, all tests predicted to fail also failed in real-world tests, indicating a potential use case for ruling out Kaplan turbines not suitable for FCR provision. A sensitivity analysis showed that simulation results were mostly unaffected by runner servo parameters, indicating a flaw in the model. Compensation with a first order low-pass filter significantly improved the accuracy of simulated dynamics. However, several model parameters, including the time constant for the low-pass filter, needed real-world tests for estimation. This reduced the likelihood of achieving high simulation accuracy ahead of conducting real prequalification tests. Using the simulated prequalification tests, methods for improving performance were explored. Both tuning the FCR controllers and the servos controlling guide vanes and runner blades were shown to improve dynamic performance, but tuning the servos improved the stability margins more. An approach to active power feedback was introduced and resulted in perfect fulfillment of the steady-state requirements. The dynamic performance requirements were not affected much, but the stability margins were severely worsened due to larger control movements at higher frequencies. The results suggested that fulfilling all technical requirements for FCR will be very challenging for Kaplan turbines. However, with increased market participation from other sources, this will likely not lead to insufficient FCR capacity in the near future.

Keywords: Kaplan turbine, FCR, modeling, simulation, prequalification

Acknowledgements

This thesis was conducted at Solvina AB, using data from prequalification tests conducted by the company as a reference case. The validation of the model would not have been possible without this data.

I would like to thank my supervisor Christian Ekstrand for his continued guidance and support during this thesis. Your expertise and hands-on experience was instrumental in making this thesis into what it is today. I also want to thank the rest of my colleagues at Solvina for welcoming me into the workplace, and especially Victor Lidskog and Bengt Johansson for their insights and inspiring discussions.

A special thanks goes out to Michael Gratza, for providing the approximated turbine characteristic that became a key part of the model, and his very helpful explanation of its usage.

Finally, I want to thank my friends and family, and above all my girlfriend Tess, for supporting and bearing with me during these months.

Eddie Eriksson, Gothenburg, November 2024

List of Abbreviations

Below is the list of acronyms and abbreviations that have been used throughout this thesis listed in alphabetical order:

CIGRE	International Council on Large Electric Systems (Conseil international des grands réseaux électriques)
ENTSO-E	European Network of Transmission System Operators for Electricity
FCR	Frequency Containment Reserve
-D	-Disturbance
-N	-Normal
FFR	Fast Frequency Reserve
FME	Frequency Measurement Equipment
FRR	Frequency Restoration Reserve
HVDC	High Voltage Direct Current
IEEE	Institute of Electrical and Electronics Engineers
LER	Limited Energy Resource
LFSM	Limited Frequency Sensitive Mode
-O	Overfrequency
-U	Underfrequency
PFR	Primary Frequency Reserve
PID	Proportional - Integral - Derivative (controller)
RfG	Requirements for Generators
RoCoF	Rate of Change of Frequency
SRC	Standardized Regression Coefficient
SvK	Svenska Kraftnät
TSO	Transmission System Operator

Nomenclature

Below is the nomenclature of indices, sets, parameters, and variables that have been used throughout this thesis.

Variables

f	Grid frequency
$\bar{G}$	Equivalent gate opening
h	Hydraulic head
P	Active power
Q	Water flow
Y	Guide vane position/angle
α	Runner blade angle

Parameters

E_p	Droop
η	Turbine efficiency
h_{nom}	Nominal hydraulic head
K_p	Proportional gain
K_i	Integral gain
P_{nom}	Nominal power

Contents

List of Figures

List of Tables

1

Introduction

In this section, the background of the issue is presented. This is used to formulate research questions and define the scope of the thesis.

1.1 Background

In the Nordic Synchronous Area, ancillary services such as Frequency Containment Reserve (FCR) and Frequency Restoration Reserve (FRR) are used in order to maintain and restore the nominal grid frequency of 50 Hz. In Sweden, these services are procured by the Transmission System Operator (TSO) Svenska Kraftnät (SvK). SvK maintains a set of technical requirements for participation in frequency ancillary services, based on requirements for the Nordic Synchronous Area set by ENTSO-E. In order to participate in the ancillary service market, providers must perform a set of tests to prove they fulfill the technical requirements. Some, but not all of the requirements have reduction factors associated with them, meaning a unit can be prequalified with a lower capacity than planned. [1]

In 2023, the technical requirements for FCR-N, FCR-D up and FCR-D down were extended with new revised requirements [1]. Meanwhile, an increased market share of varying renewable power plants over the last decades has led to a higher demand for FCR services, traditionally provided by hydro power plants in Sweden [2]. The dynamic behavior of these power plants is complex, with e.g. nonlinear components, mechanical backlash and water dynamics. Therefore, hydro power plants, and in particular those with Kaplan turbines, one of the most common types of hydraulic turbines, characterized by their multiple actuators, may face difficulties in meeting both performance and stability requirements.

Performing prequalification tests is time-intensive, especially when extensive on-site re-tuning is required in order to meet the technical requirements. Therefore, in order to better understand the dynamics of Kaplan turbines, predict which hydro power plants are suitable for FCR provision, and facilitate controller tuning, a simulation model for Kaplan turbines is desirable. In addition, such a model could be useful for demonstrating the impact of controller parameters in these nonlinear systems with many non-ideal behaviors during FCR prequalification and delivery.

1.1.1 Previous Work

There exist several models of hydro power turbines in the literature. For controller design, a linear or linearized model is often used [3], [4]. Saarinen et al. evaluated commonly used linear models against measurements on real turbines and discussed shortcomings in the models [5]. The linear models were not suitable for detailed analysis of individual hydraulic turbines, but described the behavior of three turbines significantly better when the nonlinear phenomenon backlash was modeled. For accurate time-domain simulation, nonlinearities are taken into consideration. Brezovec et al. modeled a Kaplan turbine using polynomial fitting of index tests [6]. Dahlborg et al. used a similar approach to model Kaplan turbines for large grid disturbances in a strong grid, denoting it a 'white-box' model. The model was found to be more accurate than commonly used 'gray-box' models (from [7] and [8]), but needed extensive data since the model was fitted to measurements from index tests, rather than constructed with explicit differential equations [9]. 'Index tests' refers to measurements relating water flow, active power, pressure, and efficiency to guide vane position and runner blade angle. Gratza et al. used Computational Fluid Dynamics (CFD) simulations in place of index tests to model island operation of a Kaplan turbine [10].

The combination, or 'cam', relationship between Kaplan turbines' guide vane opening and runner blade angle has been a subject for some research. Traditionally, the relationship has been found empirically in order to maximize efficiency. Gustafsson explored offsetting the combination curve from the efficiency combination in order to improve stability during island operation [11]. Gratza et al. used a similar approach to improve the dynamic response of a simulated Kaplan turbine, also during island operation [10].

The allocation of frequency control resources has also been studied. Saarinen et al. compared FCR and FRR allocation between Francis and Kaplan turbines in terms of wear and tear, efficiency, and frequency quality [12]. They found Kaplan turbines to be less suitable for FCR than Francis turbines due to their slow runner dynamics, but more suitable for FRR because of their flatter efficiency curves, i.e. efficient operation over larger intervals of operating points. Backlash was also found to strongly affect the results. In the design process of the FCR technical requirements, the goal of improving the response from individual units needed to be balanced against the need for sufficiently many hydro power plants to qualify, in order to meet the overarching objective of improving frequency quality [13]–[16]. Units with high backlash and/or high water time constants were especially problematic. Appelstål and Lindgren respectively studied the technical [17] and economic [18] potential for introducing other technologies than hydro power for frequency control in the Swedish power system. Demand side flexibility, for instance in household heat pumps, was shown to have both technical and economic potential for FCR provision. As of October 2024, hydro power plants are still the largest provider of all types of FCR, along with some notable contribution from wind power, energy storage systems, and demand flexibility [19].

1.2 Research Questions

The main goal of the thesis was to build a simulation model of a Kaplan turbine, suitable for simulation of FCR operation and prequalification for FCR-N and FCR-D. This model was to be general enough that it could be used to simulate various Kaplan turbines with appropriate parameters. The simulated unit's performance was to be evaluated against the FCR technical requirements automatically.

> *Research Question 1: Can a simulation model, accurate enough to predict fulfillment of the technical requirements, be built using parameters obtainable before conducting actual tests?*

Using the model, control improvements were to be explored. Part of the motivation for building a simulation model was to be able to perform controller tuning in advance. Beyond the FCR controllers themselves, it was desirable to examine other methods for improving FCR performance and fulfillment of the technical requirements.

> *Research Question 2: What improvements can be made to the control of the unit, in order to fulfill the technical requirements?*

Fulfilling all technical requirements was expected to be challenging for a Kaplan turbine. Besides performing preliminary tuning, it would be helpful to predict which units can prequalify at all. Kaplan turbines make up approximately 6 GW of installed capacity in Sweden, out of 16.4 GW of installed hydro capacity in total. [13], [20].

> *Research Question 3: Are Kaplan turbines in general suitable for providing FCR?*

Societal, ecological, and ethical considerations were to be examined.

> *Research Question 4: Are there any ecological consequences of altering FCR behavior, for example due to increased variations in water flow? Are there any consequences for the adoption of renewable energy sources if many hydro units equipped with Kaplan turbines can not provide FCR?*

1.3 Limitations

This thesis focuses on FCR operation of Kaplan turbines. If the runner pitch setting is kept constant, the same model may also be valid for Francis turbines [9], though that is not the primary purpose of the thesis. In particular, the model to be built should be valid under the conditions in [1], as one of its primary purposes is to simulate FCR prequalification. Therefore, other operation modes and frequency ranges will not be addressed in depth. Measurements come primarily from prequalification tests, so validation was naturally limited to this kind of operation.

The thesis work will not address the ecological impact of hydro power as a whole. However, it may be relevant to discuss aspects related to FCR operation.

The premise of the thesis is based on Swedish conditions and regulations as of

October 2024. Other countries' implementations of primary frequency control and their respective regulations and requirements are therefore not treated in this work.

Reduction factors in the technical requirements are not considered extensively, since they are more a matter of regulation technicalities and give little information about model fidelity.

Wear and tear is not considered as an optimization variable for tuning.

2

Frequency Reserves and Hydraulic Turbines

In this chapter, a theoretical background is introduced so the methods and results can be better understood.

2.1 The Per-Unit System

Throughout this thesis, many variables and parameters are in per-unit (pu). This is a standard way of normalizing variables in electric power engineering, defined simply by:

$$\bar{X} = \frac{X}{X_{\text{base}}}, \tag{2.1}$$

where X is some variable in actual units, $\bar{X}$ is the same variable in per-unit, and X_{base} is the per-unit base of the variable. The per-unit base can be defined by a nominal value, such as P_{nom} for a hydraulic turbine; range of possible values, such as for guide vane angle; or arbitrarily, for example S_{base} in power system studies.

2.2 Power System Stability

Several different phenomena affect the stability of power systems on different time scales. In this thesis, the definitions introduced by the IEEE/CIGRE Joint Task Force on Stability Terms and Definitions [21] are used. The main categories of power system stability are presented here. Rotor angle stability is the ability of synchronous generators to stay synchronized to the grid in the event of a small ("Small Signal Stability") or large ("Transient Stability") disturbance. Voltage stability is the ability to maintain stable voltage levels (magnitudes) within safe limits in all buses of the network, following a disturbance. Frequency stability is the ability to maintain the system frequency following a large disturbance.

All three categories of power system stability are, as noted in [21], to a degree coupled, especially in stressed conditions. However, they are analyzed in different ways and for control purposes they can often be considered as separate phenomena. Importantly for this thesis, voltage control is primarily a matter of reactive power control, while frequency control is performed by adjusting the active power balance [22]. Further, voltage is a local phenomenon while frequency is global across the

entire synchronous area, meaning the active power balance can be aggregated for the grid as a whole. This also means frequency control for the whole grid can be performed in a distributed manner.

This thesis is concerned with frequency control and thus active power is the variable to be controlled. The relationship between active power and frequency can be derived from the swing equation (2.2). It simply states that if the mechanical torque supplied to a synchronous machine is larger than the electrical torque, the machine will accelerate and thus the frequency will increase. The following derivation is adapted from [22].

$$J\frac{d\omega_r}{dt} = T_\mathrm{m} - T_\mathrm{e}. \tag{2.2}$$

Multiplying both sides with the speed ω_r changes the relationship to be in terms of power rather than torque (2.3). P_m here is understood as mechanical power supplied to generators and P_e as the electrical load. The differential equation is now nonlinear.

$$J\frac{d\omega_r}{dt}\omega_r = P_\mathrm{m} - P_\mathrm{e}. \tag{2.3}$$

We introduce the inertia constant H [MWs/MVA] which relates the kinetic energy stored in the rotating mass of the machine at synchronous speed to the apparent power base (2.4). We can then define the moment of inertia J using the inertia constant.

$$H = \frac{J\omega_0^2}{2S_n} \Rightarrow J = \frac{2HS_n}{\omega_0^2}. \tag{2.4}$$

Plugging in this expression for J and rearranging the equation we get (2.5) and (2.6).

$$2HS_n\frac{d\frac{\omega_r}{\omega_0}}{dt}\frac{\omega_r}{\omega_0} = P_\mathrm{m} - P_\mathrm{e}. \tag{2.5}$$

$$2H\frac{d\frac{\omega_r}{\omega_0}}{dt}\frac{\omega_r}{\omega_0} = \frac{P_\mathrm{m} - P_\mathrm{e}}{S_n}. \tag{2.6}$$

In the equation we now have speed and power divided by their respective base values, which can be replaced with per-unit (normalized) variables. Here, the bar denotes a per-unit variable. The equation in per-unit is seen in (2.7).

$$2H\frac{d\bar{\omega}_r}{dt}\bar{\omega}_r = \bar{P}_\mathrm{m} - \bar{P}_\mathrm{e}. \tag{2.7}$$

The equation is still nonlinear. We can use the fact that the frequency deviates relatively little from the nominal value during grid connected operation (2.8) and that production and consumption are in balance at an operating point (2.9) in order to perform a first order Taylor expansion around the operating point. The resulting linearized equation is (2.10).

$$\bar{f} = \bar{\omega}_r \approx 1. \tag{2.8}$$

$$\bar{P}_\mathrm{m0} = \bar{P}_\mathrm{e0}. \tag{2.9}$$

$$2H\frac{d\Delta\bar{f}}{dt} = \Delta\bar{P}_\mathrm{m} - \Delta\bar{P}_\mathrm{e}. \tag{2.10}$$

Finally, some loads such as synchronous machines driving constant torque mechanical loads have a linear dependence between frequency and active power, denoted here by D. In (2.11), this corresponds to speed dependent damping.

$$2H\frac{d\Delta\bar{f}}{dt} = \Delta\bar{P}_{\mathrm{m}} - \Delta\bar{P}_{\mathrm{e}} - D\Delta\bar{f}. \tag{2.11}$$

In frequency stability analysis, either (2.10) or (2.11) is called the linearized swing equation. It can be scaled to take an entire grid into account, by summing the power bases S_n and using a weighted sum of the connected synchronous machines' inertia constants H. In the equation, $\Delta\bar{P}_{\mathrm{m}}$ is seen as the (controllable) change in active power output from synchronous generators, $\Delta\bar{P}_{\mathrm{e}}$ as the size of a disturbance and $\Delta\bar{f}$ as the frequency deviation. The derivative of Δf is often referred to as Rate of Change of Frequency (RoCoF), commonly expressed in Hz/s rather than pu/s. In the Laplace domain, the transfer function of the grid is expressed as in (2.12).

$$G(s) = \frac{\Delta\bar{f}(s)}{\Delta\bar{P}_{\mathrm{m}}(s) - \Delta\bar{P}_{\mathrm{e}}(s)} = \frac{1}{2Hs + D}. \tag{2.12}$$

The frequency needs to be maintained in a narrow band around the nominal frequency. In the Nordic Synchronous Area, 49.9 Hz to 50.1 Hz is considered the normal frequency band. Too large deviations in frequency may cause some loads to amplify the deviation, drive resonances in thermal power plants and trip protection devices, resulting in even larger disturbances.

2.2.1 Frequency Reserves

The electricity markets Elspot (day-ahead) and Elbas (intraday) make sure that production is approximately equal to demand in the Nordic grid [23]. However, variations in loads and production occur continuously, causing imbalances. Disturbances in the power system balance may also be caused by large losses of production or loads, such as tripping of nuclear plants or malfunctioning HVDC lines. In order to keep the grid balanced, Nordic TSOs procure ancillary services for frequency control. In the Nordic system, FCR-N, FCR-D, aFRR and mFRR are the ancillary frequency services used [24]. There are also some reserves not classified as ancillary services, e.g. FFR and LFSM.

FCR-N stands for Frequency Containment Reserve, Normal operation [25]. Its purpose is to handle the normal variations in production and demand, caused by e.g. wind and load forecast errors, in order to keep the frequency in the normal operating band. FCR-D (Disturbance) is only activated when the frequency goes outside the normal band, during larger disturbances [26], [27]. FCR is activated according to measured frequency deviations and does not require control signals from SvK. In an international context, FCR is a type of primary frequency reserve [28].

The products aFRR and mFRR stand for automatic and manual Frequency Restoration Reserve [24]. The purpose of aFRR is to bring the frequency back to its nominal value. This is done automatically with control signals being generated centrally. On the other hand, mFRR is activated manually on request from SvK. The main use

of mFRR is to free up capacity in other reserves and restore the power flow to pre-disturbance values. In an international context, aFRR is counted as a secondary reserve while mFRR is counted as a tertiary reserve [28].

In Figure 2.1, a typical sequence during a grid frequency disturbance is seen. The FCR providers automatically respond to the disturbance and limit the frequency deviation. The point where the maximum deviation occurs is called the frequency nadir, zenith for positive deviations. After a delay, aFRR is activated and starts to free up the capacity of the FCR units. Later still mFRR is activated to fully restore the frequency, restore pre-disturbance power transmission between price zones, and free up the other reserves. The time axis is not to scale. FCR mitigates the disturbance within seconds, while the FRR units will be fully activated after several minutes.

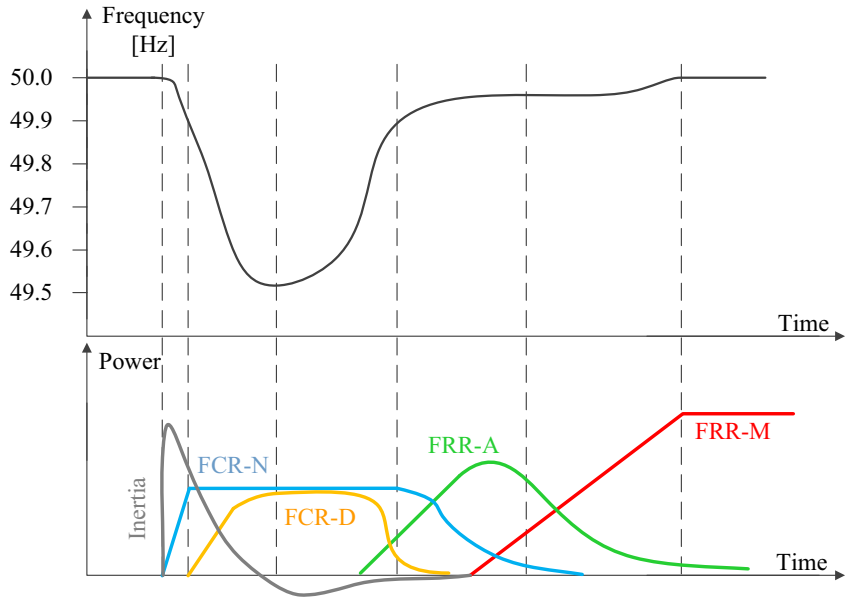

Figure 2.1: A sketch representing frequency regulation support strategies during a fictive frequency dip in the Nordic power system. (M. Persson, "Frequency Response by Wind Farms in Power Systems with High Wind Power Penetration," Chalmers University of Technology, Gothenburg, Sweden, Ph.D. dissertation, 2017. [28]). Used with permission.

Beyond ancillary services, the regulation Requirements for Generators (RfG) [29] mandates some power plants to participate in Limited Frequency Sensitive Mode (LFSM). This frequency reserve is activated outside the FCR operating bands, but behaves in the same way. Producers that do not participate in the FCR market may also be ordered to provide Frequency Sensitive Mode (FSM), equivalent to FCR-D.

As a mitigation for decreased inertia in the power system, for example when large conventional power plants are disconnected for maintenance during the summer, FFR (Fast Frequency Reserve) was introduced [30]. It is activated in a stepwise manner for large frequency deviations. Units providing FFR are required to activate

fully within around 1 s, depending on activation threshold. It is thus the fastest frequency reserve in the Nordic system.

2.2.1.1 Droop

An important aspect of primary frequency control is droop (E_p), which determines the steady-state behavior of a power plant participating in FCR. With nonzero droop, the controller does not completely remove the error. Rather, steady-state power output is proportional to the frequency error. Droop is commonly expressed in Hz/MW, or pu/pu (often shown as %) in the per-unit system. The inverse of droop is called regulating strength (MW/Hz). Ideally, an FCR provider's capacity and therefore bid size is proportional to the regulating strength, and its response linear with respect to Δf.

Besides quantifying the FCR capacity, droop is needed to share the load of frequency control between power plants. With droop, imbalances in the grid are compensated evenly between FCR providers according to their own regulating strengths.

As mentioned above, the objective of droop is to scale steady state power output proportionally to frequency error. Indeed, the simplest implementation of droop is to just have a proportional controller. However, the dynamics of hydro turbines would lead to poor stability if using a proportional-only controller [31]. Further, the dynamic response and droop cannot be changed independently of each other, making controller tuning for a specific capacity impossible.

Droop determines the steady-state active power response for a given frequency deviation. However, in practice it is often the controller output or guide vane position that is fed back to the controller. This is done mainly because the control action is prone to counteracting the inertial response of a synchronous generator when power feedback is used [1], [31], [32]. However, since the power is not exactly linearly dependent on the guide vane setting, this will not result in an entirely linear response. Because of this, SvK recommends using some type of gain scheduling or combination of power feedback and guide vane feedback to achieve correct droop.

2.3 Control Theory

In this section, control theory relevant to this thesis is presented. These are the basics used to define some of the technical requirements, described further in Appendix A.

A simple example of a control system with negative feedback, describing frequency control, is seen in Figure 2.2. There is a controller $F(s)$ (FCR providers) and a process $G(s)$ (the swing equation of the grid). Disturbances are added to the control signal ΔP (change in active power) and the process variable $\Delta \bar{f}$ (frequency deviation). A few transfer functions can be constructed in order to characterize the behavior of the closed loop system. For simplicity, the system contains no unstable poles.

Open loop transfer function: Defined as $G_o(s) = F(s)G(s)$. Describes the behavior of the open loop system obtained if the feedback is cut off, from e to

$\Delta\bar{f}$.

Closed loop transfer function: Defined as $T(s) = \frac{L(s)}{L(s)+1}$. Describes the behavior of the closed loop system from $\Delta\bar{f}^*$ to $\Delta\bar{f}$, and the sensitivity to measurement errors.

Sensitivity function: The closed loop transfer function from d_f to $\Delta\bar{f}$, defined as $S(s) = \frac{1}{L(s)+1}$.

Disturbance suppression: The closed loop transfer function from d_P to $\Delta\bar{f}$, defined as $G_c(s) = S(s)G(S) = \frac{G(s)}{L(s)+1}$.

The Nyquist curve is obtained by plotting the real and imaginary part of $G_o(s)$ in the complex plane. For our simple system, the closed loop system $T(s)$ is stable if the Nyquist curve passes to the right of -1. The minimum distance from the Nyquist curve to $(-1 + j0)$, R, is in turn related to the sensitivity function in that it is the inverse of the peak sensitivity:

$$\frac{1}{R} = \max_{\omega} |S(j\omega)|. \tag{2.13}$$

$G_c(s)$ is also known as the input sensitivity function. It describes how disturbances affect the process variable. Like for the sensitivity function, smaller values imply a system less sensitive to disturbances, but added to the input ΔP rather than the process variable $\Delta\bar{f}$.

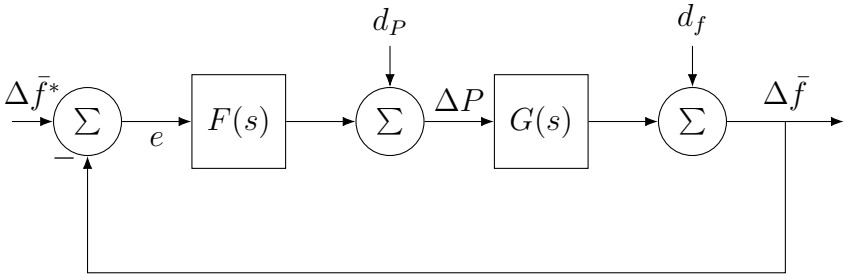

Figure 2.2: Block diagram of the closed loop frequency control system.

2.3.1 PI Controller with Droop

One of the most commonly used controllers is the PI controller, with proportional and integral action. The proportional part provides an immediate response to errors while the integral part drives the error to zero in steady state. If droop is added, like in Figure 2.3, the output of the controller is instead proportional to the error in steady state.

The transfer function of the PI controller with droop shown in Figure 2.3 is

$$\frac{K_p s + K_i}{(E_p K_p + 1)s + E_p}. \tag{2.14}$$

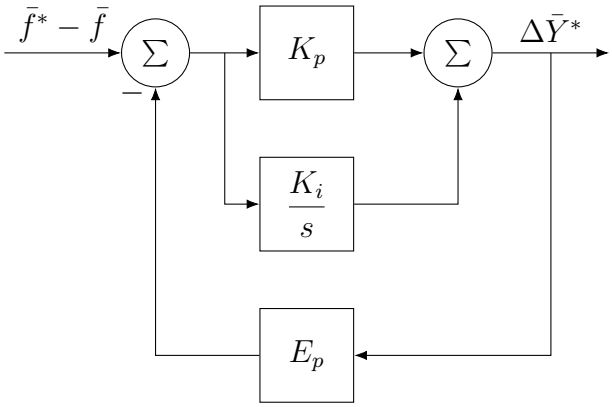

Figure 2.3: Block diagram of the PI controller with droop for frequency control. The asterisk (*) denotes a setpoint.

The dynamic behavior of this controller changes with droop. However, if the parameters are scaled with droop [31] such that

$$\begin{cases} K_p = \dfrac{K}{E_p} \\ K_i = \dfrac{1}{E_p \cdot T_{\text{feedback}}} \end{cases} \tag{2.15}$$

where K and T_{feedback} are droop independent parameters, the transfer function becomes:

$$\begin{aligned} &\frac{\frac{K}{E_p}s + \frac{1}{E_p \cdot T_{\text{feedback}}}}{(E_p\frac{K}{E_p} + 1)s + E_p\frac{1}{E_p \cdot T_{\text{feedback}}}} \\ =&\frac{\frac{1}{E_p}\left(Ks + \frac{1}{T_{\text{feedback}}}\right)}{(K+1)s + \frac{1}{T_{\text{feedback}}}} \\ =&\frac{1}{E_p}\frac{KT_{\text{feedback}}s + 1}{(K+1)T_{\text{feedback}}s + 1}. \end{aligned} \tag{2.16}$$

From this we see that the steady state gain is dictated by the droop and that the dynamic behavior is dictated by K and T_{feedback}. If K is set to zero, the controller becomes a first order low-pass filter, and if T_{feedback} is set to zero (or if $K \to \infty$) the controller becomes purely proportional.

The advantage of using a scaled controller like the one presented here is that the steady-state and transient behaviors of the controller can be changed independently from each other. Thus the behavior stays the same, just scaled, for different droops if the design parameters K and T_{feedback} are constant. This can be further studied in Figures 23–26 in [31].

2.4 Frequency Containment Reserve

This thesis focuses on the operation and prequalification of FCR units. FCR takes the role of primary frequency reserves in the Nordic system. This section provides

information on the differences and similarities between FCR-N and FCR-D, as well as the prequalification process.

2.4.1 FCR-N

The Frequency Containment Reserve for Normal operation is always active. The volume of FCR-N procured is based on an estimation of normal fluctuations in the grid and is currently sized to 600 MW in Sweden [28]. FCR-N is a symmetrical product, so providers must reserve capacity in both directions when placing bids [25]. The bidding takes place until the day before delivery. Providers are compensated for procured capacity according to the marginal price since February 2024. Activated energy is compensated according to the marginal price of up- or down regulating energy, depending on the net direction of activation during the hour of operation.

FCR-N is activated linearly for frequencies between 49.9 Hz and 50.1 Hz [25], and is therefore saturated for larger frequency deviations. The FCR-N provider must have an endurance of one hour at full activation.

2.4.2 FCR-D

The volume of FCR-D to be procured depends on the largest single point of failure, called the dimensioning incident, 1400 MW (downwards) or 1450 MW (upwards) in Sweden [1], [28]. Unlike FCR-N, FCR-D is separated into two products for the upward and downward directions. Providers are compensated for procured capacity according to the marginal price, but are not compensated for activated energy [25], [27].

Downward FCR-D is activated linearly for frequencies from 50.1 Hz to 50.5 Hz [26]. If a provider is required to provide LFSM, but does not have a separate controller for LFSM-O, the downward FCR-D controller must not saturate at 50.5 Hz [1]. FCR-D providers are required to be able to sustain 100% activation for 20 minutes. Upward FCR-D and LFSM-U work the same way, but for equivalent negative frequency deviations [27].

Entities that are not able to linearly scale their activation, such as switched loads, may partake in static FCR-D [26], [27]. For stability reasons and other issues, the volume of procured static FCR-D is limited.

2.4.3 Prequalification

In order to participate in the FCR market, providers must go through prequalification in order to prove that their plant is suitable for FCR provision. The requirements are specified for both performance and stability measures, in both time and frequency domains. This section is a brief summary of the tests described in [1], and unless otherwise stated all information is taken from there. A more in-depth explanation of the tests and requirements is found in Appendix A. Specific rules and tests for static FCR and Limited Energy Reservoirs (LERs) will not be discussed here,

since those are not relevant for Kaplan turbines or hydro power units in general. The section mainly focuses on requirements that are quantified and measurable.

The prequalification tests are performed while the unit is synchronously connected to the grid. The frequency measurement for the FCR controller is overridden, either by generating a signal within the control system or by generating a signal externally and feeding it to the Frequency Measurement Equipment (FME). For each test, the frequency signal to be injected is specified in [1]. The active power response is measured and compared to required values. Thus the only variables that are needed to evaluate the technical requirements are frequency and active power. It can be noted that since the frequency signal is fictive, no inertial response is seen during prequalification.

Many of the tests allow for a reduction factor in case the requirement is not met. These tests are related to Requirements 1, 2, 3, and 9, and are explained in Appendix A. Requirements 4, 8, and 10 are not subject to reduction factors.

The FCR-N step tests and FCR-D ramp tests are each performed with different combinations of load (generated power before activation of FCR) and droop, in order to qualify the unit for a range of loading conditions and for different FCR capacities. These are seen in Table 2.1.

Table 2.1: Combinations of loading and droop. Low and high load can typically be near the endpoints of the unit's operating range, which differ between power plants. Droop (expressed in pu/pu) is mandated by RfG [29] to be between 2% and 12% for FSM and LFSM, and similar values are typical for FCR.

No.	Load	Droop
1	Low	Low
2	Low	High
3	High	Low
4	High	High

2.4.3.1 FCR-N Step Tests

During the step tests, the frequency signal is stepped between 49.9 Hz and 50.1 Hz in order to measure the steady state activation of the unit and test it against Requirement 1. Some deviation from the theoretical activation is allowed: 5% in the direction of under-delivery and 20% in the direction of over-delivery. That is, for a negative (positive) frequency deviation, the change in power should be positive (negative), at least 95% and at most 120% of the theoretical capacity.

2.4.3.2 FCR-D Ramp Tests

The ramp sequences for FCR-D contain three types of tests:

1. Steady state activation
2. Fast ramp

3. Deactivation

Steady state activation is tested for FCR-D, comparing active power when the frequency signal is 49.5 Hz or 50.5 Hz against the baseline power at 50 Hz. It is also tested for the combination of FCR-D and FCR-N, at 49.89 Hz or 50.11 Hz. These measurements also fall under Requirement 1, and have the same limits as FCR-N in terms of over- and under-delivery.

During a fast ramp, the fifth ramp of the injected frequency signal, active power is evaluated 7.5 s after the start of the ramp. The deviation from pre-ramp power is also integrated to obtain activated energy 7.5 s after the start of the ramp. The activated power and energy are evaluated against Requirement 2 and Requirement 3, respectively.

The deactivation test contains a frequency signal that mimics the grid frequency during a large disturbance. The test evaluates the unit's ability to reduce its activation when the frequency starts returning to normal, which is needed to avoid overshoot. This is done by integrating activated power exceeding (in absolute terms) a certain threshold after the frequency nadir or zenith, until the activation returns below that threshold. The result, here called 'overshoot energy', must not exceed the value defined by Requirement 4.

During the fast ramp and deactivation tests, the unit switches from stability mode to performance mode, if it has one. The performance mode is not subject to the stability requirement described below, but may only be activated for short periods of time. This allows for a faster response during large disturbances. Allowing this was one of the compromises of the design of the new requirements [15].

If the unit is required by RfG to provide LFSM, the LFSM controllers must be active during the FCR-D ramp tests.

2.4.3.3 Sine Tests

When studying the unit's response in the frequency domain, confusion may arise from the fact that the grid frequency has a frequency (see the title of [2]). In order to distinguish between the two frequencies, 'frequency' here refers to the grid frequency (real or simulated), while the frequency with which it oscillates is referred to by its inverse, 'sine period', where $\omega = 2\pi/T_{\text{sine}}$.

During sine tests, the injected frequency oscillates sinusoidally around a center frequency (49.7 Hz, 50 Hz, or 50.3 Hz depending on product) and a sine is fitted to the units active power response. From the amplitude and phase delay, an estimation of the unit's transfer function $F(j\omega)$ is formed at the tested sine periods. $F(j\omega)$ is scaled to represent all FCR capacity in the grid for the relevant product.

Together with the transfer function of the grid $G(j\omega)$ from (2.12), $F(j\omega)$ is used to calculate the open loop transfer function $G_o(j\omega)$ and the input sensitivity function $G_c(j\omega)$. The open loop transfer function is used to construct Nyquist plots and find the stability margin R, while the input sensitivity function is used to evaluate disturbance suppression, referred to as 'performance' by SvK. The stability margin is evaluated against Requirement 8, and the disturbance suppression/performance

is evaluated against a disturbance profile defined by Requirement 9.

The linearity of the units response is tested by calculating the root mean square error of the fitted sine, normalized with the standard deviation of the fitted sine. This value may not be higher than 1, as per Requirement 10.

2.5 Hydraulic Turbines

The working principle of a Kaplan turbine, or any type of hydro turbine, is to convert the mechanical energy of flowing water into rotation on a shaft connected to a generator. A simplified layout of a hydroelectric power plant can be seen in Figure 2.4. The power available for extraction can be expressed as:

$$P = \eta \cdot \rho \cdot g \cdot h \cdot Q, \tag{2.17}$$

where η is hydraulic efficiency, ρ is the density of water, g is the gravitational acceleration, h is the effective head and Q is the flow of water [22]. The effective head contains both components from the kinetic energy of moving water and the static pressure difference due to the height difference between the headrace and tailrace surfaces (hydraulic head). In Figure 2.4, this height difference is seen between the surface in the upstream reservoir and the downstream river. The efficiency varies depending on operating conditions. When building a hydroelectric power plant one of the main considerations is to pick a turbine suitable for the head and flow available at the site.

In per-unit notation, (2.17) is written as

$$\bar{P} = \eta \bar{h} \bar{Q}. \tag{2.18}$$

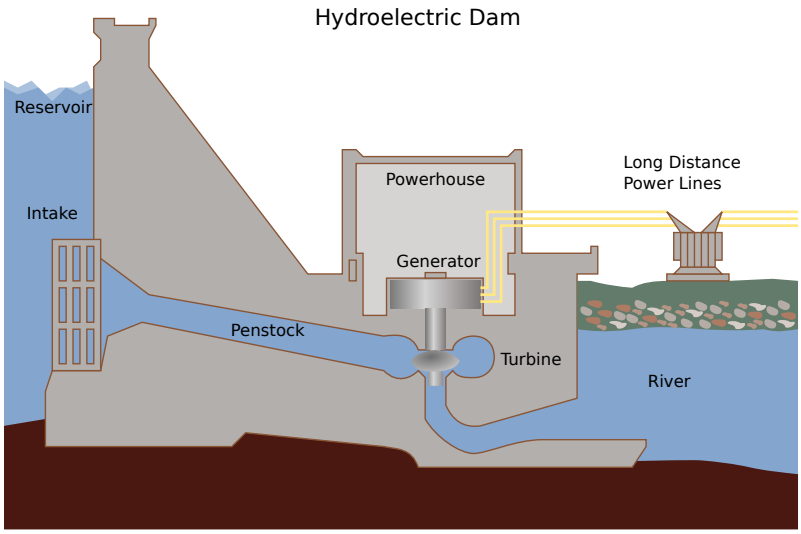

Figure 2.4: Schematic diagram of Hydroelectric power plant (Tennessee Valley Authority; SVG version by Tomia, CC BY-SA 3.0, via Wikimedia Commons [33]).

An important part of a hydro power unit's dynamics is determined by the waterways, or penstock [22]. The water time constant or water starting time is denoted T_W and is proportional to L/A where L is the length and A is the cross-section area of the penstock tube. When the guide vane position is changed, the flow of water does not change instantaneously since it has inertia, but pressure (equal to head in the per-unit system) does according to

$$\bar{h} = \left(\frac{\bar{Q}}{\bar{G}}\right)^2, \tag{2.19}$$

where $\bar{G}$ is called 'ideal gate opening' in [22], and represents the guide vane position compensated for losses. Note that opening the guide vanes results in decreased pressure and vice versa due to the inertia of the water column. The change in pressure then causes the water to accelerate according to

$$\frac{d\bar{Q}}{dt} = -\frac{1}{T_W}(\bar{h} - \bar{h}_0), \tag{2.20}$$

where $\bar{h}_0$ is the initial head. Initially, the pressure change causes the power to change in the opposite direction of the guide vanes according to (2.18). The effect is stronger the longer it takes for the water to accelerate, i.e. for larger T_W. The dynamics of the waterways lead to non-minimum phase behavior.

2.5.1 Kaplan Turbine

The Kaplan turbine was invented by the Austrian engineer Viktor Kaplan in 1913 [34]. The design was developed because of limitations in the Francis turbine, and introduced some significant changes [35]. The most important change was the introduction of variable pitch runner blades, which allowed for efficient operation across a larger range of water flow. Further, the water only flows axially in a Kaplan turbine (see Figure 2.5), as opposed to the Francis turbine where water enters radially and exits axially (Figure 2.6). This rendered the Kaplan turbine a pure reaction type turbine. As a consequence of the changes, the Kaplan turbine was much better suited for hydropower plants with low heads and large flows than previous designs.

The properties of the Kaplan turbine made it appealing for Swedish power plants, where heads are relatively low [35]. In fact, the first hydroelectric power plant to use a Kaplan turbine was Lilla Edet in Sweden, which opened in 1926 [38]. The turbine showed high efficiency over a large part of its operating range, thus proving the viability of the new technology [35]. Since then many Kaplan and Kaplan-derived turbines have been built in Sweden, with the type being one of the most common.

The pitch of the runner blades is set according to the position of the guide vanes in order to maximize efficiency [35]. The combination is found empirically, using what is sometimes called index tests [9]. In the first versions the combination was done using a mechanical cam connected to the guide vanes, i.e. the runner blade servo was mechanically connected to the guide vanes. Modern turbines use separate combination units where other conditions such as changes in head can be factored into the runner servo setpoint.

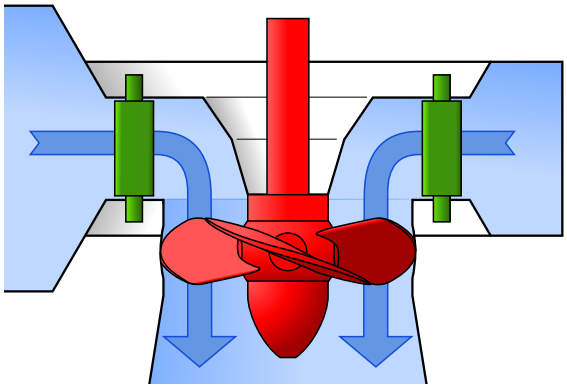

Figure 2.5: Sketch of a Kaplan turbine (Jahobr, CC0, via Wikimedia Commons [36]).

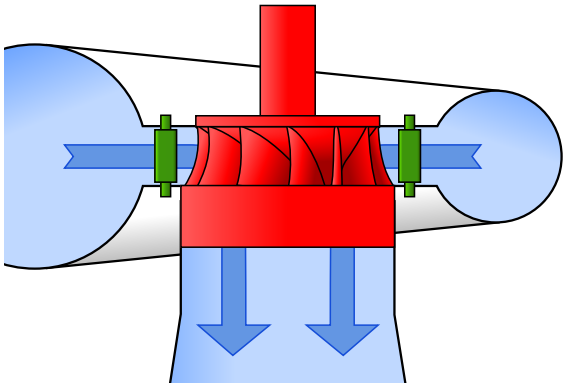

Figure 2.6: Sketch of a Francis turbine (Jahobr, CC0, via Wikimedia Commons [37]).

2.6 Sensitivity Analysis

The purpose of sensitivity analysis is to quantify the effects of varying model inputs x on model output $y(x)$ [39]. The analysis yields the relative importance of model inputs, which can then aid variable selection, i.e. whether a variable has a significant effect on an output or not.

There are many methods for performing a sensitivity analysis. Presented here is a method based on regression modeling, described in [39]. The method works well where a first order linear model can be fitted to the input-output data and where the inputs are independent from each other. The method is most commonly used for global sensitivity analysis, meaning the inputs are varied across their entire domains rather than a small interval near their nominal values.

For an input $x \in \mathbb{R}^d$, where d is the number of elements in x, sampled over n_s simulations, a standardized input x^* is defined as:

$$x^*_{i,j} = \frac{x_{i,j} - \bar{x}_j}{s_j}, \quad 1 \leq i \leq n_s, \quad 1 \leq j \leq d, \tag{2.21}$$

where $\bar{x}_j$ is the sample mean and s_j is the sample standard deviation of $x_{1,j}, \ldots, x_{d,j}$. The standardized output y^* is defined in the same manner. Then a first order model of the form

$$y^* = \beta_0^* + \beta_1^* x_1^* + \ldots + \beta_d^* x_d^* \tag{2.22}$$

is fitted. The coefficients β_j^* are known as the standardized regression coefficients (SRCs). Due to the standardization, β_j^* represents the change in the standardized output y^* when the j:th element of the input is changed one standard deviation. Thus, the domain of the inputs must be chosen on a relevant scale. The model output is more sensitive to inputs with larger SRCs.

The goodness of fit for the regression model can be checked with the coefficient of determination, r^2. It is defined here as:

$$r^2 = 1 - \frac{\text{sum of squares of residuals}}{\text{total sum of squares}} = 1 - \frac{\sum_{i=1}^{n_s}(y_i^* - \hat{y}_i^*)}{\sum_{i=1}^{n_s}(y_i^* - \bar{y}^*)}, \tag{2.23}$$

where $\hat{y}^*$ is the estimated output.

3

The Simulation Model and Methods for Analysis

In this chapter the methods are presented. The chapter is split into modeling and simulation, control, and validation.

3.1 Modeling

The simulation model was built in Simulink [40], with scripts for automation and data analysis written in MATLAB [41]. The model takes frequency as an input and outputs active power.

3.1.1 Turbine Characteristics and Waterways

The turbine characteristics of a hydro turbine are generally determined using index tests, measuring active power, water flow and efficiency for different combinations of guide vane position and runner blade angle. The data that can be extracted is limited, since large deviations from normal operating points may lead to damages in the turbine. Further, the data is usually confidential and may not be accessible prior to testing.

The approximated turbine characteristic used in [10] was provided by Michael Gratza [42]. It defines the steady state power output for the entire range of guide vane positions and runner blade angles, as a 101×101 matrix. In practice it was implemented as a 2-D lookup table in Simulink. It does not define any dynamics in itself, those must be modeled by other components. The characteristic has a constant term $\bar{P}_0$ and a term $\bar{M}$ multiplied with head, as seen in (3.1) (in physical units) and (3.2) (in per-unit). Any resulting negative values in $P_{\text{ss}}(\bar{Y}, \bar{\alpha})$ were changed to zero.

$$P_{\text{ss}}(\bar{Y}, \bar{\alpha}) = \bar{M}(\bar{Y}, \bar{\alpha}) \cdot \frac{P_{\text{nom}} \cdot h}{h_{\text{nom}}} + \bar{P}_0(\bar{Y}, \bar{\alpha}) \cdot P_{\text{nom}}. \tag{3.1}$$

$$\bar{P}_{\text{ss}}(\bar{Y}, \bar{\alpha}) = \bar{M}(\bar{Y}, \bar{\alpha}) \cdot \frac{h}{h_{\text{nom}}} + \bar{P}_0(\bar{Y}, \bar{\alpha}). \tag{3.2}$$

The approximated turbine characteristic was used because it is generalized to be used for different turbines, and only needs three parameters: nominal power and

hydraulic head, and actual hydraulic head during operation. This was deemed to be in line with the goal of defining a model that is easily parametrized.

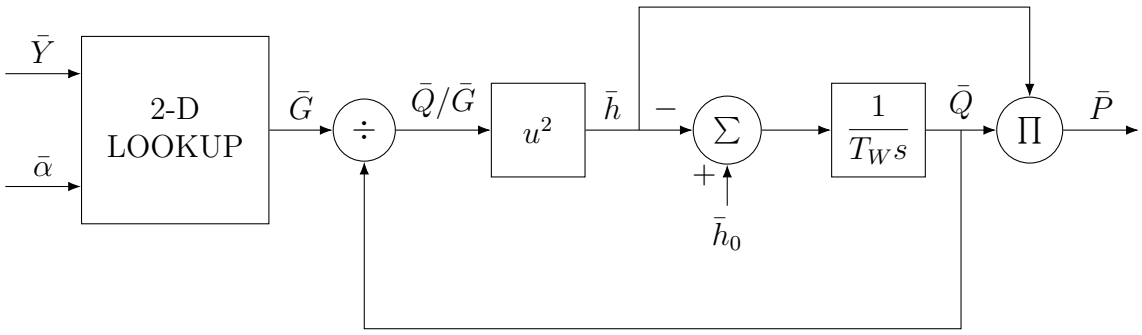

Figure 3.1: Block diagram of turbine and waterways model.

The waterways model used in this work is similar to previously used ones, such as in [22] and [9]. The nonlinear waterways model in [22] uses an affine transformation of the guide vane position, called 'ideal gate opening', as input, to account for losses. The same model was used in [9], but with the equivalent guide vane position combined with runner blade angle as the input. The equivalent guide vane position was calculated from the actual position using steady state measurements. Here, the input to the same waterways model is the output of the turbine characteristic from [10] as described above. It is denoted as $\bar{G}$, in accordance with [22]. The initial head $\bar{h}_0$ was fixed to 1, as all steady state behavior of the turbine was assumed to be encoded in the turbine characteristic. For the same reason, the output was not multiplied with some efficiency η. The model seen in Figure 3.1 is a visual representation of Equations 2.18, 2.19, and 2.20.

Linearized models of the waterways exist, for example the model seen in Equation 3.3 was used in [5]. The waterways dynamics change with load level [22]. The model seen in (3.3) is linearized about the operating point with guide vane position $\bar{Y}_0$ and is therefore most accurate near that point. Since some simulations contain large changes in output power, the linearized model would no longer be valid during some parts of the simulations. The nonlinear model seen in Figure 3.1 takes into account the altered behavior at different load levels by design. This is illustrated in Figure 3.2. During the first upwards control action in Figure 3.2a, the models initially respond in the same manner, since the process is near the linearization point $\bar{Y}_0$. As the guide vane position moves further from the initial value, the outputs become are no longer the same. Later in the simulation in Figure 3.2b, both systems have reached steady state at 0.8 pu when downward control action is initiated. The nonlinear model exhibits a larger swing in the upward direction due to the higher load level, but the linearized model reacts exactly like at 0.5 pu, only mirrored. As the outputs move closer to the initial value, the model outputs become more similar. In both directions, the nonlinear model exhibits a slower response, making it a more conservative choice.

$$G_{\text{ww,lin}}(s) = \frac{-\bar{Y}_0 T_W s + 1}{0.5\bar{Y}_0 T_W s + 1} \tag{3.3}$$

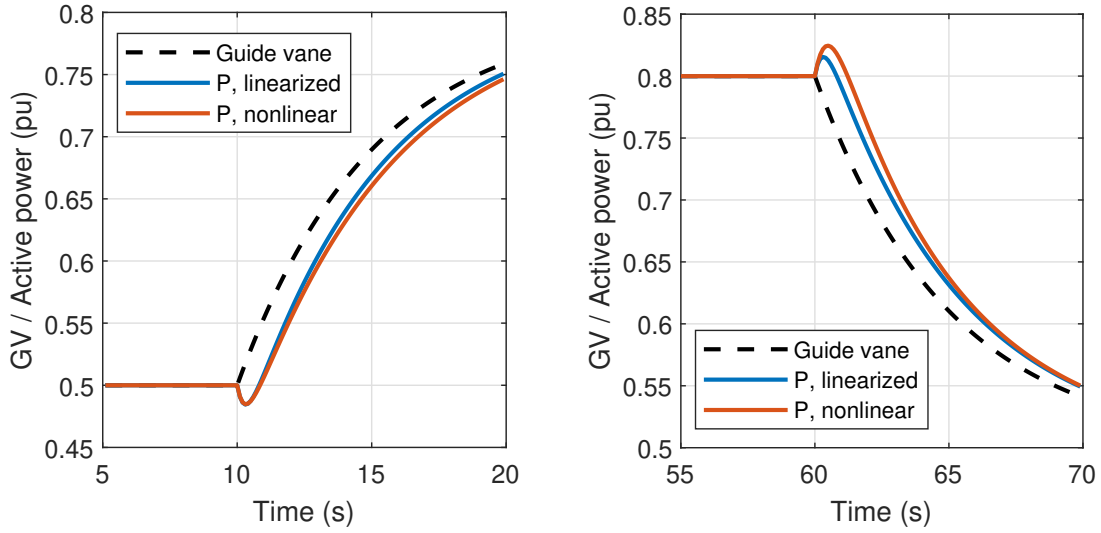

(a) Upward change from initial GV position 0.5 pu to 0.8 pu.

(b) Downward change from 0.8 pu back to the original GV position 0.5 pu.

Figure 3.2: Comparison between linearized (Eq. 3.3) and nonlinear (Figure 3.1) waterways model. The guide vane position is represented by an upward and downward step with magnitude 0.3 pu filtered through a first order low-pass filter with an arbitrarily chosen time constant 5 s. Both models have a water time constant (at full load) $T_W = 1.2$ s. The linearized model is linearized around the initial guide vane position $\bar{Y}_0 = 0.5$ pu. The plots show the same simulation at different times.

3.1.2 Servos

Servos in hydro power plants are often approximated as first order lag elements [2]. However, in [10], a second order model was used. The basic model used in this thesis is a first order model with a dead band (DB), rate limiter (RL) and mechanical backlash (BL), as seen in Figure 3.3. An input delay was also modeled. The validity of using a first order model was tested using the MATLAB System Identification Toolbox [43].

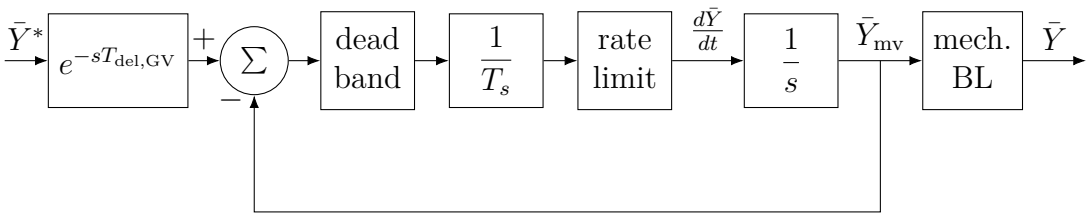

Figure 3.3: Block diagram of the servo model. In the figure the guide vane servo is shown, but the same model is used for the runner blade servo.

The model approximates the aggregated system of actuators and controllers. In order to fully model the mechanical system and its control, detailed information would be needed. Since only the relationship between input and output is essential for stability studies, the inner details can usually be omitted. Tuning the servo controllers can be modeled by changing the time constant T_s.

3.1.3 Estimation of Parameters

Since one aim of the project was to create a general model that suitable for simulating Kaplan turbines before conducting physical prequalification tests, simpler models with fewer parameters were preferred.

Table 3.1: Model parameters and how they are obtained.

Parameter	Description	Source
P_{nom}	Nominal plant power	Provided by plant owner
h_{nom}	Nominal hydraulic head	Provided by plant owner
h_{act}	Hydraulic head during test	Estimated from measurements
T_W	Water time constant	Provided by plant owner
$T_{s,\text{GV}}$	Servo time constant, guide vane	Estimated from measurements
$T_{s,\text{runner}}$	Servo time constant, runner	Estimated from measurements
$T_{\text{del,GV}}$	Input delay, guide vane	Estimated from measurements
$T_{\text{del,runner}}$	Input delay, runner	Estimated from measurements
BL_{GV}	Mechanical backlash, guide vane	Estimated from measurements
BL_{runner}	Mechanical backlash, runner	Estimated from measurements
$RL_{\text{GV,open}}$	Rate limit, guide vane, opening	Estimated from measurements
$RL_{\text{runner,open}}$	Rate limit, runner, opening	Estimated from measurements
$RL_{\text{GV,close}}$	Rate limit, guide vane, closing	Estimated from measurements
RL_{runner}	Rate limit, runner, closing	Estimated from measurements
DB_{GV}	Servo dead band, guide vane	Estimated from measurements
DB_{runner}	Servo dead band, runner	Estimated from measurements

3.1.3.1 Servo Parameters

A measurement series from normal operation, i.e. using actual grid frequency as input to the controllers, was used for estimating the servo time constants, considering it would contain relevant frequency components. The System Identification Toolbox [43] was used to estimate transfer functions. The system identification app, among other things, identifies parameters of transfer functions with a predetermined number of poles and zeros. The parameters are tuned to find the best fit for the selected input and output, defined as either measurement series or frequency response data in a MATLAB format. For the guide vane servo model seen in Figure 3.3, the controller output $\bar{Y}^*$ was used as the input and measured guide vane position $\bar{Y}_{\text{mv}}$ as output. For the runner servo, the measured guide vane position $\bar{Y}_{\text{mv}}$ was used as the input and measured runner position $\bar{\alpha}_{\text{mv}}$ as output, since the reference value for the runner servo is calculated from the measured position of the guide vanes in

the real unit. The system identification showed that higher order systems did not provide much improvement over simple first order systems. However, the estimated time constants for the guide vane and runner servos could not be used, since the system identification could not consider backlash and dead bands.

The total backlash, i.e. the sum of the dead band and the mechanical backlash as seen in Figure 3.3, in the guide vane servo was determined by examining the difference between $P_{ss,0}$ and $P_{ss,3}$ in the FCR-N step test measurements (see Appendix A). The difference in power was used to calculate an equivalent difference in guide vane position, using the turbine characteristic. The share of the backlash located in the servo dead band was found through trial and error, until the time domain behavior during sine tests closely matched that of the measurements. The mechanical backlash of the runner servo was assumed to be the same as for the guide vane servo, and the servo dead band was similarly adjusted until the qualitative behavior was deemed correct. The servo time constants were changed from the ones found through system identification, again to achieve the desired qualitative behavior.

The ramp rate limits of the guide vanes and runner blades were found by inspecting the movement during the fastest ramps. The rate limit was chosen as the highest speed during linearly changing position/angle, since that implies the speed is saturated.

The input delay of the guide vanes was similarly found by measuring the time between large steps in frequency to the first motion of the guide vanes. For the runner blades, the time between first motion of the guide vanes and the first motion of the runner blades was used.

The servo parameters were validated using the frequency domain data from sine tests.

3.2 Control

In this section, the control of the unit is described, along with changes made in order to improve the response.

3.2.1 FCR Controllers

The simulation model used PI controllers with droop, like the actual unit. Every product, along with LFSM-O and LFSM-U, had a separate controller, and the sum of the controllers' outputs and the original setpoint was fed to the servos, as seen in Figure 3.4.

Each parallel controller block contained one PI controller with droop, like shown in Figure 2.3. In accordance with the real unit, the FCR-D downwards and FCR-D upwards controllers shared the same parameters. In addition, the FCR-N controller and both LFSM controllers shared the same parameters as the FCR-D controllers in stability mode.

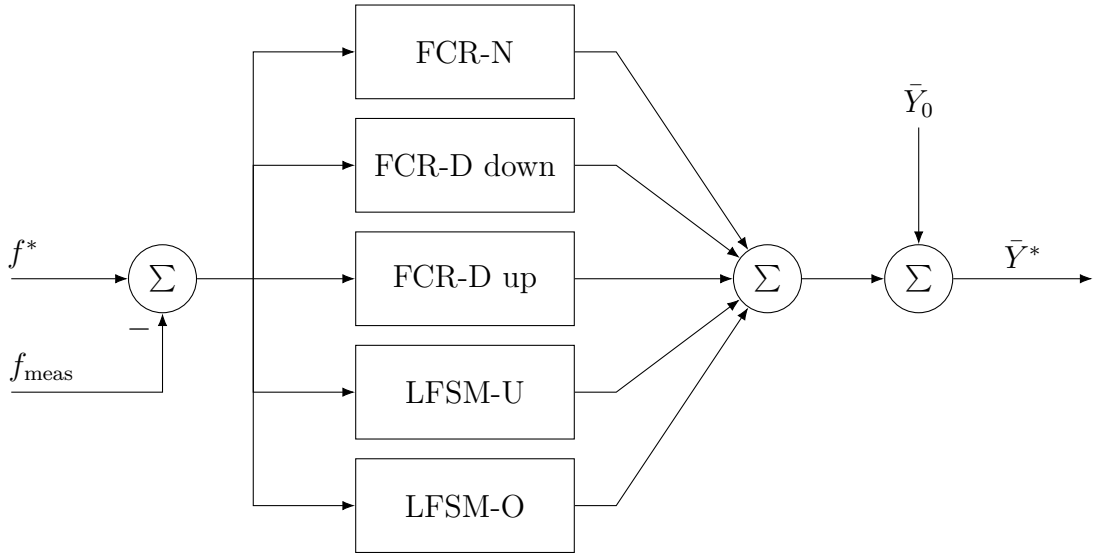

Figure 3.4: Controller structure in the model.

3.2.2 Mode shifting

In accordance with the technical requirements [1], the FCR-D controllers had a stability mode and a performance mode. The performance mode was activated for disturbances larger than 0.2 Hz, could only be active for 10 s and was then blocked from activating during a 5 minute period.

The technical requirements state that switching between the modes must happen without 'bumps' in the response. This was interpreted to mean that only the integral gain could be altered, by changing T_{feedback}, since changing the proportional gain would immediately affect the controller output.

3.2.3 Combination Unit

The combination unit, as seen in Figure 3.5, calculated a setpoint for the runner blade angle from the measured position of the guide vanes, mimicking the real unit. The combination unit was implemented as a 1-D lookup block in Simulink, interpolating a predefined combination curve.

Data of the actual combination used was not readily available. Since the most efficient combination in the real plant and the approximated turbine characteristic were not necessarily the same, the combination curve was approximated by choosing the runner blade angle with highest power output for every guide vane position in the approximated turbine characteristic. Thus the most important characteristics near the most efficient combination could be captured. This curve was smoothed in order to be more realistic and avoid jittery movement in the runner blades. The smooth curve was achieved using a fifth-order polynomial fit.

The combination curve was calculated based on the turbine characteristic ahead of

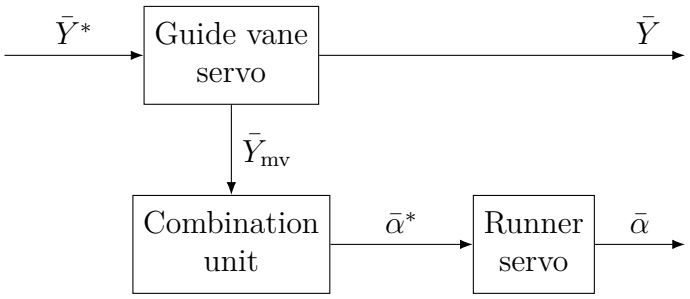

Figure 3.5: Block diagram of guide vane and runner combination. The setpoint of the runner servo depends on the measured value of the guide vane servo.

each set of simulations.

3.2.4 Active Power Feedback

The methods for active power feedback described in [32] could not be implemented directly in the model. This was because unlike in [32], several controllers are active, and ΔP is not a directly measurable variable that can be separated for each controller. Instead, the active power feedback was achieved by adding a controller acting on the error between the change in active power $\Delta\bar{P}$ and the controller output $\Delta\bar{Y}^*$. In order to avoid affecting the dynamic performance in the short term, the added controller was realized as an integral-only controller, with a large integration time constant T_P.

The controller structure with active power feedback can be seen in Figure 3.6. The output of the active power controller would continue to grow (or decrease) until the measured per-unit change in power equaled the FCR controller output. When using this structure, the theoretical capacity $\Delta P_{\text{theoretical}}$ would be calculated as

$$\Delta\bar{P}_{\text{theoretical}} = \frac{\Delta\bar{f}_{\max}}{E_p} = \frac{\Delta f_{\max}}{f_n \cdot E_p}, \tag{3.4}$$

with $\Delta f_{\max} = 0.1\,\text{Hz}$ for FCR-N and $\Delta f_{\max} = 0.4\,\text{Hz}$ for FCR-D.

Another method, where the FCR controller output was treated as desired active power change and fed to a lookup table in order to get $\bar{Y}^*$ was also tested. This would correspond to the gain scheduling described in [31].

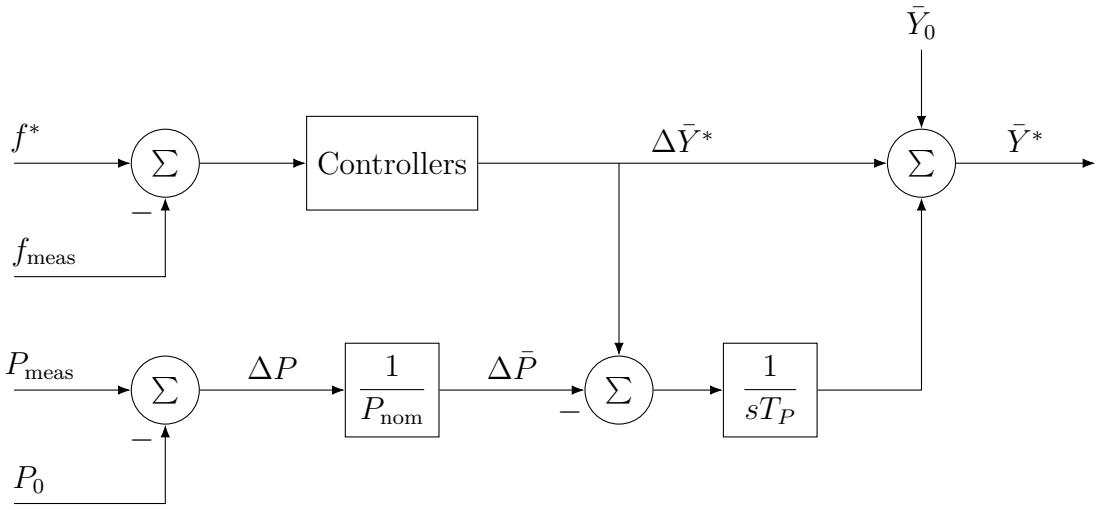

Figure 3.6: Controller structure using active power feedback. The parallel controllers for the different frequency reserves, seen in Figure 3.4, are aggregated in one block.

3.3 Simulation

The model was simulated using the frequency inputs defined in [1], as well as a recording of grid frequency taken during tests. The simulations mimicked tests performed on a real unit, with the same operating points, droops, and controller parameters (during validation). The simulations were performed with the odeN solver of order 4, with a maximum time step of 0.01 s, the same as the sample time in the measurements. The specifications of the different simulations can be seen in Appendix B.

Due to the structure using lookup tables, the turbine characteristic and thus combination curve could not be changed dynamically during the simulations. Therefore, the turbine characteristic was only calculated once per set of simulations. As a consequence of this, the gross hydraulic head, i.e. the height difference between the headrace and talirace water surfaces, h in Equation 3.1, was constant.

3.4 Validation

The responses of the servos for the guide vanes and runner blades were validated separately, so that the focus of validating the entire model could be on the behavior of the turbine and waterways themselves.

The validation of the whole model was split into three parts:

1. Steady state activation, i.e. the ΔP_{ss} values checked against the many instances of Requirement 1.
2. Dynamic activation during ramps. This corresponds to Requirements 2, 3,

and 4.

3. Frequency response from the sine tests. The amplitude and phase of the fitted sine of active power, when the frequency input was changed sinusoidally. These were used to check compliance with Requirements 8 and 9.

Validation was done using the key measurements during prequalification, seen in Table 3.2. The measurements are described in Section 2.4.3 and Appendix A. During validation, none of the proposed control improvements from section 3.2 were used. In this case, sine tests were only performed for FCR-N and downward FCR-D, since both FCR-D controllers shared the same parameters.

Table 3.2: Measurements used for prequalification and validation.

Measurement	Taken during	Products	Req.
ΔP_{ss}	Steady state activation tests	All	1
$\Delta P_{7.5\text{s}}$	Fast ramp tests	FCR-D, both	2
$E_{7.5\text{s}}$	Fast ramp tests	FCR-D, both	3
$E_{\text{overshoot}}$	Deactivation test	FCR-D, both	4
$P(j\omega)$	Sine tests	FCR-N, FCR-D down	8, 9, 10

The simulated and tested values were compared in order to find the prediction errors, here defined as $\hat{y} - y$ for a measurement y. The prediction errors and their distributions were studied.

The theoretical FCR capacity for the different tests was calculated using the approximated turbine characteristic. Using this, the measurements from Table 3.2, both simulated and measured on the real unit, could be evaluated against the technical requirements. The results were compared in order to quantify the model's ability to predict passed and failed tests.

3.4.1 Sensitivity Analysis

A sensitivity analysis of the model was performed as described in Section 2.6. The inputs to the model were the parameters described in Table 3.1, and the outputs were the measurements in Table 3.2, except for the frequency domain measurements. Instead, the stability margin and performance margin (see Appendix A) were used as outputs, since they contain the most important information from the frequency response.

The parameters and their domains are seen in Table 3.3. The parameters P_{nom}, h_{nom}, and h_{act} were fixed, since they are only used for computing the approximated turbine characteristic, which is affected in an obvious manner. The reason for the choice of domain is specified in the table. In the case of servo time constants, the minimum value was chosen to be slightly better than the baseline value in [14], [15], [17], while the maximum value was based on the parameter estimation performed in this project.

The sensitivity analysis was in practice done using parameter sweeps, where all

parameters in Table 3.3 were sampled randomly from uniform distributions. This was done in order to find possible interactions between different parameters without exhaustively sweeping all possible combinations. Some individual parameter sweeps were performed to more clearly investigate the effects of single parameters.

Table 3.3: Domain of model parameters for the sensitivity analysis.

Parameter	Min	Max	Unit	Justification
T_W	0.01	2.00	s	Almost all plants fall in this range [16]
$T_{s,\mathrm{GV}}$	0.1	1.00	s	Previous work, results in this project
$T_{s,\mathrm{runner}}$	0.1	1.00	s	Same range as for guide vane
$T_{\mathrm{del,GV}}$	0	1.00	s	Unfeasible for larger values
$T_{\mathrm{del,runner}}$	0	1.00	s	Same range as for guide vane
BL_{GV}	0	0.012	pu	Same range as [14]
BL_{runner}	0	0.012	pu	Same range as for guide vane
$RL_{\mathrm{GV,open}}$	0.02	0.18	pu/s	Around the value used in [15]
$RL_{\mathrm{runner,open}}$	0.02	0.18	pu/s	
$RL_{\mathrm{GV,close}}$	0.02	0.18	pu/s	
$RL_{\mathrm{runner,close}}$	0.02	0.18	pu/s	
DB_{GV}	0	0.012	pu	Same range as for backlash
DB_{runner}	0	0.012	pu	

4

Results and Analysis

Here, results from calculations and simulations are presented and analyzed.

4.1 Turbine Characteristics in Steady State

The approximated turbine characteristic described in section 3.1.1 was compared with measurements of steady-state power, water flow, and guide vane position from the actual plant, received from the plant owner. These measurements did not contain runner blade angle data, so the runner blades were assumed to follow the combination curve used in normal operation. In Figure 4.1, the approximated turbine characteristic can be seen along with maximum power combinations. The smoothed maximum power combination is similar to efficiency combinations used in other plants, so it was deemed an acceptable approximation of the actual most efficient combination.

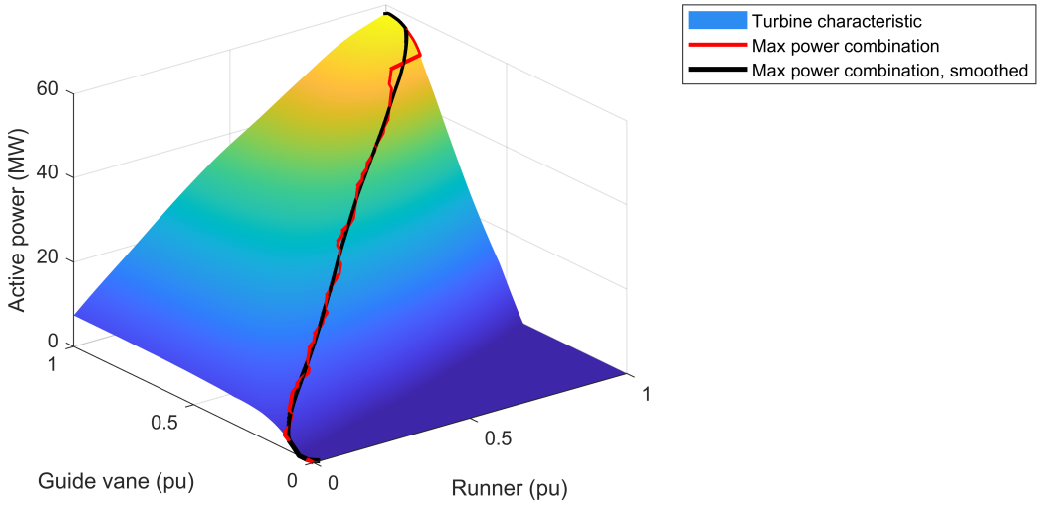

Figure 4.1: Approximated Kaplan turbine characteristic for a head of 36 m. Nominal head 33 m, nominal power 48 MW.

The combination relationship used for a 36 m head is seen in Figure 4.2a. The resulting steady-state power characteristic is seen in Figure 4.2b. It is clear that the smoothed combination curve results in practically no difference from the 'raw'

curve. Further, the power characteristic calculated from the model is close to the curve produced from measurements.

The polynomial fit of the combination curve for 36 m head resulted in (4.1). Values outside the endpoints 0 and 1 were changed to the respective endpoints, as seen in Figure 4.2a. The combination curves depended on hydraulic head but were similar to each other, as seen in Figure 4.6. The approximation works well within the operating range of the unit, i.e. guide vane positions between 0.45 pu and 0.85 pu.

$$\bar{\alpha}^* = -11.61 \cdot \bar{Y}^5 + 29.37 \cdot \bar{Y}^4 - 27.61 \cdot \bar{Y}^3 + 12.06 \cdot \bar{Y}^2 - 1.258 \cdot \bar{Y} + 0.02381 \quad (4.1)$$

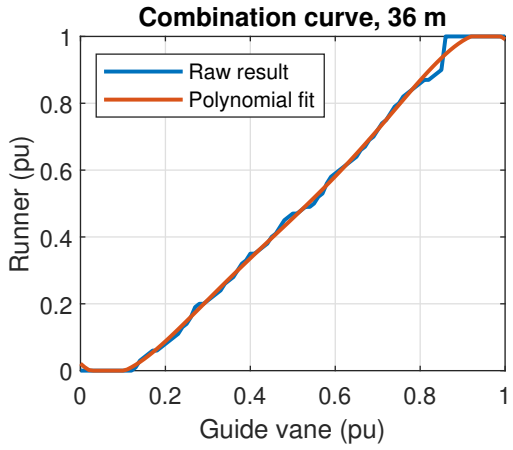

(a) Combination curve. The raw result of using the runner blade value resulting in the highest power for each of the 101 guide vane values is compared with a fifth order polynomial fitted to it.

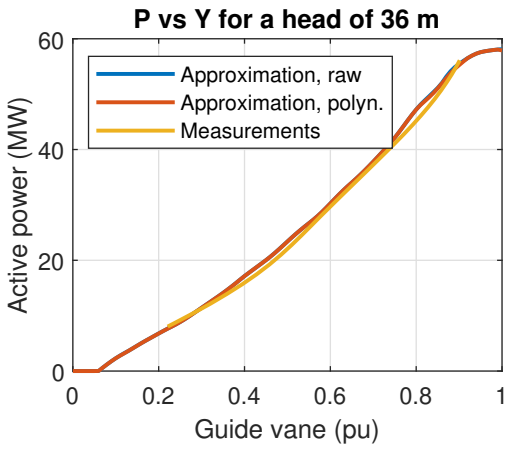

(b) Power characteristic. The results of applying the combination curves in **(a)** to the turbine characteristic are compared to steady-state measurements of power for a range of guide vane positions.

Figure 4.2: Comparison of the combination curves with and without polynomial smoothing, and their respective power characteristics calculated from the approximated turbine characteristic, compared with measurements from the studied Kaplan turbine. Calculated for a head of 36 m. Nominal head 33 m, Nominal power 48 MW

The error was obtained by subtracting the measurements from the approximation. It can be seen in Figure 4.3 over the range of measured guide vane values and for different heads between 30 m and 36 m. The hydraulic head varies based on the river conditions, but nominal head and nominal power are constants. Other model parameters do not affect the turbine characteristic. The error can be seen to vary with the head, with larger errors for larger heads. The peaks at 0.45 pu and 0.8 pu correspond to the overestimation of power output in figure 4.2b.

Based on the observations of the errors in Figure 4.3, the relationship between error and head was examined. The range of 0.45 pu – 0.85 pu was of particular interest, since the power plant operates within that range of guide vane settings. Thus the mean error in the aforementioned range was calculated. From Figure 4.4 it is clear that the mean error depends linearly on the head within the operating range. A line was fitted to the data for error compensation. The error represents that $\bar{M}$ in (3.1),

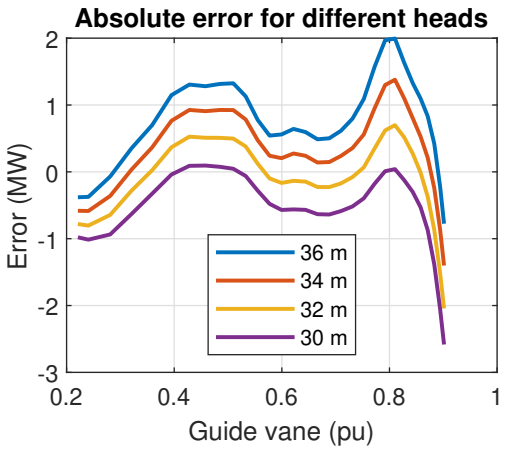

(a) Error of the approximation in MW.

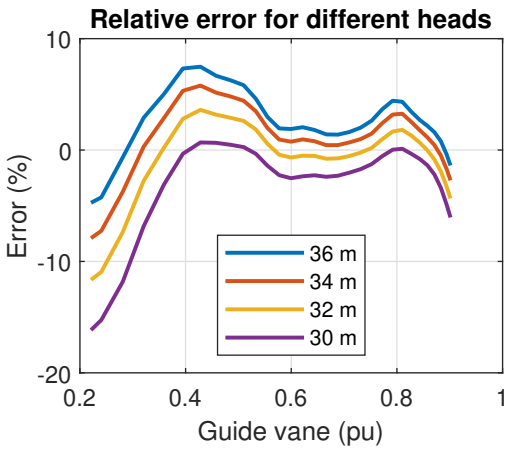

(b) Error of the approximation, relative to the measurements.

Figure 4.3: Approximation error for different heads, using the smoothed combination curves. The nominal head of the turbine is 33 m and the nominal power is 48 MW.

i.e. the turbine characteristic's linear dependence on head is not perfectly modeled for this particular unit.

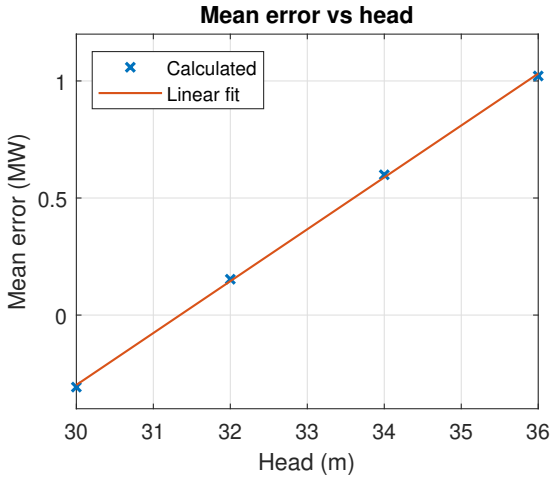

Figure 4.4: Linear relationship between mean error and head. The mean error is calculated by integrating the errors in the range 0.45 pu - 0.85 pu for each measurement series with constant head. The nominal head of the turbine is 33 m and the nominal power is 48 MW.

Using the coefficients for the linear fit, the mean error for the operating range could be calculated for heads between 30 m and 36 m. Based on the very limited availability of data and the assumption that deviations from the efficiency combination curve would be small, the mean error for a given head was subtracted from the entire turbine characteristic, equivalent to shifting the z-axis in Figure 4.1.

The errors after compensation can be observed in Figure 4.5. After compensation,

the error in the operating range is centered around 0. In almost the entire operating range, the relative error is kept within ±2%. The curves are much closer together than in Figure 4.3, which can be interpreted as the dependence on head being largely eliminated.

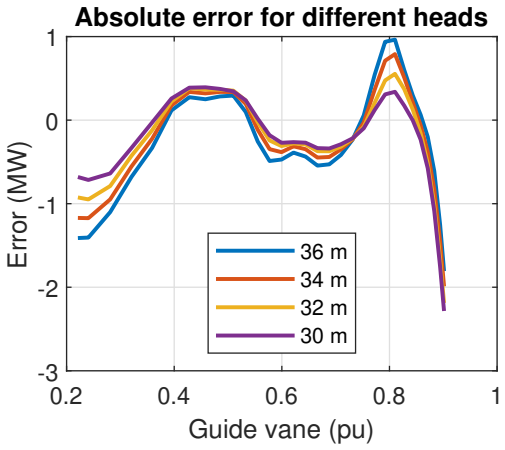

(a) Error of the approximation in MW.

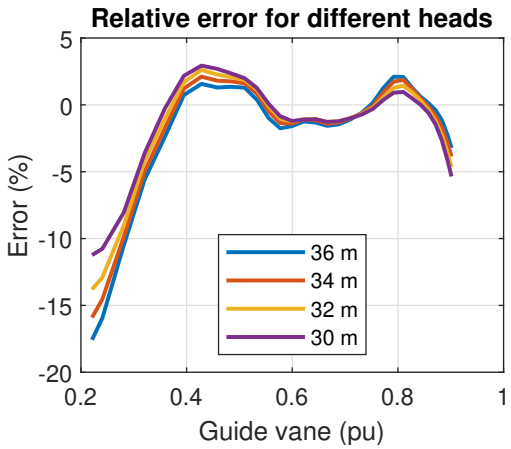

(b) Error of the approximation, relative to the measurements.

Figure 4.5: Approximation error for different heads, using the smoothed combination curves. Both the turbine characteristics an the combination curves have been compensated with mean error. Now the approximation errors in the range 0.45 pu - 0.85 pu are centered around 0. The nominal head of the turbine is 33 m and the nominal power is 48 MW.

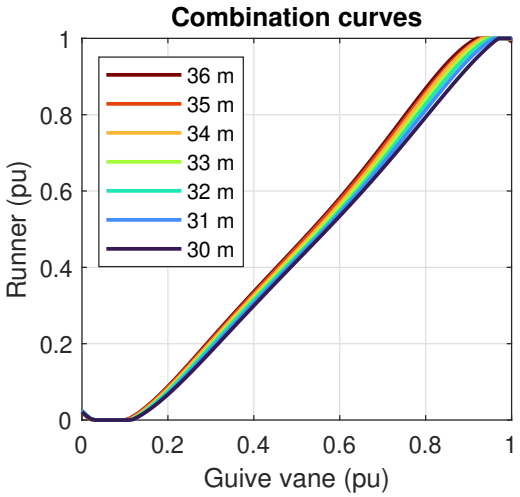

Figure 4.6: Combination curves for different values of head. The curves have been smoothed using a fifth order polynomial. These curves were produced from turbine characteristics compensated with mean error. Nominal head was 33 m. The curves are independent from nominal power.

Based on the steady-state results presented here, the approximated turbine characteristic was deemed promising for dynamic simulations. The calculation of combination curves used here was also applied for the subsequent simulations.

4.2 Verification and Validation of Simulation Model

In this section, the validation results are presented. The results are split into verification of expected behavior, validation of servo parameters, steady-state activation, dynamic activation and frequency domain response. During the validation of the prequalification tests, the guide vane and runner servos are assumed to be correctly simulated.

4.2.1 Verification of Expected Behavior

The model was verified to behave as expected. In Figure 4.7 the results from the FCR-D upwards ramp sequence with low load and high droop are seen. The controller gives a positive output for a negative frequency deviation. For frequencies above 49.9 Hz, only FCR-N is activated, and it is saturated for larger deviations. Between 49.9 Hz and 49.5 Hz, FCR-D upwards is activated and then saturated. When the frequency decreases below 49.5 Hz, LFSM-U is activated. FCR-D downwards and LFSM-O are not activated during this test since only negative frequency deviations are tested. Mode shifting is activated at the correct events, i.e. the deactivation test around 100 s and fast ramp test near 750 s, and blocked during other ramps. At around 400 s, the performance mode is activated since the frequency deviation is still more than 0.2 Hz, and the cooldown of 300 s has been finished. The guide vane position follows the controller output, and the runner blade angle follows the guide vanes according to the combination curve in Figure 4.2a. For example, between 250 s and 400 s the guide vane position is 0.6 pu and the runner blade angle is 0.55 pu, while both servo positions are near 0.7 pu around 800 s. This corresponds well with the combination curve for 33 m head in Figure 4.6. The behavior was verified for all tests.

4.2.2 Servo Parameter Estimation and Validation

Using the frequency domain data, the servo parameters were validated. In Figure 4.8, the Bode diagram showing the response from frequency error ($e = f^* - f_{\text{meas}}$) to measured guide vane position ($\Delta\bar{Y}_{\text{mv}}$) is seen. The deviations from the measurement phase were deemed acceptable, as there was no obvious bias in either direction.

In Figure 4.9, the equivalent data for the runner blade angle can be seen. In the Bode diagram constructed from FCR-N tests, the modeled runner seems to be have a lower phase delay compared to the measurements, meaning a faster response. However, the opposite is true for the FCR-D sine tests, so tuning the parameters further would improve accuracy in one test while worsening it in the other.

The estimated parameters can be seen in Table 4.1. The measurements that the estimations are based on can be seen in Appendix D.1.

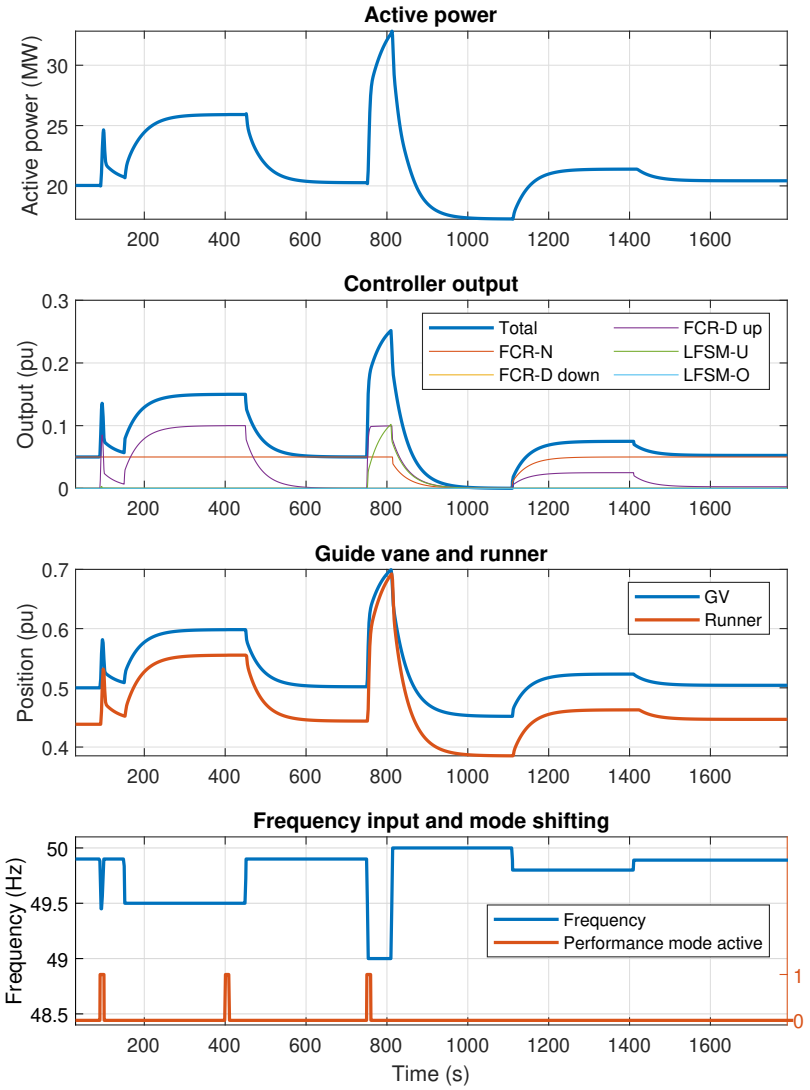

Figure 4.7: Simulated FCR-D upwards ramp sequence for low load (initial GV 0.5 pu) and high droop (8%). The nominal head of the turbine is 33 m and the nominal power is 48 MW. The actual head used in the simulation is 33.4 m, like the corresponding real-world test.

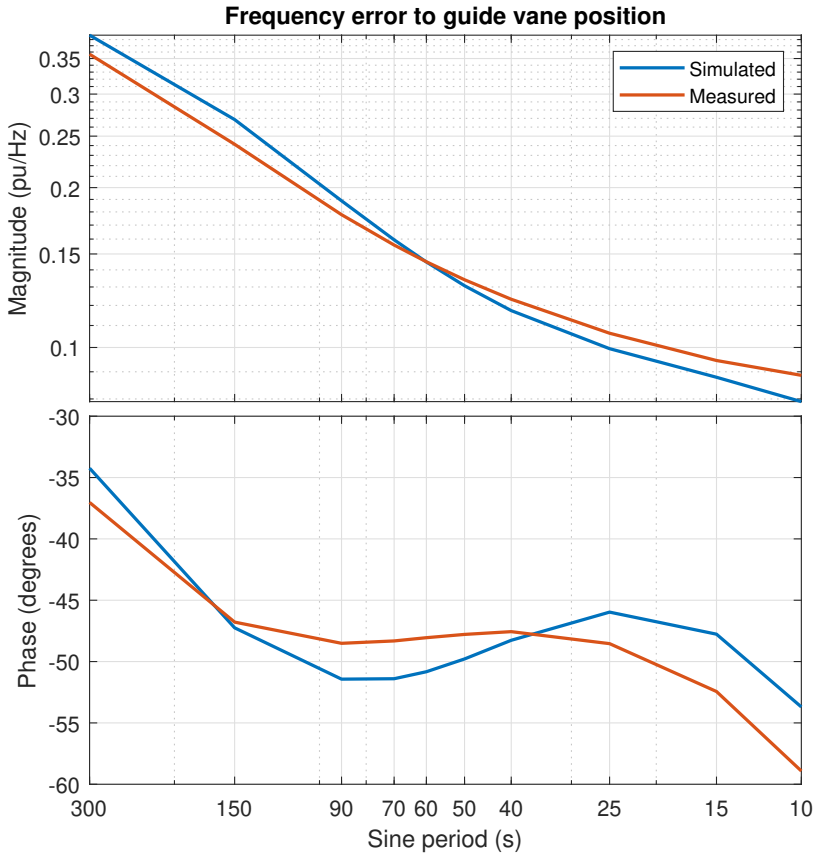

Figure 4.8: Bode diagram of the approximated transfer function from frequency error to guide vane position during FCR-N sine tests $\left(\frac{\Delta \bar{Y}_{\text{mv}}(j\omega)}{e(j\omega)}\right)$.

Table 4.1: Estimated servo parameters of the studied unit.

Parameter	Unit	Guide vane	Runner
T_s	s	0.8	0.8
T_{del}	s	0.2	1.0
BL	pu	0.0035	0.0035
RL_{open}	pu	0.05	0.03
RL_{close}	pu	0.05	0.03
DB	pu	0.0035	0.0065

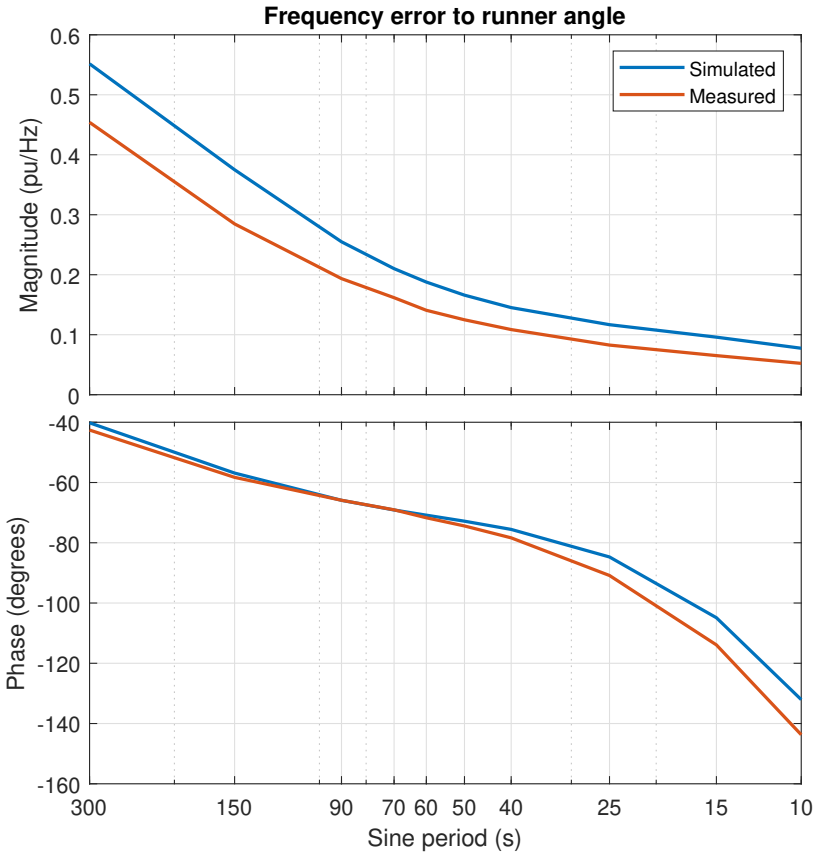

Figure 4.9: Bode diagram of the approximated transfer function from frequency error to runner blade angle during FCR-N sine tests $\left(\frac{\bar{\alpha}_{\mathrm{mv}}(j\omega)}{e(j\omega)}\right)$.

4.2.3 Steady State Performance

In this section, the steady-state activations for FCR-N are presented. The steady-state results for FCR-D, both directions, behaved in the same way. For brevity, only FCR-N is discussed here, but the results for FCR-D are available in Appendix C.

The steady-state activation differed for the different test conditions. It is important to note that what is examined is ΔP_{ss}, which means a constant offset in the simulations does not affect compliance with the requirements. Therefore, the plots are adjusted to only show the change in active power. However, as previously seen in Figure 4.5a, the steady-state error is not constant in the operating range. For example, the upward activation seen in Figure 4.10 was predicted to be 10.176 MW, 12% higher than the measured value 9.068 MW.

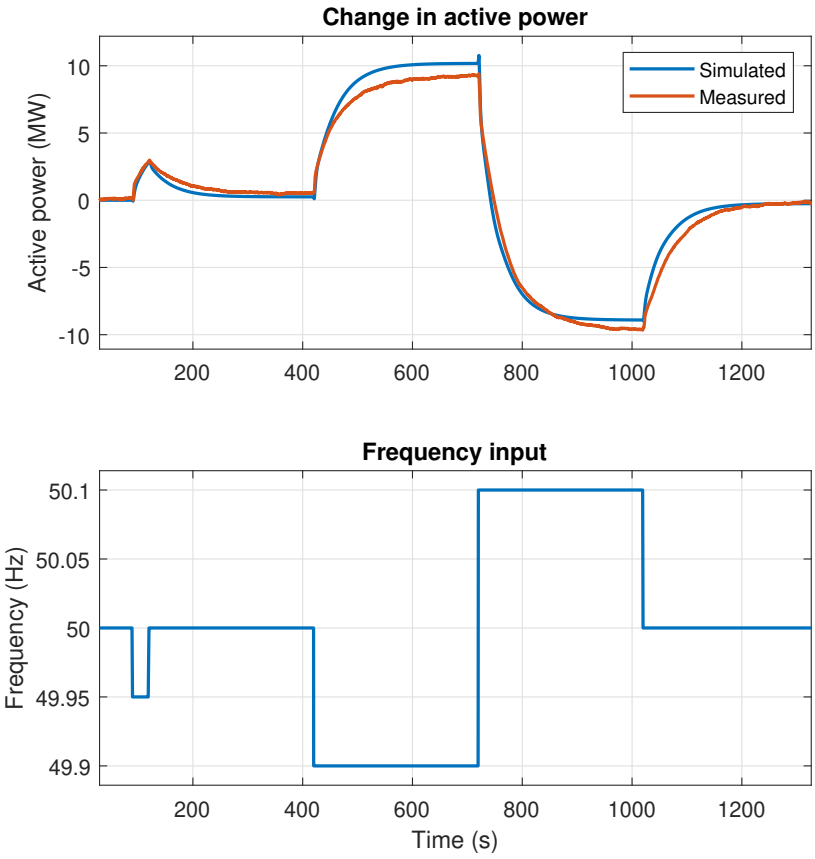

Figure 4.10: FCR-N step test for low load (initial GV 0.6 pu, ca 27 MW) and low droop (1.33%). The nominal head of the turbine is 33 m and the nominal power is 48 MW. The actual head is 33.4 m. This test is also represented in the first row of Table 4.2.

Although the steady-state errors seemed small in the previous section (at most 2.5% relative error in the operating range 0.45 pu – 0.85 pu), the relative effect becomes large when tests are performed in a small part of the operating range. In Table 4.2, the steady-state activation for FCR-N is examined. The column 'Test version'

refers to the test conditions specified in Table 2.1, with e.g. LH being short for Low load, High droop, as well as direction. The same theoretical activation, calculated from the model, is used for both simulation and measurement when evaluating the requirement. For most of the downward activations and one upward activation, both simulations and measurements show clear under-delivery, but in the other cases the model does not correctly predict whether the requirement is fulfilled.

Table 4.2: FCR-N steady-state activation. Absolute values are used. The test version refers to the combination of load and droop, e.g. LH is low load and high droop, as well as the direction of activation. In order to pass Requirement 1, the activation must be between 95% and 120% of the theoretical value. The error, indicated in square brackets, is relative to the measurement.

	Steady state activation (MW)			Requirement 1	
Test version	Theoretical	Measured	Simulated	Meas.	Sim.
LL, up	10.465	9.068	10.176 [+12.2%]	Fail	Pass
LH, up	3.011	3.168	2.819 [-11.0%]	Pass	Fail
HL, up	11.170	10.667	11.460 [+7.4%]	Fail	Pass
HH, up	3.343	2.844	3.092 [+8.7%]	Fail	Fail
LL, down	10.465	9.797	8.905 [-9.1%]	Fail	Fail
LH, down	3.011	2.623	2.777 [+5.9%]	Fail	Fail
HL, down	11.170	10.154	9.662 [-4.8%]	Fail	Fail
HH, down	3.343	3.344	3.134 [-6.3%]	Pass	Fail

The errors seen in Table 4.2 can partly be attributed to what was seen in Figure 4.5. For example, the downward activation in the test with low load and low droop was predicted to be around 1 MW smaller than the measured value. With the initial guide vane position of 0.6 pu, the active power should be underestimated by around 0.3 MW according to figure 4.5. For full downward activation, 0.45 pu, the active power should be overestimated by the same amount, so the downward activation would be expected to be underestimated by 0.6 MW in total. Similarly, at 0.75 pu, full upward activation, the estimation error should be close to zero, resulting in a 0.3 MW overestimation of the activation. The actual errors were significantly larger in both directions. Thus the errors in Figure 4.5 can not explain all discrepancies between the simulations and real tests. Figure 4.5 is based on the measurements provided by the plant owner, which may not be entirely accurate for all conditions.

In general, the model predicted the fulfillment of Requirement 1 poorly. Besides the values shown in Table 4.2, another 12 steady-state activations are evaluated in the entire testing program. Aggregated results are shown in Figure 4.11, in the form of a confusion matrix. It can be seen that the model predicted both failing and passing measurements incorrectly in more than half of the cases. In summary, the model was worse than random chance at predicting fulfillment of Requirement 1. However, the simulated steady-state responses had a mean signed error of only -0.73%, relative to the measurements. Small errors are amplified in these tests when the guide vanes move from a region of overestimation to underestimation and vice versa, and any

errors in the 'ground truth' used for compensating the characteristic propagate to these errors.

The steady-state errors are difficult to rectify, partly because the model is simplified. The turbine characteristic is a general model meant to be able to represent many different Kaplan turbines, so differences between turbines will lead to some errors. The steady-state data used to error compensate the turbine characteristic is not guaranteed to be accurate for all conditions. Also, local water conditions may vary during tests, and interactions with e.g. nearby turbines are not modeled. More detailed modeling of all related phenomena would extend the scope of this thesis and conflict with the stated objective of building a model implementable before real-world tests.

The failure to meet Requirement 1 can be rectified using active power feedback, which will be seen in section 4.4.3.

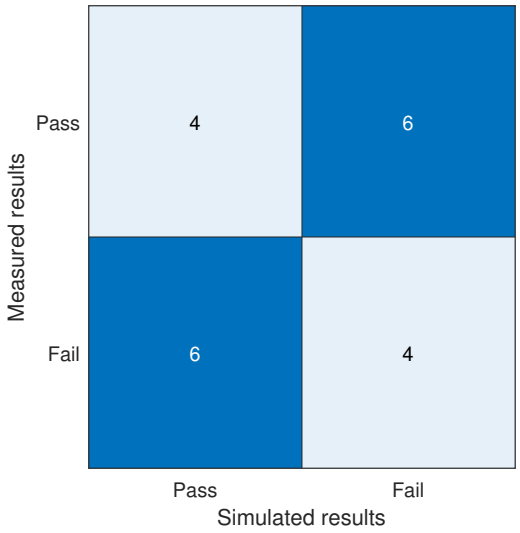

Figure 4.11: Confusion matrix for Requirement 1, all products and directions.

4.2.4 Dynamic Time Domain Performance

The values calculated during the deactivation test and fast ramp test for FCR-D generally indicate that the model overestimated the response speed of the Kaplan unit. For illustration, the change in active power after 7.5 s during ramp 5 is seen in Table 4.3. The theoretical activation is 0.86 times the theoretical steady-state activation, as described in Appendix A. In all but one case, the activation is overestimated heavily by the model. The same pattern is seen for the downward direction of Requirement 2 as well as both directions of Requirement 3. The simulated overshoot energy calculated for Requirement 4 was around half of the value calculated from the measurements. Thus many results support the notion that the simulation model responds too quickly.

In order to qualitatively study the behavior of the model, the deactivation test and fast ramp test of the FCR-D down ramp sequence with high load and high droop are shown. The deactivation test is seen in Figure 4.12. The measured response

Table 4.3: FCR-D upward activation after 7.5 s (ramp 5). Absolute values are used. The test version refers to the combination of load and droop, e.g. LH is low load and high droop. In order to pass Requirement 2, $\Delta P_{7.5s}$ must be larger than or equal to the required value. The error, indicated in square brackets, is relative to the measurement.

	Dynamic activation (MW)			Requirement 2	
Test version	Required	Measured	Simulated	Meas.	Sim.
LL	10.737	8.229	11.107 [+35.0%]	Fail	Pass
LH	5.274	6.457	6.873 [+6.4%]	Pass	Pass
HL	12.872	7.744	12.087 [+56.1%]	Fail	Fail
HH	6.848	5.446	8.394 [+54.1%]	Fail	Pass

seems to be delayed compared to the simulated response. The reasons for this will be investigated in section 4.2.6. As a consequence, the activation differs at the time of frequency zenith (marked by the dashed line). The simulated unit can return to P_{zenith} while performance mode is still active, but the real unit does not and must complete the deactivation in the slower stability mode. The slow return to baseline power in stability mode makes the final result very sensitive to small differences in P_{zenith}. Although the model responds faster than the real unit, qualitatively it seems to show similar behavior. For example, the initial response in the opposite direction is visible in both simulation and measurements, and the transition to stability mode is clear. The values calculated from this deactivation test are seen in Table 4.4.

Table 4.4: FCR-D downwards deactivation test values for high load (initial GV 0.75 pu, ca 33 MW) and high droop (8%). The values correspond to the test shown in Figure 4.12.

	$\lvert\Delta P_{\text{zenith}}\rvert$ (MW)	$\lvert E_{\text{overshoot}}\rvert$ (MWs)
Simulation	2.924	12.296
Measurement	1.544	29.335

In the fast ramp test seen in Figure 4.13, it is also clear that the simulated unit responds faster than the real unit. The response seems to start earlier and the power is ramped more rapidly. Thus the change in power and the activated energy 7.5 s after the start of the ramp (marked by the dashed line) are markedly higher in the simulation, as seen in Table 4.5.

On average, $|\Delta P_{7.5s}|$ and $|E_{7.5s}|$ were overestimated by 46.6% by the model, while $|E_{\text{overshoot}}|$ was underestimated by 49.2%. The confusion matrix for Requirements 2, 3, and 4 in Figure 4.14 further emphasizes the faster performance of the simulated unit. Out of 21 requirements that were not fulfilled in the real tests, 12 were incorrectly predicted to pass by the model. Out of the tests that were correctly predicted as failing, deactivation tests make up the majority. Despite the faster response of the simulated unit, it still did not reach low enough levels of overshoot energy to

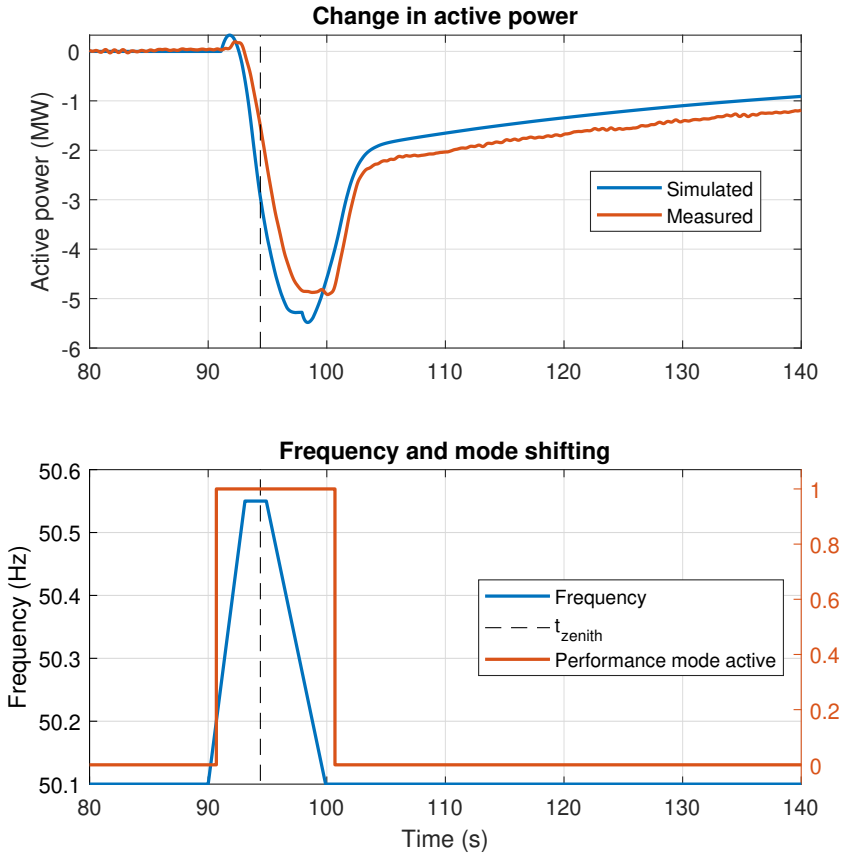

Figure 4.12: FCR-D downwards deactivation test for high load (initial GV 0.75 pu, ca 33 MW) and high droop (8%). The nominal head of the turbine is 33 m and the nominal power is 48 MW. The actual head is 33.4 m.

Table 4.5: FCR-D downwards fast ramp test values for high load (initial GV 0.75 pu, ca 33 MW) and high droop (8%). The values correspond to the test shown in Figure 4.13.

	$\lvert\Delta P_{7.5s}\rvert$ (MW)	$\lvert E_{7.5s}\rvert$ (MWs)
Simulation	7.677	23.251
Measurement	6.098	14.640

pass the tests.

Finally, the distribution of errors for $|\Delta P_{7.5s}|$ and $|E_{7.5s}|$ is studied in Figure 4.15. The deactivation test is not included since a faster or slower response has an opposite effect on the errors in overshoot energy compared to these errors. The distribution is clearly skewed to the positive side, and the mean signed error of 46.6% seems close to the center of the distribution.

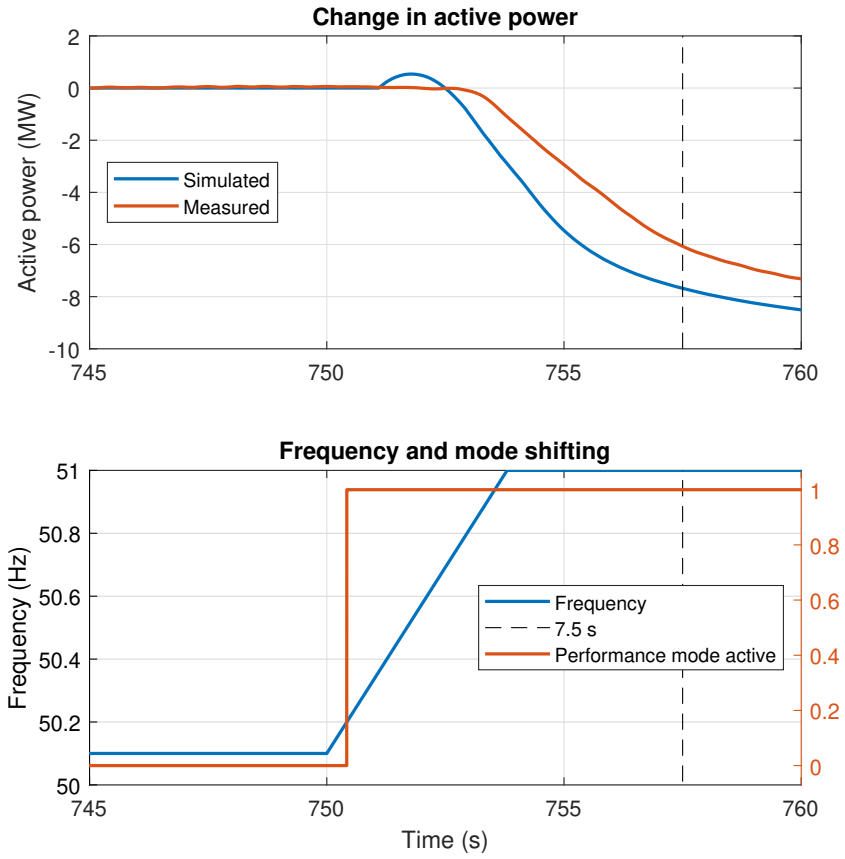

Figure 4.13: FCR-D downward fast ramp test for high load (initial GV 0.75 pu, ca 33 MW) and high droop (8%). The nominal head of the turbine is 33 m and the nominal power is 48 MW. The actual head is 33.4 m.

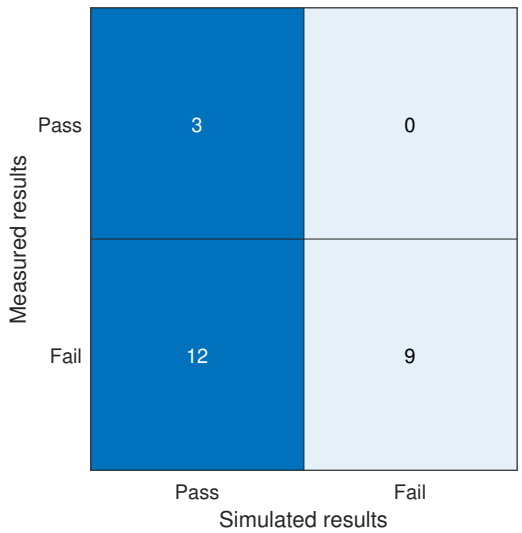

Figure 4.14: Confusion matrix for Requirements 2, 3, and 4, both directions.

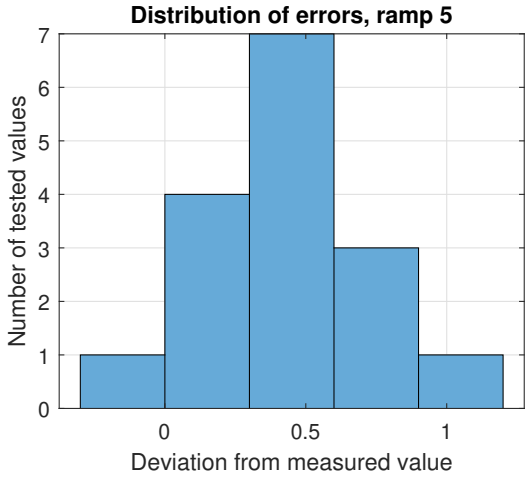

Figure 4.15: Prediction errors for $|\Delta P_{7.5\mathrm{s}}|$ and $|E_{7.5\mathrm{s}}|$.

4.2.5 Frequency Response Validation

After performing sine fitting on the active power during sine tests, Bode diagrams of the frequency response were constructed. These can be seen in Figures 4.16 and 4.17. They differ in amplitude, but behave similarly for the phase. Note that the phase is relative to the phase of the frequency error. The transfer function is equivalent to $F(j\omega)$ in Figure 2.2, so 0° would be equivalent to perfect immediate response to frequency deviations, and −180° would be equivalent to amplifying the frequency deviations.

In Figure 4.16, the amplitudes of the fitted sines from simulations are quite different from the ones in measurements. One explanation for this is that the operating point is 0.75 pu. As seen in Figure 4.5a, $\frac{\partial P}{\partial Y}$ in the simulation model is larger than in the reference data for the unit at this operating point. Thus the simulated unit will not have the same droop as the real unit in practice. The phase of the simulated unit is advanced compared to the real unit, again indicating a faster response.

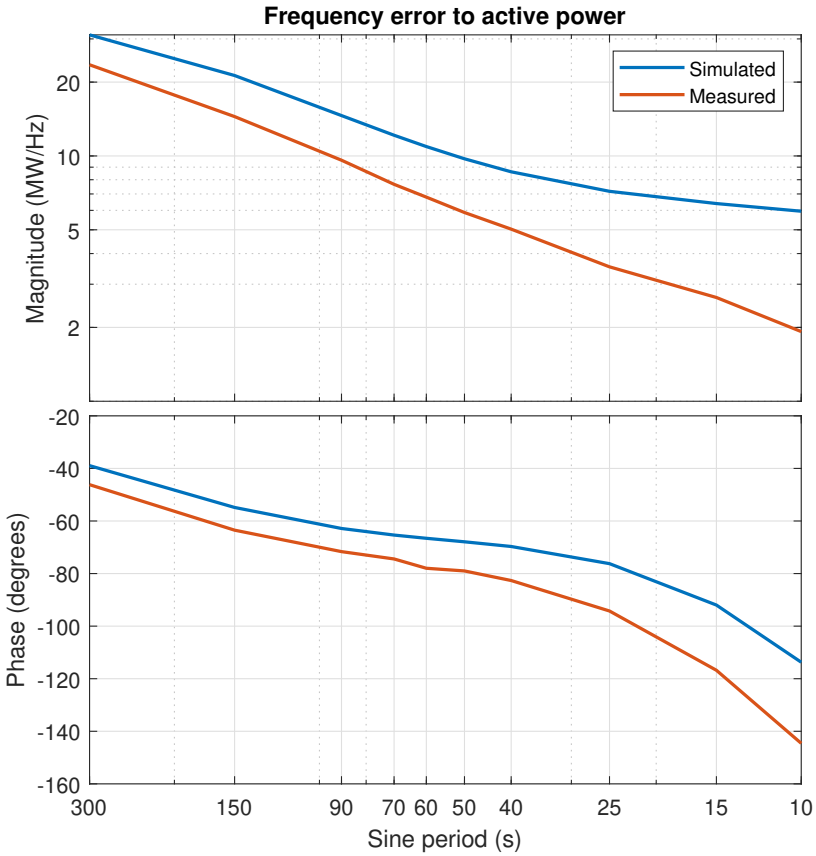

Figure 4.16: Bode diagram of the approximated transfer function between frequency error and active power during FCR-N sine tests $\left(\frac{\Delta P(j\omega)}{e(j\omega)}\right)$.

For FCR-D, the amplitude of the simulated response behaves much like the measured response. Following the same logic as above, near an operating point of 0.6 pu

the steady-state error in Figure 4.5a is constant, implying the same $\frac{\partial P}{\partial Y}$ (incremental gain) for both the simulations and the measurements. This could be why the amplitudes match for FCR-D but not for FCR-N. The phase is behaving similarly as above but the difference between simulations and measurements is even larger, particularly for the shortest sine periods.

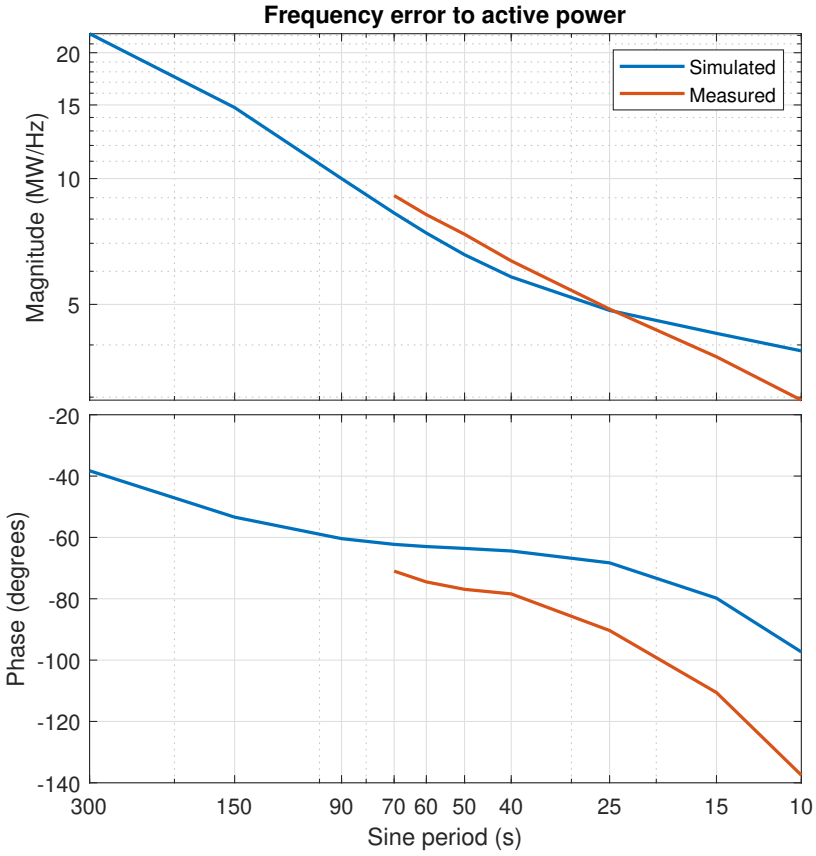

Figure 4.17: Bode diagram of the approximated transfer function between frequency error and active power during FCR-D sine tests $\left(\frac{\Delta P(j\omega)}{e(j\omega)}\right)$.

In the frequency domain, the source of the phase difference can be examined more closely. Since the guide vane and runner servo models had been validated and the simulated controller was identical to its real-world counterpart, the issue could be determined to exist between the servos and the active power output. That is, in the turbine characteristic or the waterways dynamics. Using the sinusoidal fits of the servo positions and active power, Bode diagrams could be constructed for the approximated transfer functions.

The Bode diagram seen in Figure 4.18 shows the approximated transfer function between guide vane position and active power output. A similar pattern as before is seen, where the real system seems slower than the simulated one. For shorter sine periods, the amplitude of the measurements is decreasing compared to the simulations. For the phase, there exists a difference across all studied frequencies,

but it also increases for shorter sine periods.

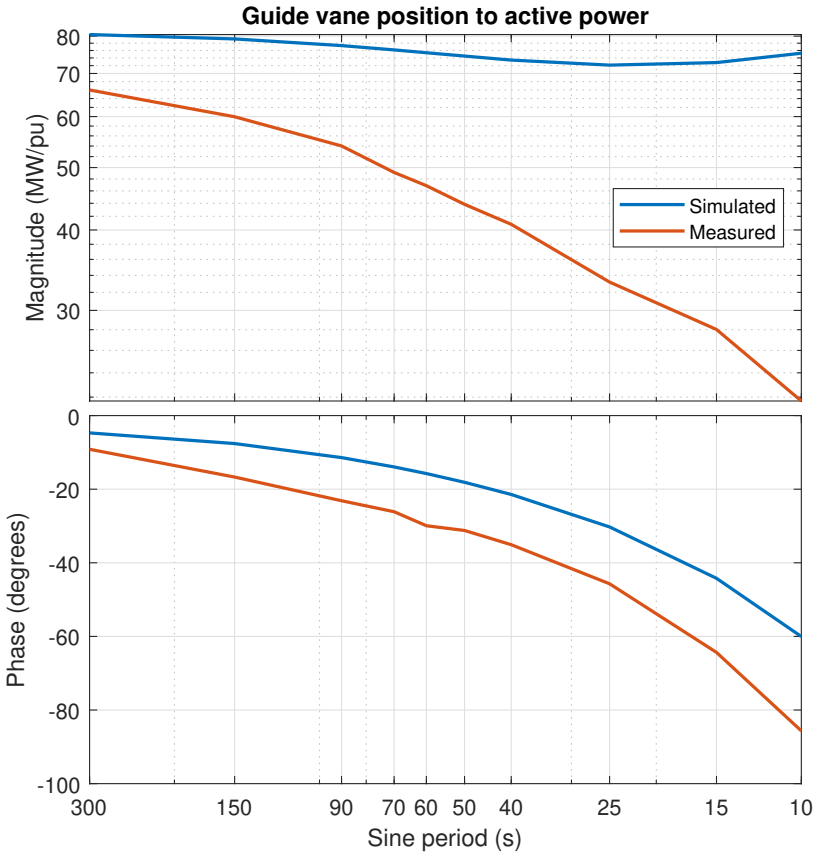

Figure 4.18: Bode diagram of the approximated transfer function from guide vane position to active power during FCR-N sine tests $\left(\frac{\Delta P(j\omega)}{\Delta \bar{Y}_{\text{mv}}(j\omega)}\right)$.

An interesting phenomenon is seen in Figure 4.19. In the Bode diagram for the approximated transfer function from runner blade angle $\bar{\alpha}$ to active power P, The difference between the simulation and measurement is similar to what was seen for the guide vane to power transfer function seen in Figure 4.18. However, here the phase difference between runner blade angle and active power is nearly constant and very small in the measurement data. This implies that in the real unit, active power closely follows the runner blade angle. The same can not be said for the simulated unit, as the phase of active power is actually ahead of the phase of runner blade angle, especially in the shorter sine periods.

For the FCR-D tests seen in Figure 4.20, the phase behaves similarly as for FCR-N. The phase difference between simulations and measurements is larger than for FCR-N, like it was for the response of the entire unit. The amplitude shows a smaller difference between simulations and measurements than for FCR-N. Again, this is similar to what was seen in the frequency response of the entire unit. The same reasoning about $\frac{\partial P}{\partial Y}$ at different operating points could be used to explain the difference.

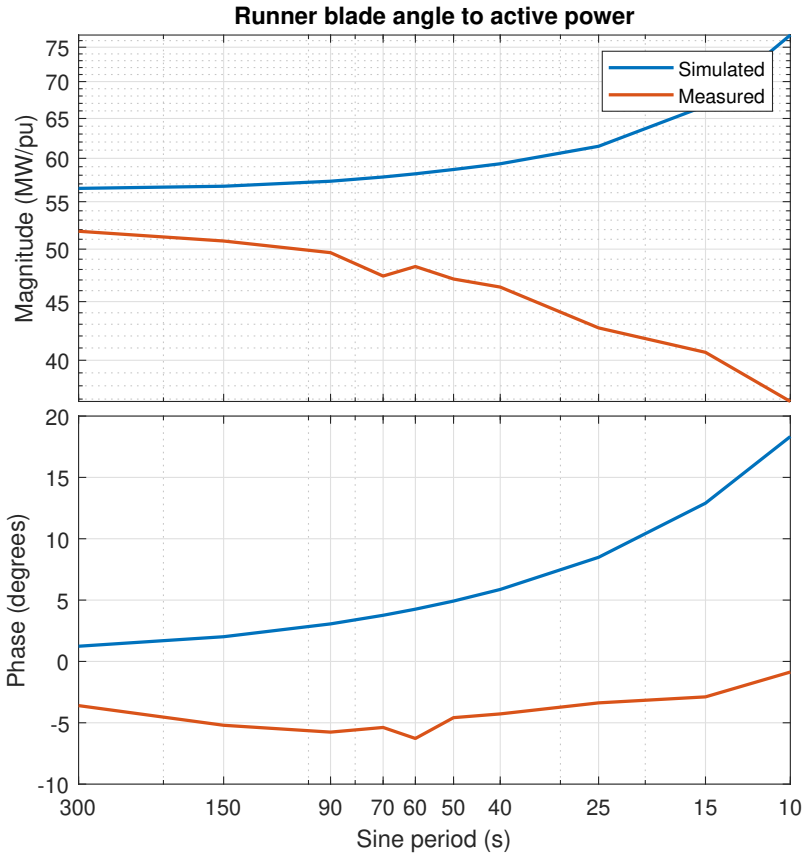

Figure 4.19: Bode diagram of the approximated transfer function from runner blade angle to active power during FCR-N sine tests $\left(\frac{\Delta P(j\omega)}{\bar{\alpha}_{\mathrm{mv}}(j\omega)}\right)$.

In summary, the frequency domain results imply the same as the dynamic time domain results: there is likely some delay or other dynamic in the real unit that is not modeled, and causes the real-world response to be slower than what is simulated. Possibly, the discrepancy could be related to a failure to capture the runner blade angle's impact on the dynamic response. In section 4.2.6, an attempt to characterize the missing component is presented.

4.2.6 Compensation for Unexplained Delay

Since the frequency domain data in Figures 4.16 to 4.20 showed that amplitude and phase decreased for shorter periods, it was hypothesized that the missing component may have a low-pass characteristic. Since the errors in amplitude were larger for the FCR-N sine tests, the FCR-D data was used to fit a suitable transfer function. Thus the frequency domain data seen in Figure 4.20 was fed to the System Identification Toolbox, with simulated data as input and measured data as output. As seen in section 4.2.2, the guide vane and runner blade movements were modeled well, so for this analysis the simulated guide vane position and runner blade angle are assumed

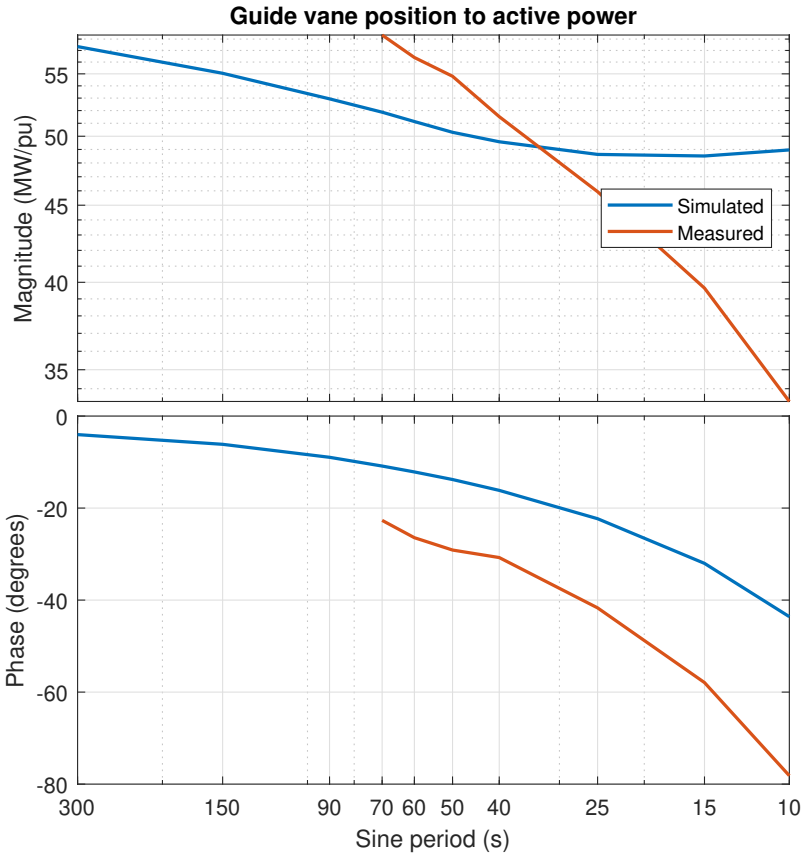

Figure 4.20: Bode diagram of the approximated transfer function from guide vane position to active power during FCR-D sine tests $\left(\frac{\Delta P(j\omega)}{\Delta \bar{Y}_{\mathrm{mv}}(j\omega)}\right)$.

to be the same as the measured values.

Since other factors were likely affecting amplitude and the incremental gain $\frac{\partial P}{\partial Y}$ varies over the operating range, the main concern was to capture the behavior of the phase. From initial attempts using all data points from the measurements, two observations were made. Firstly, the least squares fit of a transfer function must account for both phase and amplitude, so when looking at all sine periods the fitted transfer functions would sacrifice accuracy in phase at higher frequencies for lower frequency amplitudes and phases. Secondly, little to no improvement in fit was seen when fitting higher order transfer functions, so a simple transfer function with one pole and no zeros could be used.

Together with the fact that the shorter sine periods are more important for determining the stability margin, a first order transfer function was fitted using only the sine periods 25, 15, and 10 seconds. It can be noted that this narrow selection of data points in practice eliminated the possibility for higher order transfer functions anyway. The DC gain of the fitted transfer function was ignored since it would only be accurate for a limited part of the operating range. Thus the final filter used was

the one seen in Equation 4.2.

$$F_{\text{comp}}(s) = \frac{1}{1 + sT_{\text{comp}}} = \frac{1}{1 + 1.2387s} \tag{4.2}$$

The filter was applied to the output or input of the waterways subsystem separately, since the model of the waterways is not linear. The results were identical in the frequency domain, but in the time domain the qualitative behavior was slightly more similar to the measurements when the filter was placed at the input of the waterways subsystem, i.e. $\bar{G}$ in Figure 3.1. Therefore the latter variant was used.

As seen in Figure 4.21, the simulations now matched the phase of the measurements closely for the shortest sine periods. The simulated amplitude, although not prioritized, also followed the measurements more closely.

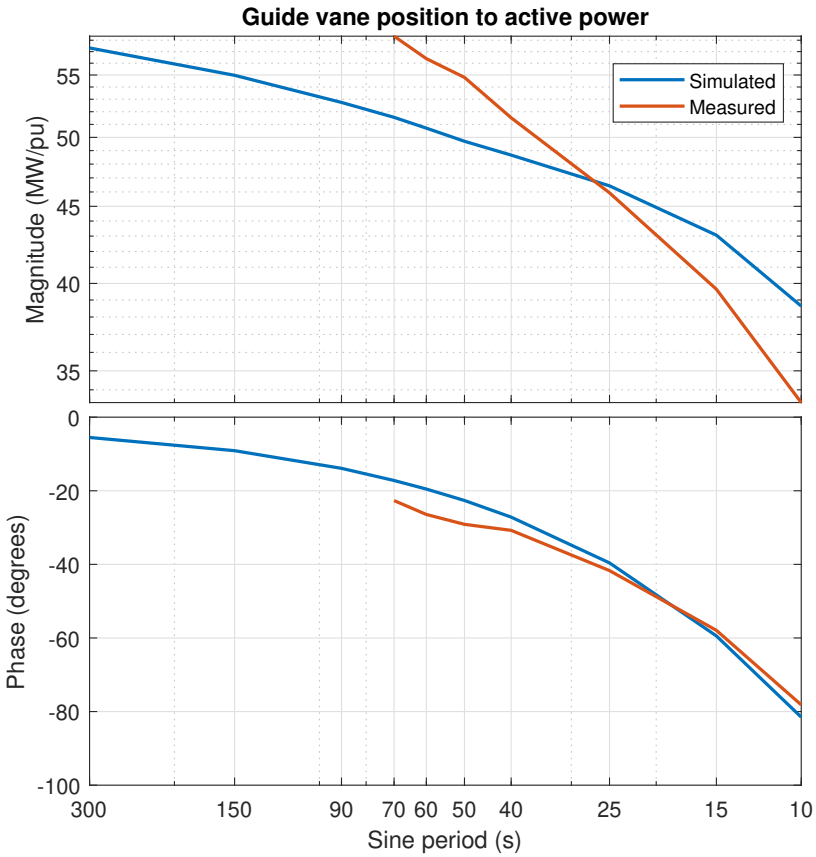

Figure 4.21: Bode diagram of the approximated transfer function from guide vane position to active power during FCR-D sine tests, compensated with low-pass filter $\left(\frac{\Delta P(j\omega)}{\Delta \bar{Y}_{\text{mv}}(j\omega)}\right)$.

The total frequency response of the simulated system was also more similar to the measurements after the filter was used. Especially the phase became closer to the measurements, as seen in Figures 4.22 and 4.23. For FCR-N, the difference

in amplitude remains, but for downward FCR-D the simulated amplitudes closely match the measured ones. No sine tests were performed for upward FCR-D.

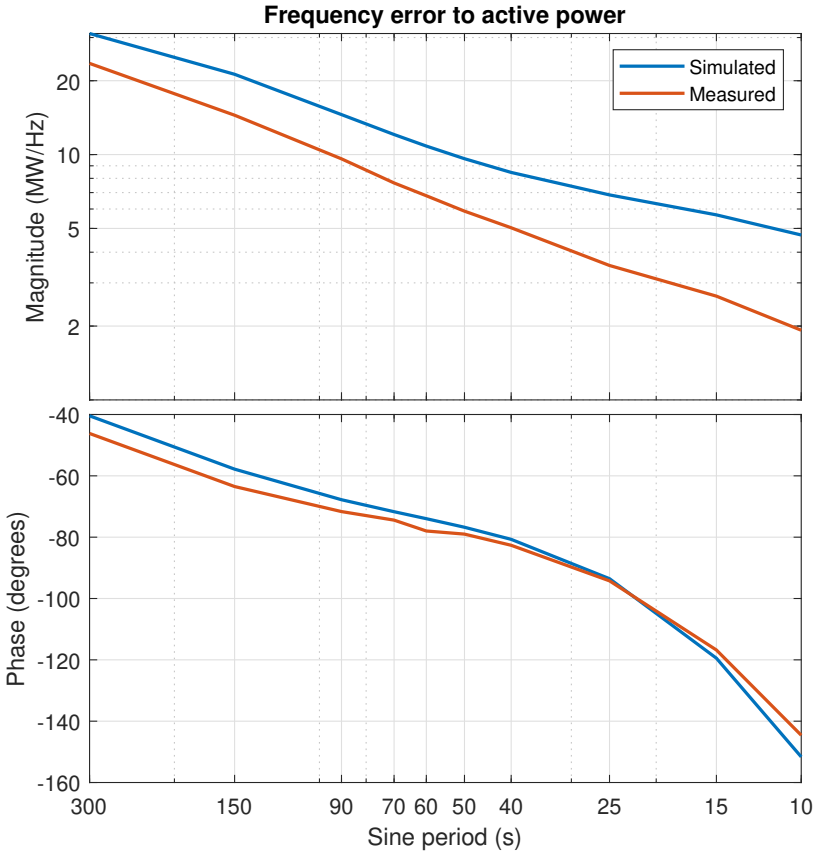

Figure 4.22: Bode diagram of the approximated transfer function between frequency error and active power during FCR-N sine tests, compensated with low-pass filter $\left(\frac{\Delta P(j\omega)}{e(j\omega)}\right)$.

As a consequence of using the filter, the dynamic time domain simulations also matched the measurements more closely. Specific examples can be seen in Appendix D.2, but aggregated results are presented here.

The mean signed error of all tests of $|\Delta P_{7.5\text{s}}|$ and $|E_{7.5\text{s}}|$ was 9.9%, compared to 46.6% before the filter was applied. For $|E_{\text{overshoot}}|$, the mean signed error was now 15.9%, compared to -49.2% before.

The effect could also be seen in the confusion matrix for Requirements 2, 3, and 4, seen in Figure 4.24. Many requirements that were previously incorrectly predicted as passed were now correctly predicted as failed. In total, 22 out of 24 dynamic requirements were correctly predicted. All tests predicted to fail by the model also failed in the real tests, which is useful for finding which tests are going to be challenging for a unit.

However, as seen with Requirement 4 before, the confusion matrix only provides

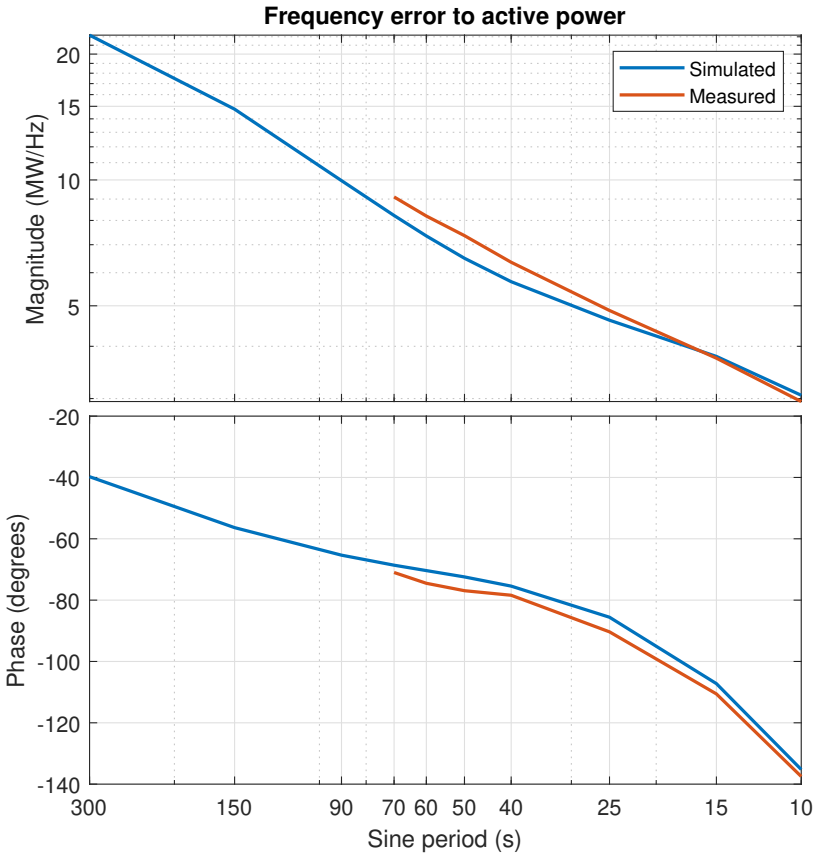

Figure 4.23: Bode diagram of the approximated transfer function between frequency error and active power during FCR-D sine tests, compensated with low-pass filter $\left(\frac{\Delta P(j\omega)}{e(j\omega)}\right)$.

meaningful statistics if the measurements are close enough to the required values for simulation errors to make a difference. It should thus prove useful to study the distribution of errors again. As before, overshoot energy is omitted. The distribution can be seen in Figure 4.25. Compared with before the filter was added, the distribution is less skewed to the positive side. Notably, 12 out of 16 simulated values are within 20% of the corresponding measured values.

Thus, whatever phenomenon that was not modeled in the original model is pretty well approximated by a first order low-pass filter. The time constant was found empirically (through system identification). The phenomenon can not be explained entirely by some input delay $e^{-s\sigma}$, since that would not affect the time derivative of the active power, which was seen to be different in simulations and measurements, like in Figures 4.12 and 4.13. Neither is an incorrectly estimated T_W likely. Increasing T_W in the model also increases the initial response in the opposite direction, which was not observed in the measurements. The fact that the real unit's active power output closely followed the runner blade angle (see Figure 4.19) could indicate that the low-pass filter approximates the effect of runner blade angle on the output.

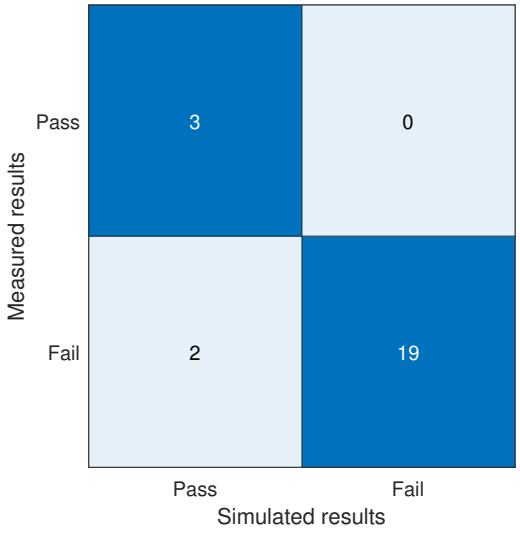

Figure 4.24: Confusion matrix for Requirements 2, 3, and 4, both directions, after low-pass filter was applied.

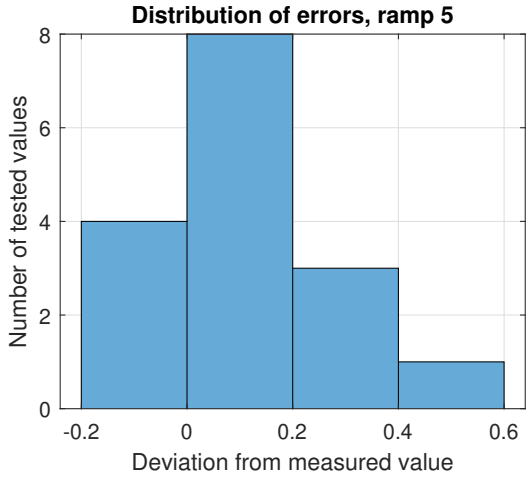

Figure 4.25: Prediction errors for $|\Delta P_{7.5\text{s}}|$ and $|E_{7.5\text{s}}|$, after low-pass filter was applied.

4.3 Sensitivity Analysis

In this section, results from the simulations investigating the sensitivity of key measurements with respect to the model parameters are presented. Using these results, the most important model parameters will be identified. First, the aggregated results in the form of standardized regression coefficients (SRCs) are presented along with the coefficient of determination r^2 for each output variable. From these, the most significant model parameters are identified.

In selected cases, scatter plots are shown in order to explain interesting results.

Note that since the low-pass filter modeled in the previous section could not be attributed to any known phenomenon, it was not included in the simulations performed for the sensitivity analysis. Out of the 500 simulations where model parameters were

randomly sampled on the distributions described in Table 3.3, 495 finished without crashes or errors.

4.3.1 Regression Modeling

Similarly to the validation results, these results are presented in terms of steady-state requirements, dynamic requirements and frequency domain requirements.

4.3.1.1 Steady-State Activation

We begin with the steady-state results, which are fairly straightforward. In Table 4.6, the results for steady-state activation of FCR-D are seen. As can be expected, no time constants, rate limits, or delays affect the steady-state behavior. Instead it is dominated by the mechanical backlash and servo dead band in the guide vanes. Interestingly, dead bands and backlash in the runner servo do not seem to have a significant impact. It seems like the turbine characteristic is not very punishing for slightly off-cam operation, i.e. not steep enough near the used combination curve to make a difference. A similar effect was actually seen earlier in Figure 4.2a, where smoothing the combination curve did not noticeably change the steady-state relationship between guide vane position and active power. The SRCs of the guide vane backlash and dead band are very close to each other, i.e. both parameters affect the steady-state activation approximately the same amount. This behavior was expected, since both parameters introduce a discrepancy between the guide vane setpoint and the actual position. Thus, as inputs to the regression model they are likely not orthogonal, that is, they do not affect the output in unique ways compared to each other. It is possible that one of the two variables is sufficient to describe the behavior. There is no obvious trend in the SRCs of backlash between different levels of droop. This is because each column is standardized separately, and all variance in the output can be attributed to the variance in backlash or dead bands.

4.3.1.2 Fast Ramp and Deactivation Test Results

From the fast ramp activation results in Table 4.7, we can note that the coefficient of determination is low for most outputs, indicating that the results relationship between parameters and outputs is not well described by a linear fit. This seems to be the case especially for the tests with low droop. Upon further inspection, the SRCs for the guide vane rate limits are also higher for these tests. It can also be seen that backlash and dead bands affect the results more during tests with high droop. This is because the backlash/dead band makes up a larger proportion of the activation when the amplitude of the activation is smaller. For example, during a full activation with high droop, the guide vane setpoint will move 0.1 pu due to the FCR-D controller while it will move 0.2 pu with low droop. The backlash is independent of droop, so with e.g. 0.005 pu of backlash it will limit the amplitude of the activation activation by 5% with high droop and 2.5% with low droop. Unlike in the steady-state results, other parameters also affect the output here, so the difference is not hidden by the standardization. Similar to the steady-state results however, is that the SRCs for backlash and dead band are very close to each other for

Table 4.6: Sensitivity of $|\Delta P_{\text{ss}}|$ for FCR-D. SRCs for each output and parameter. Positive values indicate that the measured value is increased if the parameter is increased, and vice versa. An SRC of 1 indicates that a change of 1 standard deviation in the parameter is associated with a change of 1 standard deviation in the result. The coefficient of determination r^2 indicates the goodness of fit for the linear regression, with 1 being the highest, separate for each measured value.

Direction	Downwards				Upwards			
Load	Low		High		Low		High	
Droop	Low	High	Low	High	Low	High	Low	High
T_W	0.05	0.05	0.00	0.00	0.05	0.00	0.00	0.00
$T_{s,\text{GV}}$	-0.01	-0.01	0.00	0.00	-0.01	0.00	0.00	0.00
$T_{s,\text{runner}}$	0.03	0.03	0.00	0.00	0.03	0.00	0.00	0.00
$T_{\text{del,GV}}$	0.03	0.03	0.00	0.00	0.03	0.00	0.00	0.00
$T_{\text{del,runner}}$	0.02	0.02	0.00	0.00	0.02	0.00	0.00	0.00
BL_{GV}	-0.48	-0.47	-0.68	-0.67	-0.48	-0.67	-0.68	-0.69
BL_{runner}	0.02	0.02	0.01	-0.01	0.02	-0.01	0.01	0.03
$RL_{\text{GV,open}}$	0.01	0.01	0.00	0.00	0.01	0.00	0.00	0.00
$RL_{\text{runner,open}}$	-0.05	-0.05	0.00	0.00	-0.05	0.00	0.00	0.00
$RL_{\text{GV,close}}$	0.03	0.03	0.00	0.00	0.03	0.00	0.00	0.00
$RL_{\text{runner,close}}$	-0.01	-0.01	0.00	0.00	-0.01	0.00	0.00	0.00
DB_{GV}	-0.56	-0.55	-0.70	-0.71	-0.56	-0.71	-0.70	-0.68
DB_{runner}	0.05	0.05	0.01	-0.01	0.05	-0.01	0.01	0.03
r^2	0.60	0.57	1.00	1.00	0.60	1.00	1.00	1.00

the respective tests. Another observation that can be made is that the parameters of the runner servo overall have a much smaller effect on the outputs. The only significant contribution seems to be the rate limits for tests with low droop, which would follow the same logic as for the guide vanes.

In Table 4.7 there were some interesting results. The effects of droop, rate limits, and servo time constants are illustrated in Figures 4.26 and 4.27, for low and high droop respectively. In the tests with low droop, $|\Delta P_{7.5\text{s}}|$ was highly dependent on the rate limit when the limit was very low, but beyond that there was no discernible effect. The linear fit was of course affected across the entire domain. In Figure 4.26a, there are some values of $|\Delta P_{7.5\text{s}}|$ far below the fitted line. These likely correspond to the leftmost data points in Figure 4.26b. These points are likely also the reason for the much lower r^2 for the tests with low droop. When studying the results from the tests with high droop in Figure 4.27, the same effect is not visible. The effect of the servo time constant is more pronounced, and there is close to no effect from the rate limit. It seems the rate limiter is not activated during the smaller ramps in tests with high droop.

In Table 4.8, the activated energy during the fast ramps is studied. Interestingly, the linear regression fits better for this set of outputs than for activated power.

Table 4.7: Sensitivity of $|\Delta P_{7.5s}|$ for FCR-D. SRCs for each output and parameter. Positive values indicate that the measured value is increased if the parameter is increased, and vice versa. An SRC of 1 indicates that a change of 1 standard deviation in the parameter is associated with a change of 1 standard deviation in the result. The coefficient of determination r^2 indicates the goodness of fit for the linear regression, with 1 being the highest, separate for each measured value.

Direction	Downwards				Upwards			
Load	Low		High		Low		High	
Droop	Low	High	Low	High	Low	High	Low	High
T_W	-0.06	0.02	-0.17	-0.46	-0.38	-0.55	-0.52	-0.73
$T_{s,\mathrm{GV}}$	-0.09	-0.08	-0.21	-0.38	-0.22	-0.41	-0.19	-0.34
$T_{s,\mathrm{runner}}$	0.01	0.03	0.07	0.02	-0.06	-0.06	-0.06	-0.01
$T_{\mathrm{del,GV}}$	-0.01	0.01	-0.09	-0.31	-0.19	-0.33	-0.18	-0.29
$T_{\mathrm{del,runner}}$	0.00	0.02	0.03	0.02	-0.04	-0.06	-0.05	-0.02
BL_{GV}	-0.23	-0.49	-0.20	-0.52	-0.14	-0.45	-0.11	-0.38
BL_{runner}	0.01	0.02	0.03	0.01	-0.02	-0.02	-0.03	0.00
$RL_{\mathrm{GV,open}}$	-0.02	0.01	-0.01	0.00	0.38	0.03	0.35	0.02
$RL_{\mathrm{runner,open}}$	0.04	-0.05	-0.01	-0.01	0.12	0.01	0.22	0.01
$RL_{\mathrm{GV,close}}$	0.26	0.03	0.39	0.02	0.06	0.01	0.05	0.01
$RL_{\mathrm{runner,close}}$	-0.07	-0.01	-0.18	-0.01	0.01	0.00	0.02	0.00
DB_{GV}	-0.20	-0.56	-0.23	-0.53	-0.22	-0.49	-0.18	-0.39
DB_{runner}	0.00	0.06	0.07	0.02	0.03	-0.02	0.02	0.00
r^2	0.18	0.61	0.35	0.99	0.42	0.97	0.51	0.96

This could indicate that the activated energy is dictated to a larger degree by linear components. However, the same pattern as in Table 4.7, where tests with low droop had lower r^2, is also seen here. The SRCs for the water time constant and guide vane servo time constant are overall higher than in Table 4.7. The same is true for the guide vane delay. The effect of the water time constant can be easily explained, as a larger T_W increases the initial pressure change, which in turn leads to the power output initially going in the opposite direction of activation, as seen in Figure 4.13. Similarly to the previous results, runner parameters affect the results much less than the guide vane parameters. There is also no clear difference between the effect of backlash and servo dead band.

The overshoot energy is mostly affected by the water time constant, guide vane servo time constant, and guide vane delay, as seen in Table 4.9. The effects of backlash and dead band seem to be smaller than in the previous tests. The rate limits also do not seem to affect to affect the outputs as much. Thus, the overshoot energy seems to be mostly dictated by time constants and delays, but the coefficient of determination is not as high as for $|E_{7.5s}|$. This could be a consequence of the design of the test itself, as the calculation of overshoot energy is a bit complicated, with e.g. changing integration limits.

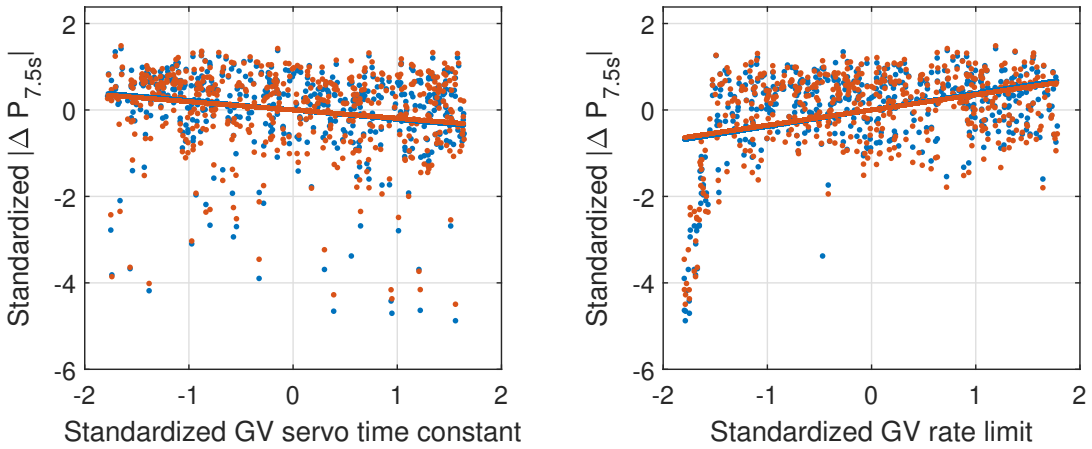

(a) $|\Delta P_{7.5s}|$ vs. Servo time constant. **(b)** $|\Delta P_{7.5s}|$ vs. Servo rate limit.

Figure 4.26: $|\Delta P_{7.5s}|$ vs. guide vane servo time constant and rate limit, low droop (4%), for upward FCR-D. The plots show how the activated power during the fast ramp test is affected by the two model parameters. The values are standardized to have zero mean and a standard deviation of 1 for easier comparison of different parameters.

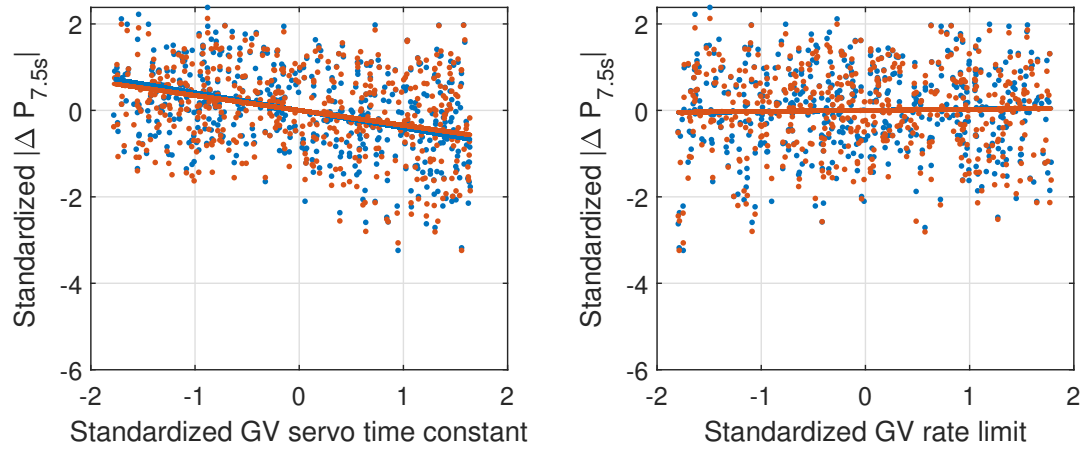

(a) $|\Delta P_{7.5s}|$ vs. Servo time constant. **(b)** $|\Delta P_{7.5s}|$ vs. Servo rate limit.

Figure 4.27: $|\Delta P_{7.5s}|$ vs. guide vane servo time constant and rate limit, high droop (8%), for upward FCR-D. The plots show how the activated power during the fast ramp test is affected by the two model parameters. The values are standardized to have zero mean and a standard deviation of 1 for easier comparison of different parameters.

Table 4.8: Sensitivity of $|E_{7.5s}|$ for FCR-D. SRCs for each output and parameter. Positive values indicate that the output is increased if the parameter is increased, and vice versa. An SRC of 1 indicates that a change of 1 standard deviation in the parameter is associated with a change of 1 standard deviation in the output. The coefficient of determination r^2 indicates the goodness of fit for the linear regression, with 1 being the highest, separate for each output.

Direction	Downwards				Upwards			
Load	Low		High		Low		High	
Droop	Low	High	Low	High	Low	High	Low	High
T_W	-0.56	-0.57	-0.67	-0.78	-0.65	-0.73	-0.82	-0.90
$T_{s,\mathrm{GV}}$	-0.37	-0.45	-0.35	-0.39	-0.34	-0.41	-0.26	-0.27
$T_{s,\mathrm{runner}}$	0.04	0.03	0.06	0.03	-0.03	-0.04	-0.03	-0.02
$T_{\mathrm{del,GV}}$	-0.36	-0.46	-0.34	-0.43	-0.41	-0.47	-0.34	-0.34
$T_{\mathrm{del,runner}}$	0.02	0.03	0.04	0.04	-0.05	-0.04	-0.05	-0.03
BL_{GV}	-0.15	-0.32	-0.13	-0.26	-0.13	-0.27	-0.11	-0.18
BL_{runner}	0.02	0.02	0.03	0.01	-0.01	-0.01	-0.01	-0.01
$RL_{\mathrm{GV,open}}$	-0.03	0.00	-0.02	-0.01	0.31	0.04	0.25	0.03
$RL_{\mathrm{runner,open}}$	0.01	-0.02	0.00	0.00	0.04	0.00	0.08	0.00
$RL_{\mathrm{GV,close}}$	0.37	0.07	0.35	0.05	0.04	0.00	0.03	0.00
$RL_{\mathrm{runner,close}}$	-0.05	-0.01	-0.08	-0.02	0.01	0.00	0.01	0.00
DB_{GV}	-0.16	-0.36	-0.16	-0.26	-0.15	-0.28	-0.11	-0.19
DB_{runner}	0.01	0.03	0.03	0.01	0.03	-0.01	0.01	-0.01
r^2	0.66	0.91	0.74	0.98	0.77	0.98	0.86	0.99

Table 4.9: Sensitivity of $|E_{\text{overshoot}}|$ for FCR-D. SRCs for each output and parameter. Positive values indicate that the output is increased if the parameter is increased, and vice versa. An SRC of 1 indicates that a change of 1 standard deviation in the parameter is associated with a change of 1 standard deviation in the output. The coefficient of determination r^2 indicates the goodness of fit for the linear regression, with 1 being the highest, separate for each output.

Direction	Downwards				Upwards			
Load	Low		High		Low		High	
Droop	Low	High	Low	High	Low	High	Low	High
T_W	0.62	0.60	0.66	0.66	0.75	0.66	0.81	0.80
$T_{s,\text{GV}}$	0.34	0.39	0.33	0.35	0.37	0.38	0.30	0.31
$T_{s,\text{runner}}$	0.01	0.02	-0.01	0.01	0.02	0.03	0.00	0.01
$T_{\text{del,GV}}$	0.44	0.49	0.41	0.43	0.53	0.49	0.43	0.37
$T_{\text{del,runner}}$	-0.03	0.00	-0.04	-0.01	0.03	0.03	0.02	0.05
BL_{GV}	0.07	0.11	0.06	0.12	0.06	0.11	0.06	0.13
BL_{runner}	0.01	0.02	0.00	0.00	0.02	0.02	0.01	0.02
$RL_{\text{GV,open}}$	0.00	0.00	0.00	0.01	-0.08	-0.01	-0.01	0.03
$RL_{\text{runner,open}}$	0.03	-0.01	0.03	0.00	0.03	-0.01	0.05	-0.01
$RL_{\text{GV,close}}$	-0.13	-0.05	-0.11	-0.04	-0.03	-0.03	-0.03	-0.01
$RL_{\text{runner,close}}$	-0.03	0.00	-0.04	-0.01	-0.01	-0.01	-0.01	-0.01
DB_{GV}	0.02	0.06	0.02	0.07	0.04	0.08	0.03	0.11
DB_{runner}	-0.05	-0.03	-0.05	-0.04	-0.02	-0.03	-0.02	0.01
r^2	0.63	0.68	0.65	0.69	0.88	0.74	0.85	0.81

4.3.1.3 Frequency Domain Requirements

Finally, we study the frequency domain requirements in Table 4.10. Here, the rate limits do not seem to affect the results. The sinusoidal frequency inputs seemingly do not cause very fast ramps. Thus the outputs are mostly affected by the time constants, delays and backlash/dead band. For the stability margin, measured in Requirement 8, T_W and backlash/dead band seem to be the most important parameters. The performance margin, Requirement 9, is very dependent on backlash/dead band and less on other parameters, but especially for FCR-N, T_W does affect the performance margin. Requirement 10, or the linearity of the unit's response, is included for two period lengths, 40 s and 10 s. The 40 s period is the shortest sine period for both products where the linear regression of Requirement 10 works. As can be seen for the 10 s period, r^2 is near zero, so the SRCs cannot be trusted. In practice this was likely caused by the fact that some simulations had such large dead bands and amounts of backlash that the deviation in power became zero during the shorter sine periods. The sinusoidal fit to the active power would then lead to nonsensical results for Requirement 10, since the amplitude of the fitted fine is used to normalize components other than the fundamental sine. For Requirement 9, r^2 is lower than for Requirement 8.

Table 4.10: Sensitivity of frequency domain results. SRCs for each output and parameter. Positive values indicate that the output is increased if the parameter is increased, and vice versa. An SRC of 1 indicates that a change of 1 standard deviation in the parameter is associated with a change of 1 standard deviation in the output. The coefficient of determination r^2 indicates the goodness of fit for the linear regression, with 1 being the highest, separate for each output.

Product	FCR-N				Downward FCR-D			
Requirement	8	9	10		8	9	10	
Period			40 s	10 s			40 s	10 s
T_W	-0.71	-0.25	-0.12	0.00	-0.40	-0.09	-0.06	-0.02
$T_{s,\mathrm{GV}}$	-0.25	-0.15	-0.01	-0.10	-0.23	-0.10	-0.01	-0.15
$T_{s,\mathrm{runner}}$	0.01	-0.01	-0.01	0.03	0.01	0.00	-0.01	0.01
$T_{\mathrm{del,GV}}$	-0.32	-0.10	0.00	0.00	-0.28	-0.07	0.00	-0.05
$T_{\mathrm{del,runner}}$	0.01	-0.01	-0.01	0.01	0.01	0.00	-0.01	0.00
BL_{GV}	-0.40	-0.61	-0.68	-0.24	-0.56	-0.64	-0.68	-0.22
BL_{runner}	0.00	0.01	0.00	-0.09	-0.01	0.02	0.01	-0.12
$RL_{\mathrm{GV,open}}$	0.00	0.00	0.00	0.05	0.00	0.00	0.00	0.05
$RL_{\mathrm{runner,open}}$	-0.02	0.04	0.01	-0.02	-0.01	0.03	0.01	0.03
$RL_{\mathrm{GV,close}}$	0.00	-0.01	0.00	-0.08	0.00	-0.01	0.00	-0.09
$RL_{\mathrm{runner,close}}$	0.01	-0.01	0.00	-0.02	0.01	0.00	0.00	-0.04
DB_{GV}	-0.43	-0.59	-0.69	-0.19	-0.60	-0.61	-0.69	-0.18
DB_{runner}	-0.01	0.01	0.01	-0.04	-0.01	0.02	0.01	-0.07
r^2	0.98	0.85	0.99	0.12	0.98	0.86	0.99	0.14

Mechanical backlash was seen to affect the performance requirement in Table 4.10. A separate sweep of only backlash was therefore performed. In Figure 4.28, this is studied. It is clear that backlash increases the peak around the 50 s period, to the point of failing the requirement for large values. For the longest sine periods, the backlash also worsens performance. Interestingly, for the shortest sine periods, performance is actually improved by backlash. This can possibly be explained by the fact that the phase shift of the unit's response is very large for those sines. Thus decreasing the amplitude of the response would be beneficial to the system. The same effects can be seen for the stability and sensitivity in Appendix D.3.

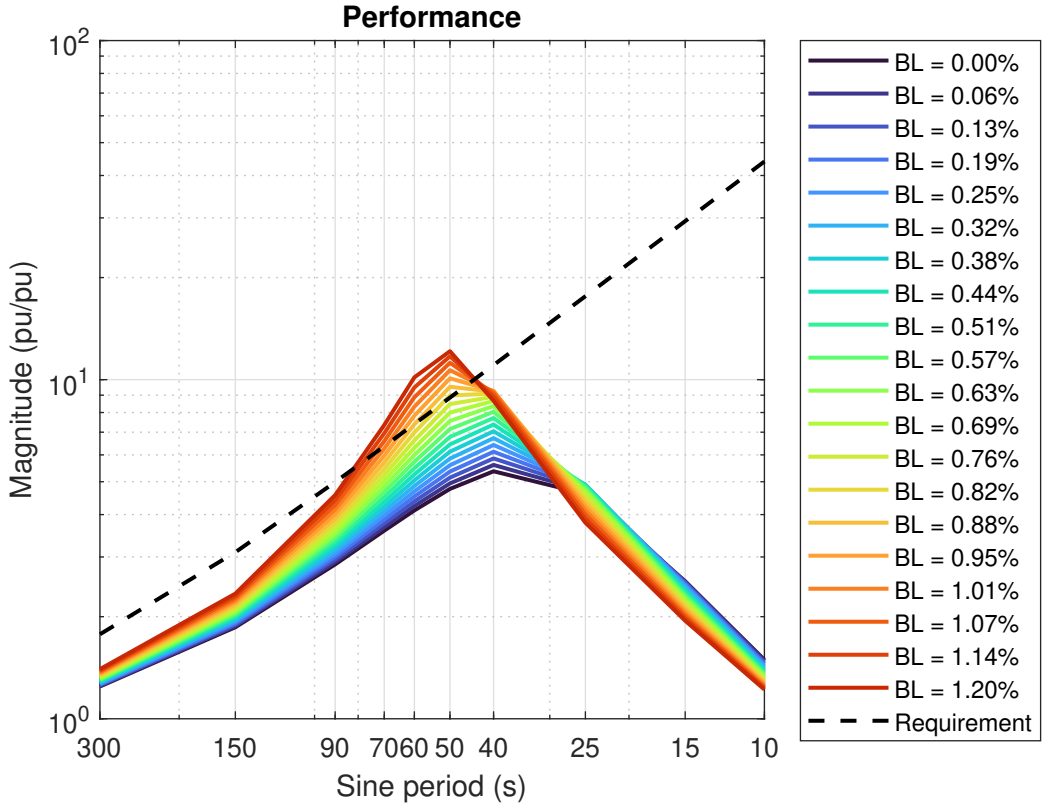

Figure 4.28: Disturbance suppression for different values of mechanical backlash in the guide vanes. $\left(G_c(j\omega) = \dfrac{G(j\omega)}{1 + F(j\omega)G(j\omega)} = \dfrac{\Delta\bar{f}(j\omega)}{d_P(j\omega)}\right)$.

Apart from backlash, the performance margin was also affected by the water time constant, especially for FCR-N, so a separate sweep of T_W was also performed. In Figure 4.29, T_W can be seen to increase the peak at 40 s. The sensitivity to disturbances at the very high and low ends is barely affected at all. It may not be intuitive that a time constant on the scale of one second can impact these sines, but as seen in Figure D.12 in the Appendix, the phase of the unit's response is affected by T_W for all sine periods.

In summary, the servo parameters for the guide vanes affected the results much more than those of the runner blades. The water time constant affected all dynamic requirements and frequency domain requirements. The dead band of the guide

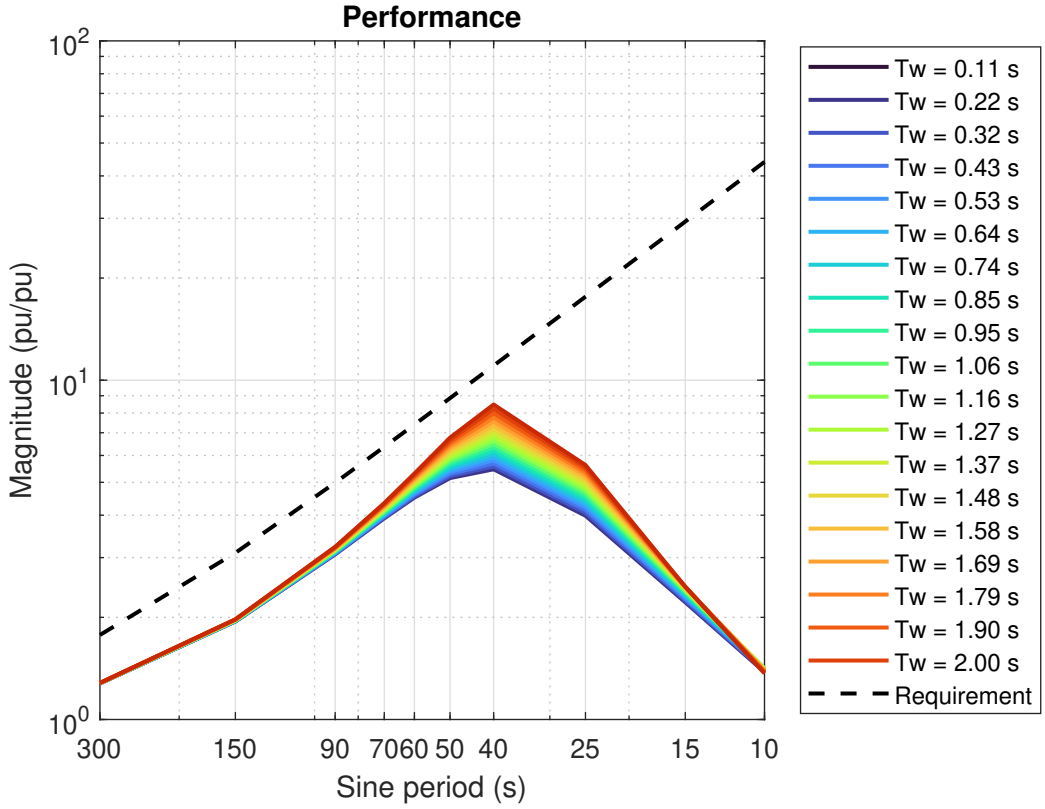

Figure 4.29: Disturbance suppression for different values of T_W. $\left(G_c(j\omega) = \dfrac{G(j\omega)}{1 + F(j\omega)G(j\omega)} = \dfrac{\Delta\bar{f}(j\omega)}{d_P(j\omega)}\right)$.

vane servo and the mechanical backlash affected the results in nearly exactly the same way. Information about backlash or dead bands from real plants can likely be encoded in a single parameter. The results are summarized in Table 4.11. In the real unit, the opening and closing rates were not found to differ. If they are considered the same parameter, the runner rate limit is counted, and only one of backlash or dead band is counted, six parameters are needed in order to use the model. Including nominal power and nominal and actual hydraulic head, a total of nine parameters are needed. Simulations were performed with the estimated runner servo parameters replaced with the mean values of their domains (see Table 3.3). The results can be seen in Appendix C (see the column for 'Sim B'). The results were very similar to those of the model with runner servo parameters estimated from measurements, with some exceptions. This model with 'guessed' runner parameters showed larger activations in the fast ramp tests with low droop. This was likely because the rate limit was higher, as that was the only parameter with any noticeable impact on results for the runner. It also aligns with the fact that the guide vane rate limit only affected the results in the tests with low droop.

The results for the runner servo parameters seen here, together with the results in section 4.2.6 and Figure 4.19 are indicative that the original model does not model the effects of runner blade angle properly.

Table 4.11: Domain of model parameters for the sensitivity analysis.

Parameter	Significant	Comment
T_W	Yes	
$T_{s,\text{GV}}$	Yes	
$T_{s,\text{runner}}$	No	
$T_{\text{del,GV}}$	Yes	
$T_{\text{del,runner}}$	No	
BL_{GV}	Yes	Same effect as dead band
BL_{runner}	No	
$RL_{\text{GV,open}}$	Yes	
$RL_{\text{runner,open}}$	Maybe	Only for $\lvert\Delta P_{7.5\text{s}}\rvert$
$RL_{\text{GV,close}}$	Yes	
$RL_{\text{runner,close}}$	Maybe	Only for $\lvert\Delta P_{7.5\text{s}}\rvert$
DB_{GV}	Yes	Same effect as backlash
DB_{runner}	No	

4.4 Control Improvements

In this section, the results from the proposed control improvements are presented. This is divided into FCR controller tuning, servo tuning, and active power feedback. The consequences on water flow from tuning is also analyzed.

4.4.1 Tuning Parameters of Current Implementation

During these simulations, the first order filter developed in Section 4.2.6 was kept in the model.

The parameters of the PI controller, K and T_{feedback} were varied simultaneously in order to find the best controller. The gain K was varied between 0.1 and 1.0, where the original value was 0.25. The time constant T_{feedback} was varied between 2 s and 50 s. The default time constant was 31 s. The ranges were split into 19 evenly spaced points, for a total of 361 parameter sets to test.

The resulting stability margins for all tests can be seen in Figure 4.30. Generally, it can be seen that stability is reduced for lower controller time constants. A faster controller will lead to higher loop gain at high frequencies, and therefore the sensitivity at those frequencies is increased. When varying controller gain K, the stability margin is highest near $K = 0.30$. Some proportional action is needed for damping, but higher gain increases control action too much, which worsens stability. The effects on the transfer functions themselves of varying K and T_{feedback} can be seen in Appendix D.5.

The performance margin, represented as $(|D(j\omega)|^{-1} - |G_c(j\omega)|)/(|D(j\omega)|^{-1})$ at the sine period with the worst performance, is seen in Figure 4.31. Lower values of T_{feedback} generally lead to better disturbance suppression, especially at lower frequencies. This is explained by the stronger integral action. The relationship between

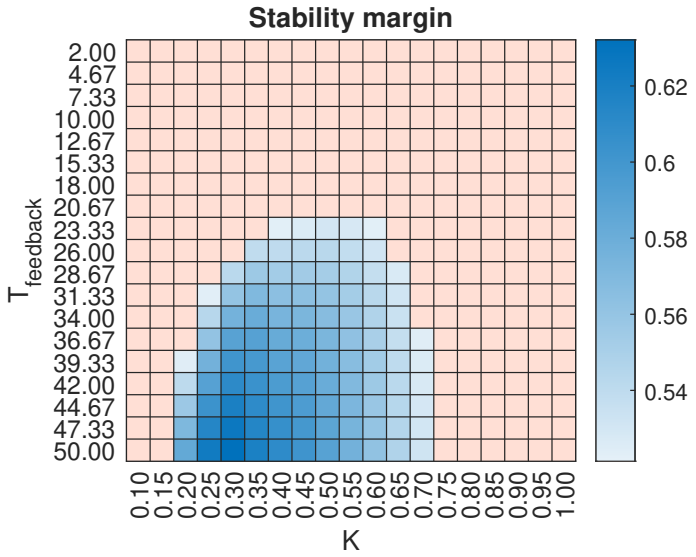

Figure 4.30: Stability margin of downward FCR-D sine tests for different controller values. Pink squares signify controller parameters where the stability margin was smaller than with the original controller.

K and the performance requirement is less pronounced. The performance requirement is not met for very low values of K but the difference in margin between e.g. $K = 0.3$ and $K = 1.0$ is not very large. The gain improves damping for the 60 s period, but once sufficient damping of that frequency has been achieved, the performance margin is mostly limited at the lower frequencies less affected by K. This can be observed in Figure 4.32.

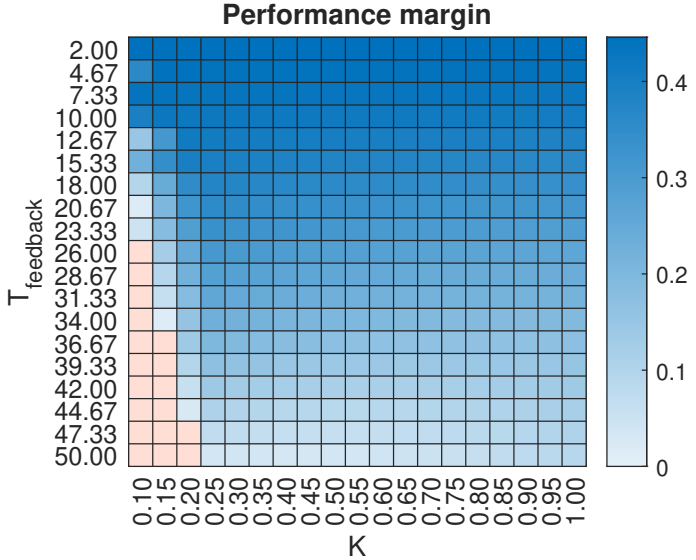

Figure 4.31: Performance margin of downward FCR-D sine tests for different controller values. Pink squares signify tests that failed Requirement 9.

The controller that achieved the highest performance margin while maintaining the same stability margin as the original controller had the parameters $K = 0.4$

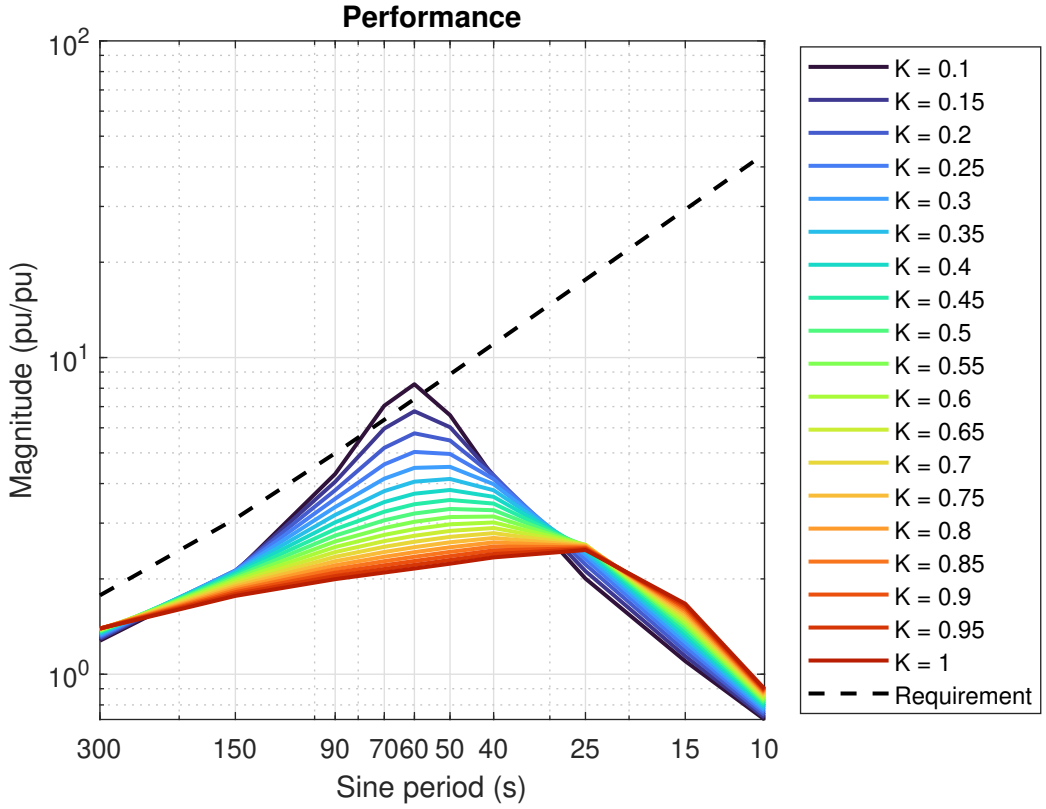

Figure 4.32: The effect of proportional gain on the performance requirement. For very low K, the unit can not adequately suppress disturbances with a 60 s period. T_{feedback} fixed at 31.33 s.

$T_{\text{feedback}} = 23.33$ s. However, this is only true for FCR-D. Using the same controller parameters during the FCR-N sine tests leads to a decreased stability margin. In Figure 4.33 we see the parameter combinations that achieve the criterion of improved or maintained stability, for both FCR-N and FCR-D. When FCR-N is taken into account, there is no way to increase integral action without lowering the stability margin.

However, K can be increased from 0.25 to 0.35. Looking closely at Figure 4.31, this would actually very slightly lower the performance margin. Although, the performance margin is at this point determined by the behavior at the 300 s period. If we instead study Figure 4.32 again, it can be clearly seen that changing K from 0.25 to 0.35 lowers the peak around 60 s, which is desirable. The tests that fail usually do so near this sine period. Thus the new stability mode parameters are chosen to be $K = 0.35$ and $T_{\text{feedback}} = 31.33$ s.

With the stability mode parameters selected, the effect of changing T_{feedback} in performance mode was studied. Proportional gain was unchanged from stability mode. Sweeping T_{feedback} from 0.02 to 2.0, the results shown in figure 4.34 were obtained. Since performance mode only affects the fast ramp test and the deactivation test, only Requirements 2, 3 and 4 are studied. The requirements are averaged over all directions and test conditions. All requirements show improvements for values down

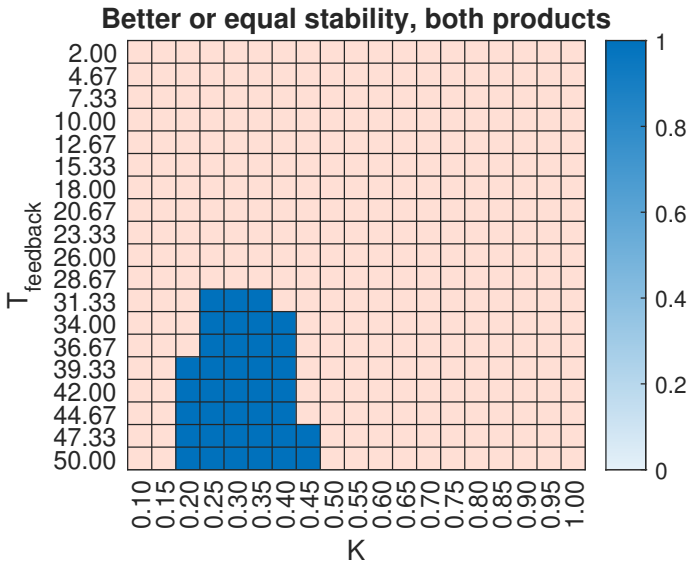

Figure 4.33: Controller parameters that maintain or improve the stability margin for both products. Pink squares signify controller parameters where the stability margin for either product was smaller than with the original controller. The viable set of parameters is much smaller than if just FCR-D is considered.

to 0.2 s. Requirement 2 does not improve further beyond that, likely due to the rate limiters in the servos. Requirement 4 especially seems to keep improving with lower T_{feedback}. However, it should be noted that for very fast control signals, the first order servo model may not be valid anymore. Lowering T_{feedback} below 0.2 s was not seen as a viable option, since a PI controller with droop with such a low feedback time would be nearly equivalent to a purely proportional controller. Thus 0.2 s was chosen.

4.4.2 Faster Servos

Changing the servo time constants from 0.8 s to 0.2 s predictably resulted in better performance. In addition to improving the responses themselves, it also allowed for more aggressive tuning while maintaining the same stability margins as the original settings. In Figure 4.35, we see that T_{feedback} can be decreased to 20.67 s with maintained stability margins. Similarly to the simulations with the slower servos, disturbance suppression in the 50 s - 70 s band was improved by increasing K although this was not captured by the performance margin value. Therefore, with the faster servos the stability mode parameters were chosen as $K = 0.45$ and $T_{\text{feedback}} = 20.67$ s.

For the performance mode, the effect on the dynamic requirements can be seen in Figure 4.36. Much like the simulations with slow servos, little improvements were seen for values of T_{feedback} below 0.2 s, so that was again the value chosen. Notably however, the results for Requirement 4 were much better for all values of T_{feedback} compared to Figure 4.34. It seems like improving the servo performance has a large effect, even when the FCR controller is not re-tuned.

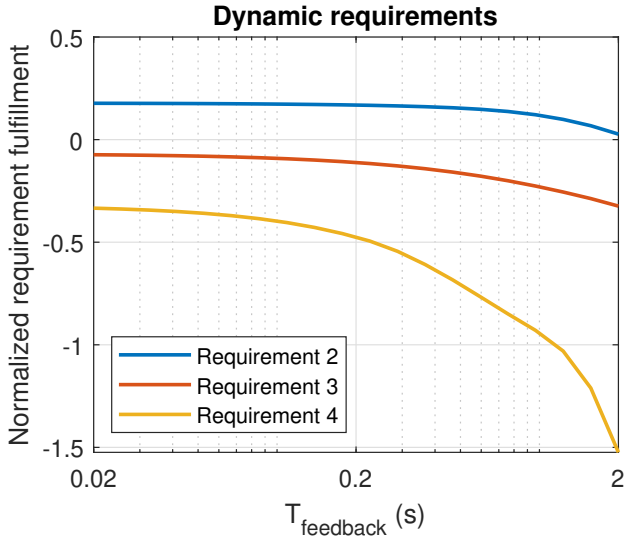

Figure 4.34: FCR-D dynamic requirements vs. T_{feedback} in performance mode. The requirements are normalized such that 0 marginally passes and larger values indicate better performance. E.g. for Requirement 2 0.1 would indicate that the required activation is exceeded by 10%. Note the logarithmic x-axis.

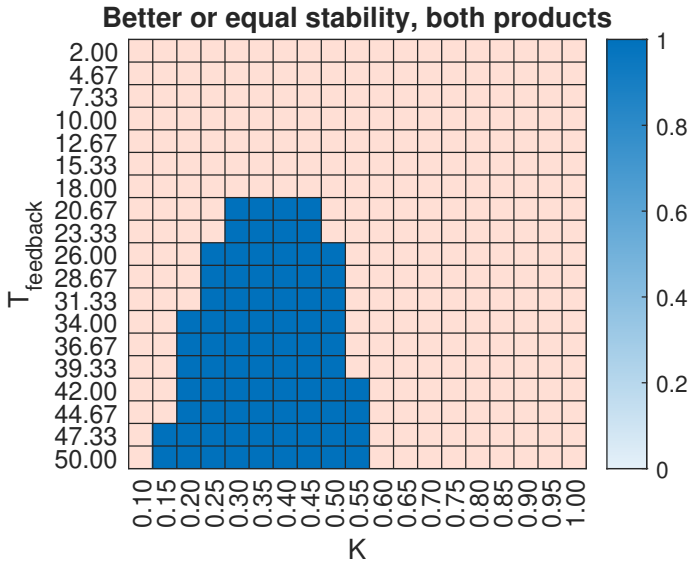

Figure 4.35: Controller parameters that maintain or improve the stability margin for both products, with faster servos. Pink squares signify controller parameters where the stability margin for either product was smaller than with the original controller and servos. The viable set of parameters is larger than for the slow servos.

In order to compare the improvements of tuning the FCR controller and tuning the servos, the results for Requirement 4 were compiled into Table 4.12. The base case represents the model used in validation, with the original controller parameters. T1 stands for the tuning obtained in Section 4.4.1. T2 represents the model with faster servos and original controller parameters. T3 is the version where both the

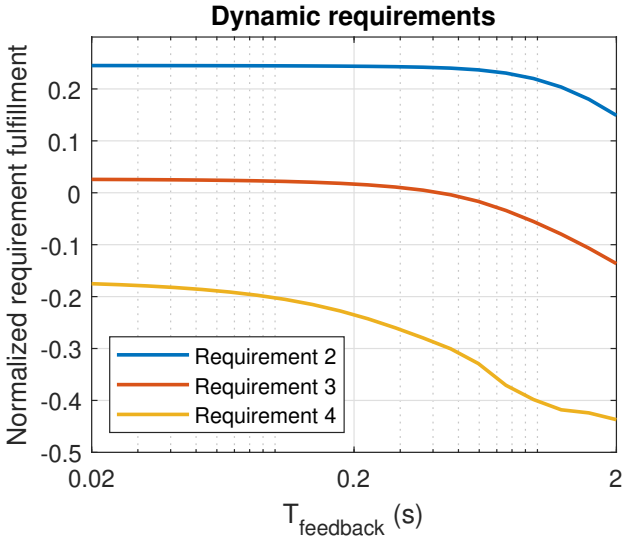

Figure 4.36: FCR-D dynamic requirements vs. T_{feedback} in performance mode with faster servos. The requirements are normalized such that 0 marginally passes and larger values indicate better performance. E.g. for Requirement 2 0.1 would indicate that the required activation is exceeded by 10%. Note the logarithmic x-axis.

servos and the controller were tuned. The parameters of the different tuning cases are compiled in Table 4.13. Both controller tuning and servo tuning resulted in large improvements by themselves, and the performance was improved further by combining both measures.

Table 4.12: Effects of controller tuning and faster servos on Requirement 4. The requirements are normalized such that 0 marginally passes and larger values indicate better performance. E.g. a value of -0.4 indicates that the maximum allowable overshoot energy is exceeded by 40%. The parameters for the different cases are presented in Table 4.13.

Direction	Load	Droop	Base	T1	T2	T3
Downwards	Low	Low	-1.14	-0.39	-0.39	-0.11
	Low	High	-1.12	-0.10	-0.42	-0.14
	High	Low	-1.66	-0.75	-0.71	-0.44
	High	High	-1.85	-0.43	-0.69	-0.27
Upwards	Low	Low	-0.82	-0.28	-0.33	-0.07
	Low	High	-1.18	-0.28	-0.44	-0.03
	High	Low	-1.45	-0.57	-0.68	-0.36
	High	High	-3.63	-1.01	-1.74	-0.46

The improvements were especially large for the FCR-D upwards test with high load and high droop. These are studied further in Figure 4.37. The base case for this test showed very poor performance, with 4.6 times the allowed overshoot energy. We see that both faster servos and more aggressive controllers increase the power at

Table 4.13: Controller and servo parameters for different tuning cases. The base case represents the model used in validation, with the original controller parameters. T1 stands for the tuning chosen with the original servos. T2 represents the model with faster servos and original controller parameters. T3 is the version where both the servos and the controller were tuned.

Parameter	Base	T1	T2	T3
K (stability)	0.25	0.35	0.25	0.45
K (performance)	0.25	0.35	0.25	0.45
T_{feedback} (stability)	31 s	31 s	31 s	21 s
T_{feedback} (performance)	1.9 s	0.2 s	1.9 s	0.2 s
T_s (both servos)	0.8 s	0.8 s	0.2 s	0.2 s

the time of frequency nadir, marked with a vertical line. Because of the slow return toward zero activation, small changes in P_{nadir} have large effects on the overshoot energy. A more aggressive controller also speeds up the deactivation enough to remove the entire lower, broader part of the integrated area.

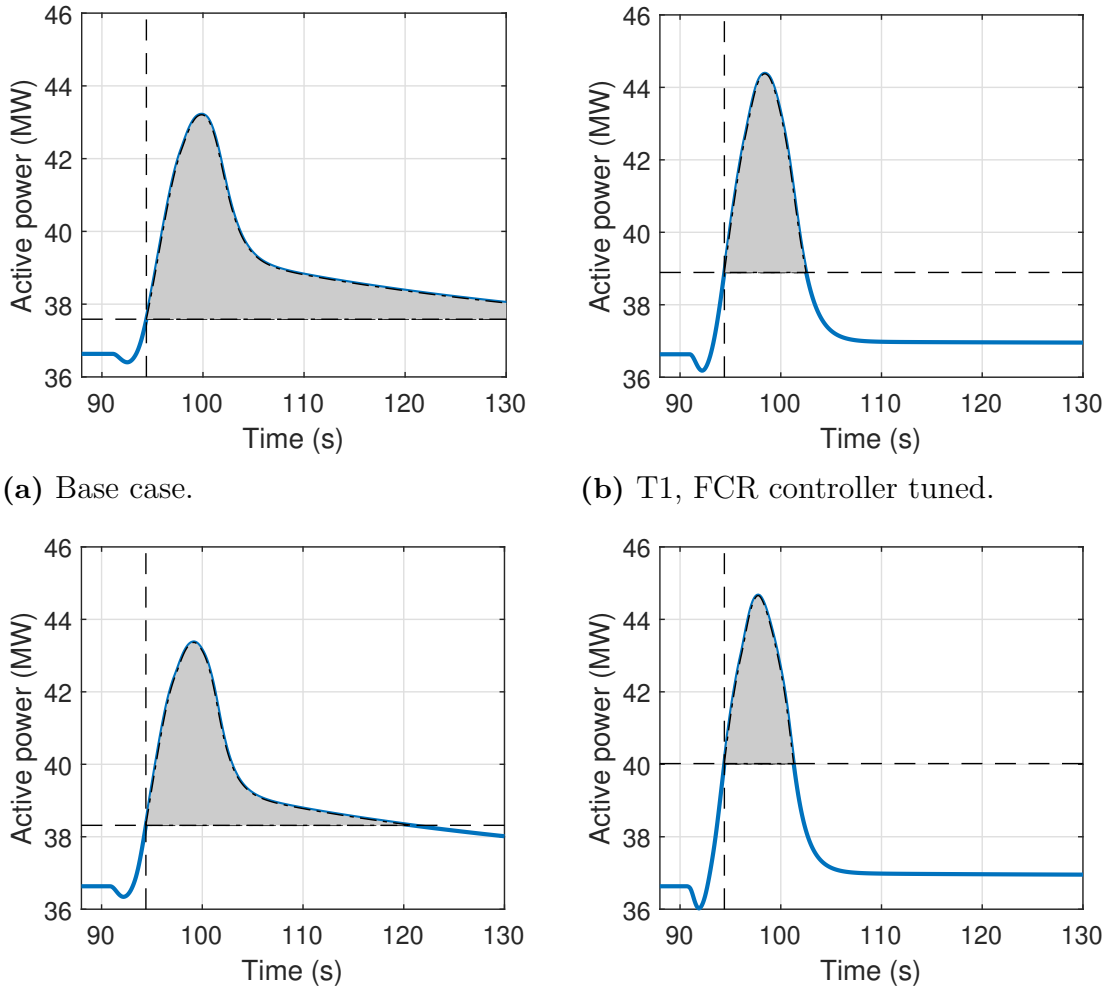

(a) Base case.

(b) T1, FCR controller tuned.

(c) T2, faster servos.

(d) T3, both controller and servos tuned.

Figure 4.37: Deactivation test, FCR-D upwards. Comparison between the different versions seen in Table 4.12. From the test with high load (initial GV 0.70 pu, ca 37 MW) and high droop (8%). The parameters for the tuning cases are seen in Table 4.13. The nominal head of the turbine is 33 m and the nominal power is 48 MW. The actual head is 33.4 m.

4.4.3 Active Power Feedback

After a few initial tests, the integration time constant T_P for the additional active power controller was chosen to be 30 s. Lower values would affect dynamic performance too much, and larger values led to additional corrective steps in the steady-state activation tests, due to the backlash.

The FCR-N step test for low load and high droop is seen in Figure 4.38. One difference that is clear immediately is the steady-state activation. The theoretical capacity is the same for the version with active power feedback and the version with tabulated guide vane feedback, which is different from the theoretical capacity for guide vane feedback, since the droop is the same but applied to active power instead of the guide vane setpoint. However, the tabulated version is affected by backlash the same way as the regular version with just guide vane feedback. The version with active power feedback returns to the original power during zero activation, while the other two are affected by backlash. This is reflected in Requirement 1, where the unit with active power feedback passed all tests. The unit with tabulated guide vane feedback did not improve over the base case.

The dynamic activations were also improved by the active power feedback, as seen in Table 4.14. The unit with tabulated guide vane feedback performed similarly to the base version. Since the active power feedback is fast enough to affect the dynamic performance, the concerns about counteracting the inertial response during real operation should be addressed. If we assume an inertia constant of 4 s (high for a hydro turbine) the initial inertial response during a ramp with a RoCoF of $-0.24\,\mathrm{Hz/s}$ such as ramp 5 would be:

$$\Delta P_{\text{inertia}} = -2H\frac{d\bar{f}}{dt} = 2 \cdot 4\,\mathrm{s} \cdot \frac{0.24\,\mathrm{Hz/s}}{50\,\mathrm{Hz}} = 0.0384\,\mathrm{pu}. \tag{4.3}$$

Assuming zero output from the controller, the active power feedback with $T_P = 30\,\mathrm{s}$ would change the guide vane setpoint with $-0.0384/30 = -0.001\,28\,\mathrm{pu/s}$. During the test with high droop, i.e. where the FCR controller ramps the slowest, the initial ramp rate of the controller was around $0.012\,\mathrm{pu/s}$, or an order of magnitude faster than $-0.001\,28\,\mathrm{pu/s}$. Thus, the counteraction to the inertial response would be negligible in the beginning and after around 3 s the active power feedback would actually start to amplify the response.

Table 4.14: FCR-D upward activation after 7.5 s (ramp 5), different feedback types. Normalized against Requirement 2 since $\Delta P_{\text{theoretical}}$ is changed.

Test version	Base version	Active power feedback	Tabulated GV feedback
LL	-0.14	0.06	-0.07
LH	0.07	0.47	0.07
HL	-0.24	0.22	-0.14
HH	-0.02	0.73	-0.05

In Figure 4.39, the ability to suppress load disturbances is compared in the frequency domain. That is, the transfer function from load disturbance d_P to frequency de-

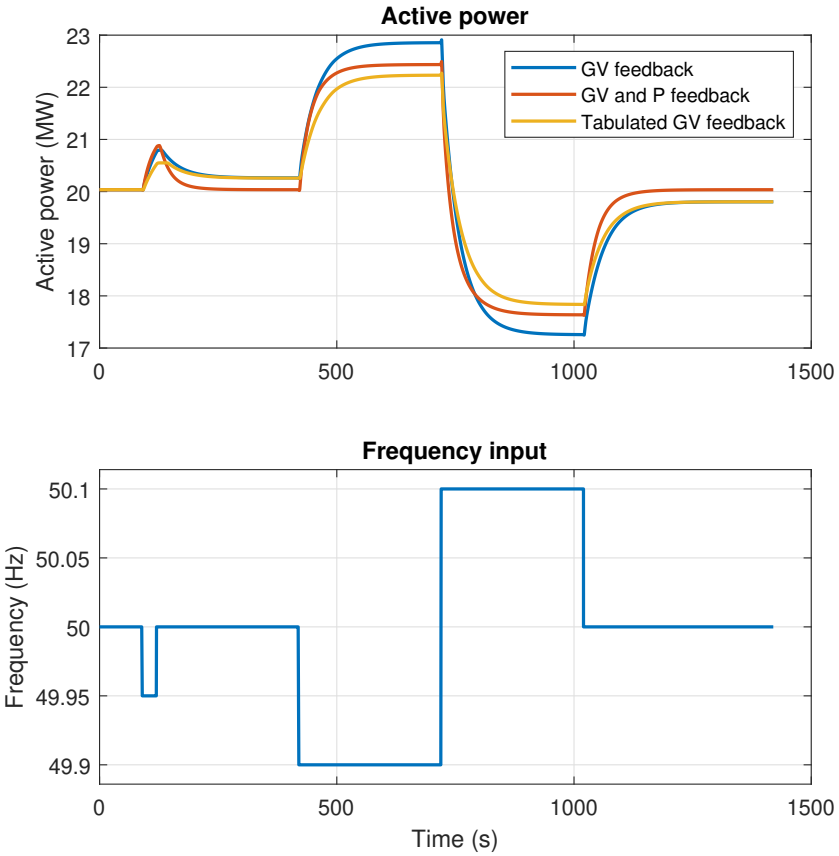

Figure 4.38: Comparison between different feedback types during a FCR-N step test with low load (initial GV 0.50 pu, ca 20 MW) and high droop (4%). The theoretical capacity for the model with GV feedback is 3.011 MW. For the other two models the theoretical capacity is 2.4 MW. The nominal head of the turbine is 33 m and the nominal power is 48 MW. The actual head is 33.4 m.

viation $\Delta\bar{f}$, $G_c(j\omega)$ The worst performance is seen from the unit with tabulated guide vane feedback, which fails the performance requirement. The unit with active power feedback performs better during the longer sine periods, but the peak is shifted to the 25 s period. This could be caused by the integration constant of 30 s and subsequent oscillations.

Finally in Figure 4.40 the drawback of active power feedback is seen. The unit fails the stability requirement, and the Nyquist curve constructed from the open loop transfer function $G_o(j\omega) = F(j\omega)G(j\omega)$ from frequency error (or reference) to frequency deviation even passes on the left side of $(-1, j0)$, meaning it would act to destabilize the grid. The tabulated guide vane feedback version also decreases the stability margin, but not enough for the system to become unstable.

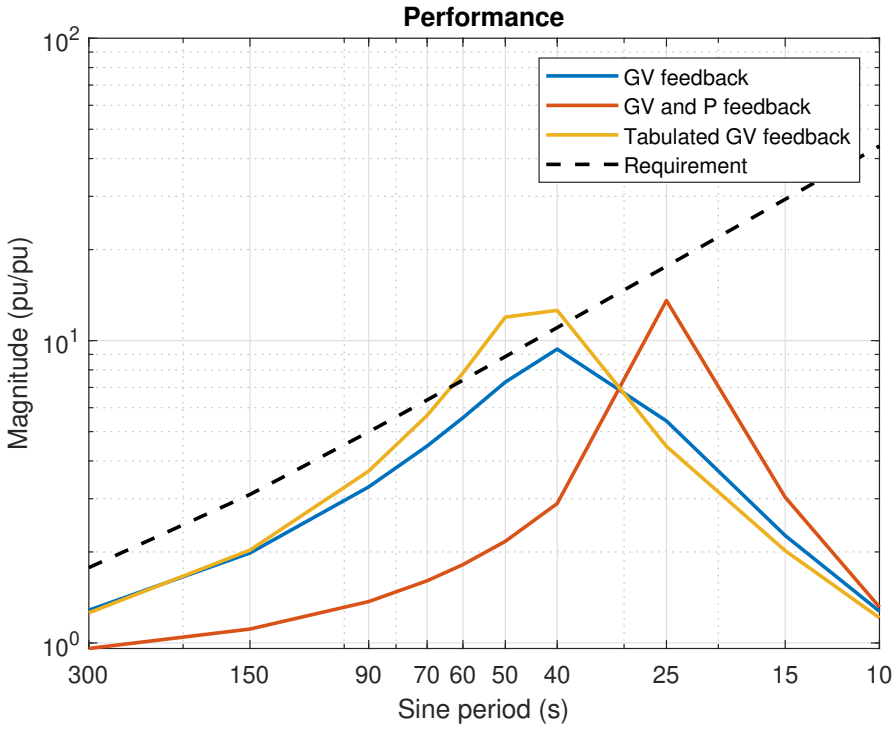

Figure 4.39: Disturbance suppression using different feedback types in the FCR-N sine tests $\left(G_c(j\omega) = \dfrac{G(j\omega)}{1 + F(j\omega)G(j\omega)} = \dfrac{\Delta\bar{f}(j\omega)}{d_P(j\omega)}\right)$.

4.4.4 Consequences for Water Flow

Four one hour simulations with a recording of actual grid frequency were performed in order to compare the variations in water flow ($\bar{Q}$ seen in Figure 3.1). The simulations were done with low droop (1.33%) and high droop (4%), and with two different combinations of controller and servo tuning. The base model with the original FCR controller parameters was compared to the most aggressive controller with fast servos, denoted T3 in section 4.4.2. Table 4.15 shows the standard deviation in water flow in per-unit during those simulations. The results show that a more aggressive controller along with faster servos slightly increases the standard deviation of water flow, but the impact of changing the droop is much larger. The standard deviation in water flow changed near proportionally to the inverse of the droop, which is expected, since active power is approximately proportional to water flow. The reason the relationship is not perfectly proportional can be traced to the nonlinear turbine characteristic and waterways model, and the dead bands and backlash of the servo models.

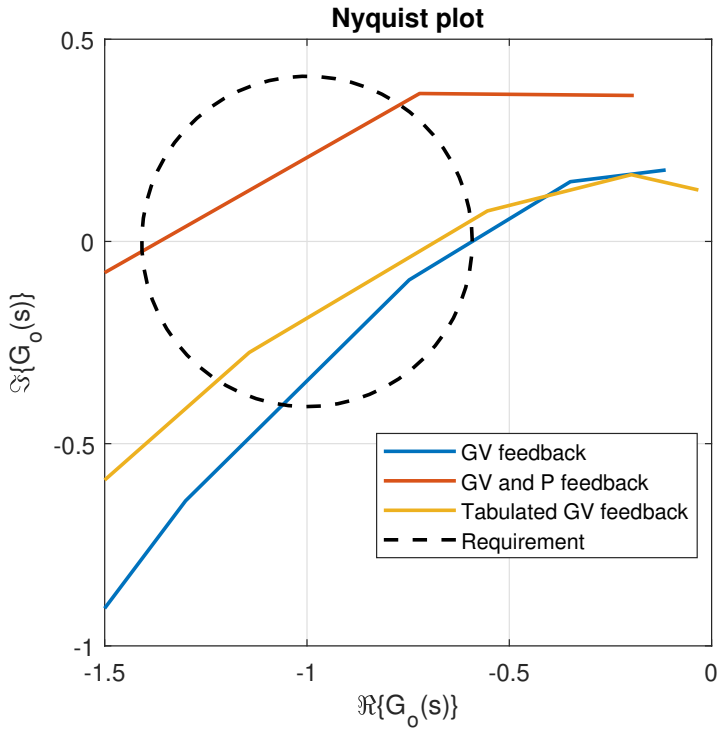

Figure 4.40: Nyquist plot using different feedback types in the FCR-N sine tests. The Nyquist curve is constructed from the open loop transfer function $\left(G_o(j\omega) = F(j\omega)G(j\omega) = \frac{\Delta\bar{f}(j\omega)}{e(j\omega)}\right)$.

Table 4.15: Standard deviation of per-unit water flow ($\bar{Q}$) during a 60 minute active control simulation, with a recording of the grid frequency as input. Base and T3 represent the model with original servos and FCR controller parameters, and the model with faster servos as well as tuned FCR controller, respectively. The parameters for the model versions can be seen in Table 4.13.

	Model version	
FCR-N droop	Base	T3
Low (1.33%)	0.0341	0.0378
High (4%)	0.0100	0.0111

5

Discussion

In this part of the thesis, the findings are discussed in relation to the research questions. The goals of the thesis are evaluated.

5.1 Model Accuracy and Simplicity

This section relates the findings to Research Question 1:

> *Can such a model, accurate enough to predict fulfillment of the technical requirements, be built using parameters obtainable before conducting actual tests?*

The base version of the model was not able to predict the measurements for prequalification with a usable level of accuracy. The model consistently predicted faster responses than the real unit, both in the time domain and in the frequency domain. The steady-state activations were not predicted with enough accuracy to make any conclusions on the fulfillment of Requirement 1. The linearity of the response, measured for Requirement 10, was not captured by the model. The real-world measurements of active power contained noise which stood for the majority of RMSE, rather than backlash and saturations. However, when the model was compensated using a first order low-pass filter, the accuracy of both time domain and frequency domain results was much improved, except for the steady-state results which were naturally not affected, and the linearity measurements. The results were close enough that it was possible to identify which requirements were the hardest to fulfill. In this case Requirement 4, related to the deactivation performance, was especially problematic.

The results were similar to those of [9], in the sense that response speed was overestimated. This makes sense, as the Kaplan turbine model used in this thesis could be considered a slightly more detailed version of the 'grey-box' model used in [9]. In both cases, the runner blade angle and guide vane position are condensed into one variable which is then used as the input to the waterways block. This limits to what extent runner blade angle can affect pressure and water flow in the modeled turbine. Similarly, the sensitivity analysis in this thesis showed that runner servo parameters had little effect on the results, further indicating that the influence of runner blade angle is not captured by the model.

However, in order to achieve the improved accuracy of the 'white-box' model in [9], more detailed measurements of water flow and pressure for different combinations

of guide vane position and runner blade angle were needed. In this thesis, the simple addition of the low-pass filter was enough to come a long way. If the same approach could be used for other units, and if the time constant T_{comp} could somehow be measured or derived from other model parameters, the model could be quite useful. Even if the time constant can not be found, the 'optimistic' base version of the model can still be used to predict failure to meet Requirements 2, 3, and 4, since it consistently responded faster than the real unit, because a failed test in the simulations is very likely to fail in real-world tests.

From the sensitivity analysis, six parameters were found to significantly impact the simulation results, seven if guide vane servo dead band and mechanical backlash are kept separate. Out of those, T_W is generally a known parameter of a hydro unit, and can be approximately calculated when the length and cross-section of the penstock is known. The dead bands and rate limits are set within the servo controllers and should therefore be known in advance, but may be subject to confidentiality. The remaining parameters, i.e. the servo time constant, input delay and mechanical backlash of the guide vanes require some type of tests to be estimated. The tests could be quite simple, and could ideally be performed through directly altering the guide vane setpoint, isolating the servo behavior from the FCR controllers. The nominal active power and nominal head are known in advance, and actual head during tests could be forecast, or tested for a few different values. The time constant T_{comp} of the first order low-pass filter was found from the sine tests in this thesis. It is not clear whether this is valid for other units, or if there are simpler methods to find it. Except for this time constant, all parameters can clearly be tied to the actual processes in the plant. The value found for T_{comp}, 1.2387 s is reasonably close to the runner servo time constant (0.8 s). Since the model otherwise failed to capture the runner blade angle's effect on performance, it could be possible that T_{comp} can be derived from the runner servo parameters.

In summary, the model cannot perform as desired without estimating some parameters from tests. If all parameters are known, the model can predict which requirements are near the limits of passing, except for Requirement 1 and 10.

5.2 Control Improvements and Fulfillment of Requirements

This section discusses the strategies used to improve performance and relates them to Research Questions 2 and 3.

> *Research Question 2: What improvements can be made to the control of the unit, in order to fulfill the technical requirements?*

Tuning the guide vane and runner servos, approximated by changing the servo time constants, was found to improve performance with regards to Requirements 2, 3, 4, 8, and 9, with unchanged FCR controller parameters, as well as allow for more aggressive FCR controllers with maintained stability margins. Based on the results from the sensitivity analysis, where runner servo parameters were not found to af-

fect the results much, the improvements were likely mostly caused by tuning the guide vane servo. Increasing the proportional gain of the FCR controllers improved disturbance suppression near the 60 s period during sine tests. The peak near the same sine period was also affected by backlash. This could imply that the effects of backlash can be at least partly compensated for by increasing the proportional gain in FCR controllers. However, the feasibility of tuning the servos and the proportional gain of FCR controllers may be limited due to increased wear and tear. Tuning the servos improved the stability margins, while tuning the FCR controllers too aggressively decreased them. Thus, for a unit with slow servos, improving the servo performance may be a more worthwhile effort than changing FCR controller parameters. Changing other parameters of the unit would be associated with replacing components rather than just altering controllers, and were therefore not considered.

The issue of incorrect steady-state activation (Requirement 1) was rectified with active power feedback. Since the feedback was slow, dynamic activation was not negatively affected. However, the stability was worsened drastically. Further damping the active power feedback for shorter periods may help the stability. The tabulated guide vane feedback approach suggested in [31] did not worsen the stability margin as much, but on the other hand did not solve the problems with steady-state activation either, because the effects of guide vane backlash and dead band were not compensated. To the author's knowledge, the implementation of combined guide vane and active power feedback in this thesis is novel, and unlike the implementations presented in [32] does not require measurement of a fictive ΔP separate for each provided FCR product.

> *Research Question 3: Are Kaplan turbines in general suitable for providing FCR?*

With all improvements investigated in this thesis, the results still indicated that Requirement 4 could not be fulfilled for the studied unit, in particular if the stability requirement (8) was to also be fulfilled. Requirement 4, unlike other performance requirements, can not be compensated with a reduction factor if the requirement is not met. Thus, failing Requirement 4 completely disqualifies a unit from participating in the FCR markets. Before conducting actual tests, the studied unit was identified as having advantageous properties for FCR provision, such as short waterways. It is likely many units with Kaplan turbines in less favorable conditions will not be able to fulfill the technical requirements. This is consistent with the findings in [12]: that Kaplan units were less suitable for FCR than Francis units, and more suitable for aFRR. However, providing aFRR may not be feasible, since the provider must be able to communicate with SvK in real time via fiber connection [44], the investment in which may be very costly [45].

5.3 Societal and Ecological Consequences

This section relates simulation results for water flow variations and the consequences of a lack of Kaplan turbines on the FCR market to Research Question 4.

Research Question 4: Are there any ecological consequences of altering FCR behavior, for example due to increased variations in water flow?

The results in section 4.4.4 showed that the variations in water flow were close to inversely proportional to droop, while more aggressive controllers only marginally affected the results. Further, short term variation caused by FCR operation are unlikely to meaningfully affect water levels, compared to longer term variations caused by changing the production setpoint on an hourly basis for electricity wholesale. The mean of water flow changes caused by FCR-N will be close to zero since FCR-N is activated symmetrically.

As mentioned in section 2.5.1, Kaplan turbines are suitable for hydro power plants with low hydraulic head, such as in run-of-the-river power plants. The ecological impacts of this type of hydro power plant is lower than of those with large dams and reservoirs because the water flow is closer to the natural flow of the river and their dams cause less flooding of the area upstream of the plant [46], [47]. Coupled with the results from this thesis, this indicates that FCR operation in Kaplan turbines does not cause significant ecological consequences.

Are there any consequences for the adoption of renewable energy sources if many hydro units equipped with Kaplan turbines can not provide FCR?

Earlier, it has been said that the adoption of variable renewable electricity production has led to an increase in FCR demand [2]. The results in this thesis indicate that Kaplan units will struggle to prequalify for FCR-D provision. However, SvK only predicts an increased demand for FCR-D upwards capacity of 150 MW between 2024 and 2026 [48]. Meanwhile, prequalified FCR-D upwards capacity from energy storage systems (such as batteries) has increased from 80 MW to 530 MW between January and October 2024 alone [19]. FCR-D downwards has also seen increased prequalified capacity from energy storage and wind power during 2024 [49]. In [17] and [18] the authors saw technical and economic potential for FCR provision from other sources than hydropower, but FCR provision from batteries was calculated to not be profitable. Since then, it seems market actors have deemed the technology profitable since it is as of October 2024 one of the fastest growing sources of FCR. Thus, a lack of FCR provision from Kaplan turbines does not currently seem to be a major obstacle for continued integration of renewable electricity production.

5.4 Discussion on Methodology

Especially for the sensitivity analysis, it was important to be able to numerically represent how the unit's performance related to the requirements. For Requirement 9, related to disturbance suppression in the frequency domain, the requirement was evaluated at the sine period closest to failing, or failing the most. This did not always provide enough information, as seen in section 4.4.1. Several parameters affected performance at the 60 s period, which might have been more interesting to study. However, when there was a peak large enough to be close to the requirement, the margin between the peak and the requirement was captured as intended.

The estimation of servo parameters was uncertain, especially with regard to dividing

total backlash between dead bands and mechanical backlash, was not as systematic as one would like. The use of system identification was attempted, but did not produce satisfactory results for linear components and could not be used for backlash estimation. However, since dead bands and mechanical backlash were seen to affect the results in very similar ways, their sum was more important.

One flaw of the model is that the gross hydraulic head is fixed during simulations, so loss of hydraulic head from sustained increased flow can not be modeled. Still, if it were to be modeled, this would require even more information about the plant, which would conflict with the objective of having a simple model.

5.5 Future Work

The first order low-pass filter used for compensating an unexplained delay in this thesis was simple, but markedly improved model accuracy. Future studies could investigate if the same approximation can be used for other Kaplan units or even other types of turbines, and if so, if the time constant can be derived from other model parameters, for example in the runner servo in the case of Kaplan turbines. Only then would it be possible to perform accurate simulations ahead of actual tests.

The combined guide vane and active power feedback used in this thesis showed some potential, but was detrimental to stability. Further investigation into how it can be implemented could be useful for all kinds of hydro power plants facing difficulties with Requirement 1, not just Kaplan units.

While Kaplan turbines may be too slow for the dynamic requirements for FCR, energy storage systems such as batteries can respond very quickly to frequency deviations. However, there is an investment cost associated with batteries, and the endurance is limited. Kaplan turbines have wide operating ranges with high efficiency. A combination of both technologies could play to their respective strengths. In this way, the economic benefit of a battery could be greater when used to augment an Kaplan or other hydro turbine, compared to when used as a standalone FCR providing unit. Further studies into this subject would be very interesting.

6

Conclusion

The main goal of this thesis was to develop a model of a Kaplan turbine, suitable for simulation of FCR prequalification and prediction of passing or failing the technical requirements for FCR, with parameters that could be known before conducting real tests. In addition, the study set out to assess how the parameters of the proposed model affect prequalification results, and investigate how the FCR controller can be tuned in order to better fulfill the technical requirements. Finally, the thesis explored ecological effects of more aggressive tuning of FCR controllers in Kaplan turbines, and consequences of Kaplan turbines being excluded from the FCR markets.

The study found that the initially proposed model performed qualitatively similar to the real unit used as a reference, but was not accurate enough to predict fulfillment of the technical requirements. The results indicated that the model did not fully capture the effect of runner blade angle on the dynamic performance. The exception to this was the runner blade rate limit, which caused the runner blades to deviate far enough from the combination curve that the effect was noticeable. Further investigation found that the discrepancy in model and real-world performance in this specific case could be approximated with a first order low-pass filter, which could be compensating for the failure to model runner dynamics, but this will most likely be unit dependent, and not possible to know before conducting real-world tests. Results from simulations showed that the model with the added low-pass filter performed much closer to the real-world unit. With the exception of said filter, the study found that the model can achieve this accuracy with parameters closely tied to real physical processes or controller settings of the servos in the unit. However, several servo parameters require some sort of tests to be performed for estimation, so the goal of being able to perform simulations without any real-world tests was not met.

The investigation into FCR controller tuning showed that the proportional gain of this unit's controller could be increased from the original value 0.25 to 0.35 without decreasing the stability margin, which improved dynamic performance. Another finding was that tuning the guide vane and runner servos also significantly improved the performance as well as the stability margins, and thus allowed for more proportional and integral gain in the FCR controller. The effects of changing the FCR controller gains found in this study should be applicable to other units, but the exact changes that can be made are of course unit dependent. The consequences of tuning the FCR controllers for wear and tear was not examined in detail, but it should be noted that larger control action in general is associated with increased

wear and tear. Since tuning was not optimized with wear and tear in mind, this study cannot conclusively state what the optimal controller gains would be.

The thesis introduced a new approach for combining guide vane feedback and active power feedback, which was found to improve compliance with requirements on steady-state performance, without negatively affecting dynamic performance. However, it was also found that this approach would worsen the stability in a closed-loop system.

The results from this thesis indicate that many Kaplan turbines may not respond quickly enough to be eligible for FCR-D, any direction. However, increased FCR market participation from other sources of FCR suggests that this is unlikely to cause problems on a system level. This study did not find more aggressive FCR controllers to have meaningful impact on water flow variation, and therefore little to no ecological consequences.

The conclusions that can be drawn on the basis of this study are limited by the fact that the model was only validated against one real-world Kaplan turbine. In particular, it is not known whether the low-pass filter used for compensating the model is valid for other units, and its parameters can not conclusively be said to depend on any known physical parameter. While the scope of the thesis was limited to FCR prequalification, due to the extensive tests associated with prequalification, the results can still show some insight into the general dynamic behavior of Kaplan turbines.

Bibliography

[1] ENTSO-E, *Technical requirements for frequency containment reserve provision in the nordic synchronous area*, Brussels, Belgium, May 26, 2023. [Online]. Available: https://www.svk.se/siteassets/aktorsportalen/bidra-med-reserver/om-olika-reserver/fcr/fcr-technical-requirements-may-23.pdf (visited on 2024-04-09).

[2] L. Saarinen, "The frequency of the frequency : On hydropower and grid frequency control," Publisher: Acta Universitatis Upsaliensis, Ph.D. dissertation, Uppsala University, 2017. [Online]. Available: https://urn.kb.se/resolve?urn=urn:nbn:se:uu:diva-308441 (visited on 2024-04-09).

[3] J. Jiang, "Design of an optimal robust governor for hydraulic turbine generating units," *IEEE Transactions on Energy Conversion*, vol. 10, no. 1, pp. 188–194, Mar. 1995, ISSN: 08858969. DOI: 10.1109/60.372586. [Online]. Available: http://ieeexplore.ieee.org/document/372586/ (visited on 2024-04-17).

[4] L. Saarinen, P. Norrlund, and U. Lundin, "Tuning primary frequency controllers using robust control theory in a power system dominated by hydropower," in *Proceedings of the CIGRÉ Session*, Paris, Jul. 2016.

[5] L. Saarinen, P. Norrlund, and U. Lundin, "Field measurements and system identification of three frequency controlling hydropower plants," *IEEE Transactions on Energy Conversion*, vol. 30, no. 3, pp. 1061–1068, Sep. 2015, ISSN: 0885-8969, 1558-0059. DOI: 10.1109/TEC.2015.2425915. [Online]. Available: http://ieeexplore.ieee.org/document/7110341/ (visited on 2024-04-09).

[6] M. Brezovec, I. Kuzle, and T. Tomisa, "Nonlinear digital simulation model of hydroelectric power unit with kaplan turbine," *IEEE Transactions on Energy Conversion*, vol. 21, no. 1, pp. 235–241, Mar. 2006, ISSN: 0885-8969. DOI: 10.1109/TEC.2005.847963. [Online]. Available: http://ieeexplore.ieee.org/document/1597342/ (visited on 2024-04-16).

[7] IEEE Committees, "Dynamic models for turbine-governors in power system studies," IEEE Power & Energy Society, Tech. Rep. PES-TR1, Jan. 2013.

[8] D. Kosterev, "Hydro turbine-governor model validation in pacific northwest," *IEEE Transactions on Power Systems*, vol. 19, no. 2, pp. 1144–1149, May 2004, ISSN: 0885-8950. DOI: 10.1109/TPWRS.2003.821464. [Online]. Available: http://ieeexplore.ieee.org/document/1295026/ (visited on 2024-05-14).

[9] E. Dahlborg, P. Norrlund, and L. Saarinen, "Kaplan turbine model validation for large grid frequency disturbances," *IEEE Transactions on Energy Conversion*, vol. 36, no. 2, pp. 611–618, Jun. 2021, ISSN: 0885-8969, 1558-0059. DOI: 10.1109/TEC.2020.3029636. [Online]. Available: https://ieeexplore.ieee.org/document/9218972/ (visited on 2024-04-09).

[10] M. Gratza, R. Witzmann, C. J. Steinhart, *et al.*, "Frequency stability in island networks: Development of kaplan turbine model and control of dynamics," in *2018 Power Systems Computation Conference (PSCC)*, Dublin: IEEE, Jun. 2018, pp. 1–7, ISBN: 978-1-910963-10-4. DOI: 10.23919/PSCC.2018.8442445. [Online]. Available: https://ieeexplore.ieee.org/document/8442445/ (visited on 2024-04-16).

[11] M. Gustafsson, "Improved governing of kaplan turbine hydropower plants operating island grids," M.S. thesis, KTH Royal Institute of Technology, Stockholm, Sweden, 2013.

[12] L. Saarinen, P. Norrlund, W. Yang, and U. Lundin, "Allocation of frequency control reserves and its impact on wear and tear on a hydropower fleet," *IEEE Transactions on Power Systems*, vol. 33, no. 1, pp. 430–439, Jan. 2018, ISSN: 0885-8950, 1558-0679. DOI: 10.1109/TPWRS.2017.2702280. [Online]. Available: http://ieeexplore.ieee.org/document/7921697/ (visited on 2024-04-09).

[13] E. Agneholm and E. A. Jansson, "FCP project summary report," ENTSO-E, Brussels, Belgium, May 11, 2017.

[14] R. Eriksson, N. Modig, and A. Westberg, "FCR-n design of requirements," ENTSO-E, Brussels, Belgium, Jul. 4, 2017.

[15] M. Kuivaniemi, N. Modig, and R. Eriksson, "FCR-d design of requirements," ENTSO-E, Brussels, Belgium, Jul. 5, 2017.

[16] E. Agneholm, S. Afkhami Meybodi, M. Kuivaniemi, *et al.*, "FCR-d design of requirements - phase 2," ENTSO-E, Brussels, Belgium, Jan. 13, 2019.

[17] S. Appelstål, "Technical evaluation of existing and potential technologies for automatic frequency control in the Swedish power system," M.S. thesis, Uppsala University, Uppsala, Sweden, 2019. (visited on 2024-09-23).

[18] A. Lindgren, "Economic mapping of technologies that potentially could deliver the reserves FCR and aFRR," M.S. thesis, Uppsala University, Uppsala, Sweden, 2019.

[19] "Utbud på marknaderna för reserver." (Jul. 1, 2024), [Online]. Available: https://www.svk.se/aktorsportalen/bidra-med-reserver/behov-av-reserver-nu-och-i-framtiden/utbud-pa-marknaderna-for-reserver/ (visited on 2024-10-21).

[20] Svenska Kraftnät, "Kraftbalansen på den svenska elmarknaden, rapport 2024," Sundbyberg, 2024/1927, May 31, 2024, p. 17. [Online]. Available: https://www.svk.se/siteassets/om-oss/rapporter/2024/kraftbalansen-pa-den-svenska-elmarknaden-rapport-2024.pdf (visited on 2024-10-31).

[21] P. Kundur, J. Paserba, V. Ajjarapu, *et al.*, "Definition and classification of power system stability IEEE/CIGRE joint task force on stability terms and definitions," *IEEE Transactions on Power Systems*, vol. 19, no. 3, pp. 1387–1401, Aug. 2004, ISSN: 0885-8950. DOI: 10.1109/TPWRS.2004.825981. [Online]. Available: http://ieeexplore.ieee.org/document/1318675/ (visited on 2024-06-24).

[22] P. Kundur, *Power system stability and control*, 1st ed. New York: McGraw-Hill, 1994, 1176 pp., ISBN: 978-0-07-035958-1.

[23] Nordic Energy Regulators. "An overview of the nordic electricity market," NordREG. (Jan. 10, 2019), [Online]. Available: https://www.nordicenergyregulators.org/about-nordreg/an-overview-of-the-nordic-electricity-market/ (visited on 2024-09-12).

[24] "Om olika reserver," Svenska kraftnät. (Apr. 30, 2024), [Online]. Available: https://www.svk.se/aktorsportalen/bidra-med-reserver/om-olika-reserver/ (visited on 2024-09-12).

[25] "Frekvenshållningsreserv normaldrift (FCR-N)," Svenska kraftnät. (Apr. 30, 2024), [Online]. Available: https://www.svk.se/aktorsportalen/bidra-med-reserver/om-olika-reserver/fcr-n/ (visited on 2024-09-12).

[26] "Frekvenshållningsreserv störning uppreglering (FCR-D upp)," Svenska kraftnät. (Apr. 30, 2024), [Online]. Available: https://www.svk.se/aktorsportalen/bidra-med-reserver/om-olika-reserver/fcr-d-upp/ (visited on 2024-09-12).

[27] "Frekvenshållningsreserv störning nedreglering (FCR-D ned)," Svenska kraftnät. (Apr. 30, 2024), [Online]. Available: https://www.svk.se/aktorsportalen/bidra-med-reserver/om-olika-reserver/fcr-d-ned/ (visited on 2024-09-12).

[28] M. Persson, "Frequency response by wind farms in power systems with high wind power penetration," Ph.D. dissertation, Chalmers University of Technol-

ogy, Gothenburg, Sweden, 2017, 164 pp. [Online]. Available: https://research.chalmers.se/publication/250313.

[29] European Commission, "COMMISSION REGULATION (EU) 2016/ 631 - of 14 april 2016 - establishing a network code on requirements for grid connection of generators," *Official Journal of the European Union*, vol. 59, pp. 1–68, L 112 Apr. 27, 2016, ISSN: 1977-0677. [Online]. Available: http://data.europa.eu/eli/reg/2016/631/oj (visited on 2024-08-06).

[30] "Snabb frekvensreserv (FFR)," Svenska kraftnät. (May 9, 2023), [Online]. Available: https://www.svk.se/aktorsportalen/bidra-med-reserver/om-olika-reserver/ffr/ (visited on 2024-09-23).

[31] L. Saarinen, *Implementation and tuning guideline for FCR provision*, May 29, 2023. [Online]. Available: https://www.svk.se/siteassets/aktorsportalen/bidra-med-reserver/om-olika-reserver/fcr/implementation-and-tuning-guideline-for-fcr-provision-may-23.pdf (visited on 2024-07-29).

[32] Svenska Kraftnät, "Effekt- och pådragsåterkoppling för en synkron kraftproduktionsmodul," Svenska Kraftnät, SvK 2023/2892, Feb. 17, 2023. [Online]. Available: https://www.svk.se/siteassets/1.om-kraftsystemet/legalt-ramverk/eu-lagstiftning/anslutningskoder/effekt--och-padragsaterkoppling-for-en-synkron-kraftproduktionsmodul.pdf (visited on 2024-08-06).

[33] Tennessee Valley Authority; SVG version by Tomia, *Schematic diagram of hydroelectric power plant*, https://creativecommons.org/licenses/by-sa/3.0/legalcode, Aug. 18, 2000. [Online]. Available: https://commons.wikimedia.org/wiki/File:Hydroelectric_dam.svg.

[34] M. Polák, "A brief history of the kaplan turbine invention," *Energies*, vol. 14, no. 19, Sep. 29, 2021, ISSN: 1996-1073. DOI: 10.3390/en14196211. [Online]. Available: https://www.mdpi.com/1996-1073/14/19/6211 (visited on 2024-08-06).

[35] H. G. Hansson, "Development of the kaplan turbine," in *Dædalus: Tekniska museets årsbok*, vol. 47, Stockholm, Sweden: Tekniska Museet, 1977, pp. 11–35. [Online]. Available: https://www.digitalamodeller.se/arsbocker/daedalus-1977/ (visited on 2024-08-06).

[36] Jahobr, *Sketch of a kaplan turbine*, CC0, Nov. 23, 2016. [Online]. Available: https://commons.wikimedia.org/wiki/File:KaplanSketch.svg (visited on 2024-08-07).

[37] Jahobr, *Sketch of a francis turbine*, CC0, Nov. 23, 2016. [Online]. Available: https://commons.wikimedia.org/wiki/File:FrancisSketch.svg (visited on 2024-08-07).

[38] "Power plants: Lilla edet," Vattenfall. (Aug. 7, 2024), [Online]. Available: https://powerplants.vattenfall.com/lilla-edet/ (visited on 2024-08-07).

[39] T. J. Santner, B. J. Williams, and W. I. Notz, "Sensitivity analysis and variable screening," in *The Design and Analysis of Computer Experiments*, T. J. Santner, B. J. Williams, and W. I. Notz, Eds., New York, NY: Springer, 2018, pp. 247–297, ISBN: 978-1-4939-8847-1. DOI: 10.1007/978-1-4939-8847-1_7. [Online]. Available: https://doi.org/10.1007/978-1-4939-8847-1_7 (visited on 2024-09-30).

[40] The MathWorks Inc., *Simulink version: 23.2 (r2023b)*, Natick, Massachusetts, United States, 2023. [Online]. Available: https://www.mathworks.com.

[41] The MathWorks Inc., *MATLAB version: 23.2.0 (r2023b)*, Natick, Massachusetts, United States, 2023. [Online]. Available: https://www.mathworks.com.

[42] M. Gratza, *AW: Your paper on kaplan turbine modeling*, E-mail, Apr. 30, 2024.

[43] The MathWorks Inc., *System identification toolbox version: 23.2 (r2023b)*, Natick, Massachusetts, United States, 2023. [Online]. Available: https://www.mathworks.com.

[44] "Bidra med FCR, aFRR eller mFRR," Svenska kraftnät. (Apr. 30, 2024), [Online]. Available: https://www.svk.se/aktorsportalen/bidra-med-reserver/bli-leverantor-av-reserver/bidra-med-fcr-afrr-eller-mfrr/ (visited on 2024-10-21).

[45] "Om realtidsdata," Svenska kraftnät. (Oct. 11, 2023), [Online]. Available: https://www.svk.se/utveckling-av-kraftsystemet/systemansvar--elmarknad/kraftsystemhubben/om-realtidsdata/ (visited on 2024-10-21).

[46] J. Donev. "Hydroelectric reservoir." (2024), [Online]. Available: https://energyeducation.ca/encyclopedia/Hydroelectric_reservoir (visited on 2024-09-23).

[47] J. Donev. "Run-of-the-river hydroelectricity." (2024), [Online]. Available: https://energyeducation.ca/encyclopedia/Run-of-the-river_hydroelectricity (visited on 2024-09-23).

[48] "Framtida volymbehov," Svenska kraftnät. (Jul. 1, 2024), [Online]. Available: https://www.svk.se/aktorsportalen/bidra-med-reserver/behov-av-reserver-nu-och-i-framtiden/framtida-volymbehov/ (visited on 2024-10-21).

[49] "Allt fler leverantörer av stödtjänster för det svenska elsystemet," Svenska kraftnät. (Sep. 26, 2024), [Online]. Available: https://www.svk.se/press-och-nyheter/nyheter/balansansvar/2024/allt-fler-leverantorer-av-stodtjanster-for-det-svenska-elsystemet/ (visited on 2024-10-21).

[50] Gustaver, M. (2020) A Chalmers University of Technology Master's thesis template for LaTeX. Unpublished.

A

FCR Technical Requirements and Prequalification

Here, the tests and requirements relevant for FCR prequalification of a hydro power plant are presented.

A.1 Step and Ramp Responses

These prequalification tests are used for determining steady state responses as well as time domain performance. The step and ramp tests are performed with different combinations of loading conditions and droop according to Table 2.1. The FCR provider must show that the unit qualifies in the range of values to be used during operation. The most challenging combination from a loading standpoint, usually high load with low droop, is used for endurance testing.

FCR-N

These tests evaluate the steady state power levels and the speed of the response. For FCR-N, the simulated frequency shown in Figure A.1 is injected. In the figure, an idealized active power response is also shown. The first downward pulse is meant to put units with backlash in the least advantageous position ahead of the first large step. The steady state power is measured right before every large step, as well as in the end of the test (at around 400, 700, 1000 and 1300 seconds) and denoted $P_{\text{ss},0}$, $P_{\text{ss},1}$, $P_{\text{ss},2}$ and $P_{\text{ss},3}$ respectively. For endurance testing, the same sequence is used with longer duration between steps.

The mean of $P_{\text{ss},0}$ and $P_{\text{ss},3}$ is used to signify baseline power with no FCR-N activation. Then, steady state activation can be calculated for the upwards and downwards direction, respectively:

$$\Delta P_{\text{ss},1} = P_{\text{ss},1} - \frac{1}{2}(P_{\text{ss},0} + P_{\text{ss},3}) \tag{A.1}$$

$$\Delta P_{\text{ss},2} = P_{\text{ss},2} - \frac{1}{2}(P_{\text{ss},0} + P_{\text{ss},3}) \tag{A.2}$$

Requirement 1 for FCR-N allows for 5% of under-delivery and 20% of over-delivery compared to the theoretical capacity. Theoretical capacity can be calculated by

multiplying the frequency deviation with the chosen regulating strength, or using another method specified by the FCR candidate, e.g. if the relationship between controller output and active power is not linear. Thus, Requirement 1 for FCR-N is formulated as

$$-0.05 \leq \frac{\Delta P_{\text{ss},1} - |\Delta P_{\text{ss,theoretical}}|}{|P_{\text{ss,theoretical}}|} \leq 0.2 \tag{A.3}$$

in the upwards direction and

$$-0.2 \leq \frac{\Delta P_{\text{ss},2} + |\Delta P_{\text{ss,theoretical}}|}{|P_{\text{ss,theoretical}}|} \leq 0.05 \tag{A.4}$$

in the downwards direction.

In case the requirement is not met, a reduction factor $K_{\text{red,ss}} \in [0.9, 1]$ is allowed to be applied to the theoretical capacity.

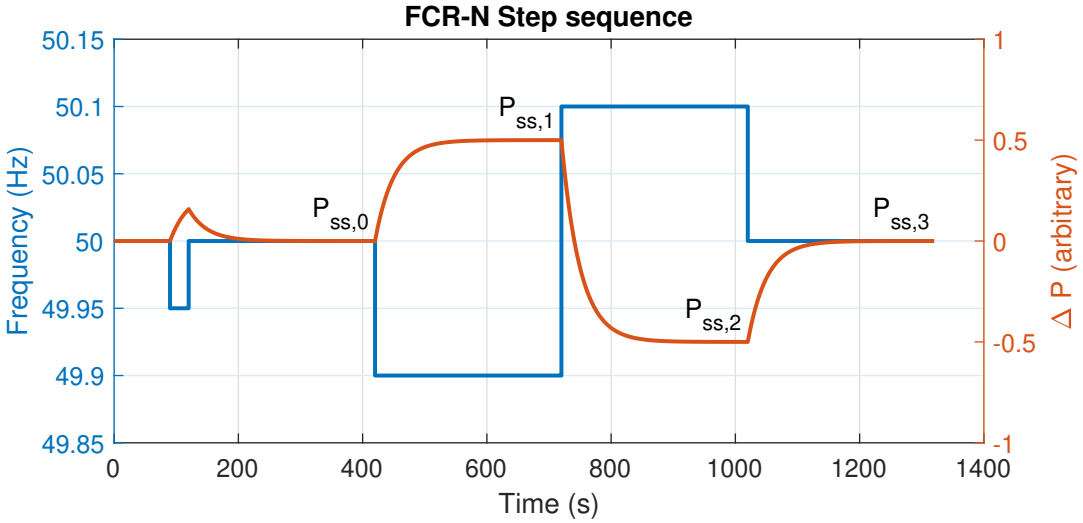

Figure A.1: Simulated frequency input for FCR-N step test.

FCR-D

The ramp sequence for FCR-D is more complex than the sequence used for FCR-N. Several aspects of performance are tested during different parts of the sequence. Different versions of the sequence are used for the different combinations in Table 2.1, with endurance variants and added steps for testing the combination of FCR-D and FCR-N. Since FCR-D is not symmetrical, the upwards and downwards directions are tested separately. For illustration, Figure A.2 shows the sequence used for FCR-D upwards with concurrent FCR-N activation. Not all combinations are tested with FCR-N active, only tests with high droop are performed with FCR-N enabled. The different ramps and measurements taken are explained in the following parts. For brevity only FCR-D upwards is described in detail, but the same principles are true in reverse for FCR-D downwards.

Besides quantifying the performance, the ramp sequence is also designed to confirm the function of the unit's mode shifting. The FCR unit may use parameters that

do not fulfill the stability requirements for 10 s following disturbances of 0.2 Hz or greater in its high performance mode. During a cooldown period after the activation of high performance mode, the unit must remain in high stability mode for 5 min (300 s) or up to 15 min (900 s).

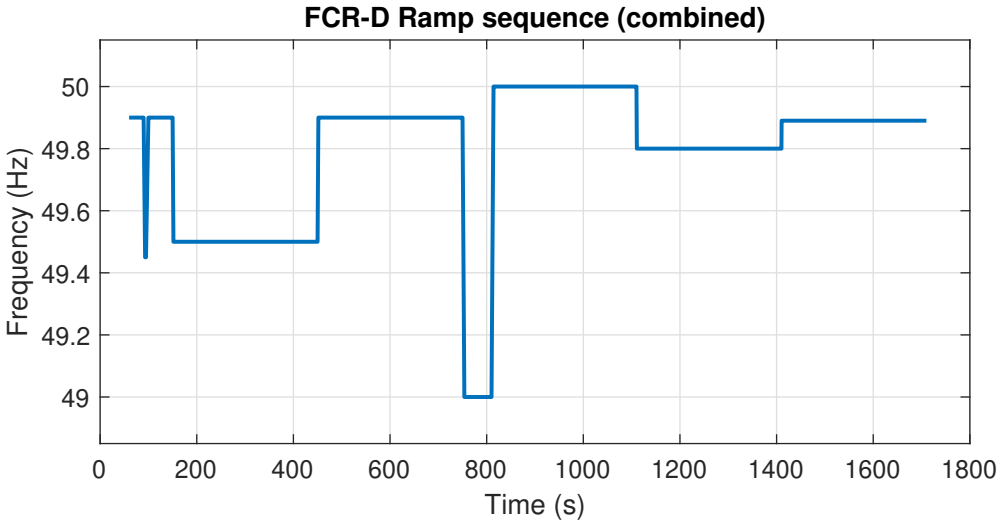

Figure A.2: Simulated frequency input for FCR-D upwards ramp test, with FCR-N active.

The first part of the sequence is called the deactivation test, seen in Figure A.3. The injected frequency is an approximation of the grid's response to a disturbance half the size of the reference incident (1450 MW) [16]. After a disturbance, an overshoot in the opposite direction is possible but undesirable. In order to limit the overshoot, the energy injected to the grid after the frequency nadir should be limited. If the FCR unit uses mode shifting, the high performance mode should be activated once the injected frequency deviation exceeds 0.2 Hz and deactivated within 10 s.

The overshoot energy is calculated by integrating the activated power that exceeds $0.5\Delta P_{\text{ss,theoretical}}$ or ΔP_{nadir}, whichever leads to a greater result, with respect to time. If the activated power does not decrease below $0.5\Delta P_{\text{ss,theoretical}}$ or ΔP_{nadir} within 40 s, the integration is cut off. For the upwards direction, it is formulated as:

$$E_{\text{overshoot}} = \max_{k=t_{\text{nadir}} \to t_{\text{nadir}}+40} \int_{t_{\text{nadir}}}^{t=k} \left(\Delta P(t) - \min\left(|\Delta P_{\text{nadir}}|, 0.5 \cdot |\Delta P_{\text{ss,theoretical}}|\right)\right) dt. \tag{A.5}$$

For the downwards direction, the overshoot energy is calculated the same except the sign of ΔP is flipped. Requirement 4 for FCR-D states that the overshoot energy must not exceed the theoretical capacity integrated over 1.7 s, or:

$$E_{\text{overshoot}} \leq |\Delta P_{\text{ss,theoretical}}| \cdot 1.7\,\text{s}. \tag{A.6}$$

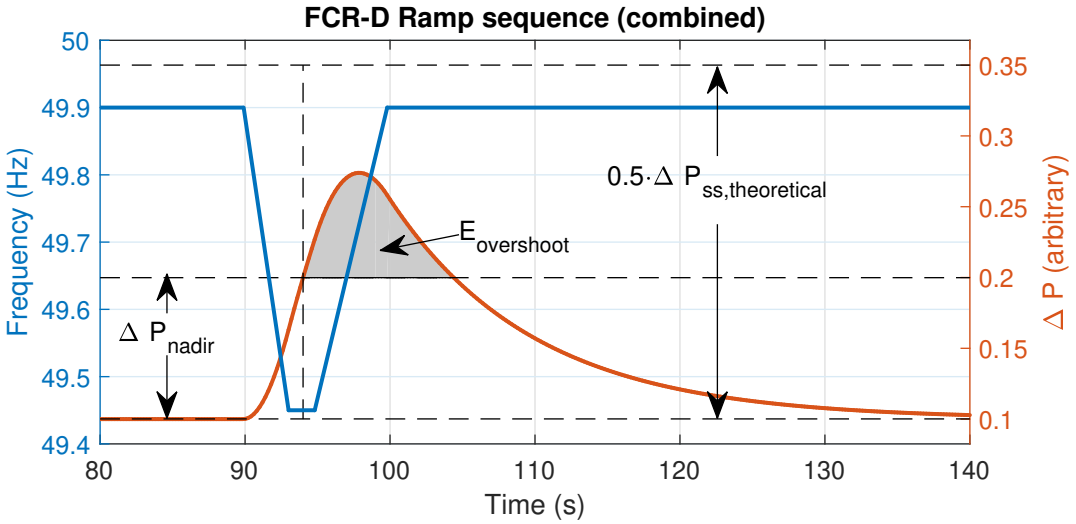

Figure A.3: Simulated frequency input for upward FCR-D deactivation test.

The next part of the ramp sequence can be seen in Figure A.4. During the ramp following the deactivation test, at around 150 s in the figure, there are no requirements on performance. The ramp serves to confirm that the high performance mode is blocked after the deactivation test, as well as to bring the unit to full FCR-D activation (49.5 Hz). Before the next ramp, the steady state power is recorded ($P_{\text{ss},3}$). After the ramp at 450 s, FCR-D activation should approach zero (49.9 Hz). Again, steady state power is recorded ($P_{\text{ss},4}$). The difference between $P_{\text{ss},3}$ and $P_{\text{ss},4}$ should then be the same as the FCR-D capacity.

$$\Delta P_{\text{ss}} = P_{\text{ss},3} - P_{\text{ss},4} \tag{A.7}$$

Thus, Requirement 1 for FCR-D can be formulated, similarly as for FCR-N:

$$-0.05 \leq \frac{\Delta P_{\text{ss}} - |\Delta P_{\text{ss,theoretical}}|}{|\Delta P_{\text{ss,theoretical}}|} \leq 0.2 \tag{A.8}$$

in the upwards direction and

$$-0.2 \leq \frac{\Delta P_{\text{ss}} + |\Delta P_{\text{ss,theoretical}}|}{|\Delta P_{\text{ss,theoretical}}|} \leq 0.05 \tag{A.9}$$

in the downwards direction.

Similarly to FCR-N, a steady state reduction factor $K_{\text{red,ss}} \in [0.75, 1]$ is allowed. Note that the reduction factor for FCR-D may be lower than for FCR-N.

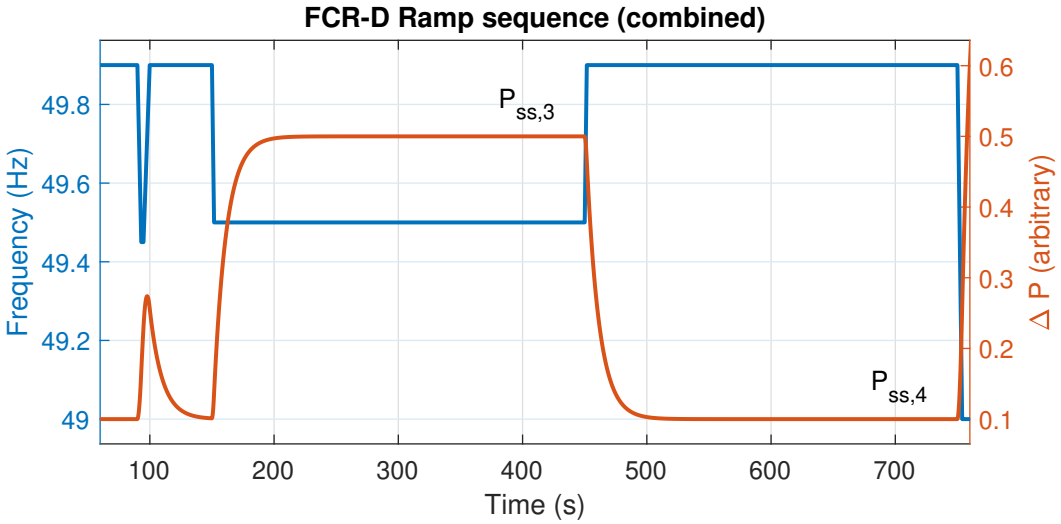

Figure A.4: Simulated frequency input for upward FCR-D steady state response test.

Following the steady state test, the high performance mode should be available again. The next ramp tests the dynamic performance of the FCR unit, and is illustrated in Figure A.5. This ramp lowers the simulated frequency to 49 Hz, and units with LFSM controllers must have them enabled. Thus both FCR-D and LFSM contributes to the response. The requirements for this test are fairly straightforward. If it is used, the high performance mode should be activated. The change in power after 7.5 s should be at least 86% of the theoretical capacity, and the energy contribution after the same amount of time should be equivalent to full theoretical capacity integrated over 3.2 s.

This gives Requirement 2:

$$|\Delta P_{7.5\mathrm{s}}| \geq 0.86 |\Delta P_{\mathrm{ss,theoretical}}| \tag{A.10}$$

and Requirement 3:

$$|E_{7.5\mathrm{s}}| = \left| \int_{t_{\mathrm{start}}}^{t_{\mathrm{start}}+7.5\,\mathrm{s}} \Delta P(t) dt \right| \geq |\Delta P_{\mathrm{ss,theoretical}}| \cdot 3.2\,\mathrm{s}. \tag{A.11}$$

If the requirements are not met, a dynamic reduction factor $K_{\mathrm{red,dyn}} \in [0.75, 1]$ may be applied to the theoretical capacity.

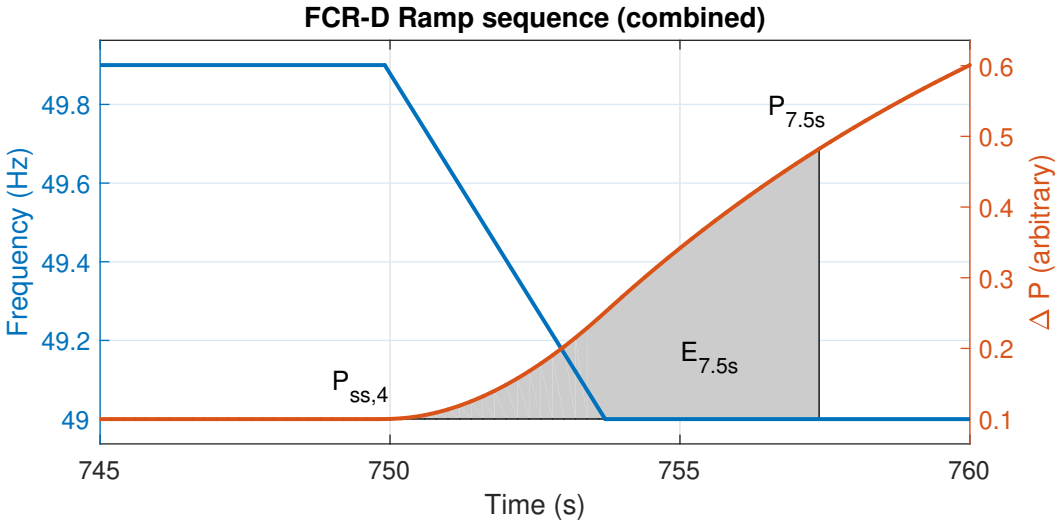

Figure A.5: Simulated frequency input for upward FCR-D fast ramp test.

The final test of the ramp sequence measures the steady state response with FCR-N and FCR-D combined. As seen in Figure A.6, ideally zero activation at 50 Hz ($P_{\mathrm{ss},6}$) is compared with full FCR-N activation and a small FCR-D activation at 49.89 Hz ($P_{\mathrm{ss},8}$). Like all other steady state measurements, this is also called Requirement 1 and is formulated as such:

$$-0.05 \leq \frac{P_{\mathrm{ss},8} - P_{\mathrm{ss},6} - |\Delta P_{\mathrm{ss,theo,FCR-N}}| - 0.01/0.4|\Delta P_{\mathrm{ss,theo,FCR-D}}|}{|\Delta P_{\mathrm{ss,theo,FCR-N}}|} \leq 0.2 \quad \text{(A.12)}$$

for FCR-D upwards and

$$-0.2 \leq \frac{P_{\mathrm{ss},8} - P_{\mathrm{ss},6} + |\Delta P_{\mathrm{ss,theo,FCR-N}}| + 0.01/0.4|\Delta P_{\mathrm{ss,theo,FCR-D}}|}{|\Delta P_{\mathrm{ss,theo,FCR-N}}|} \leq 0.05 \quad \text{(A.13)}$$

for FCR-D downwards. Note that since FCR-D up and down are separate products, the theoretical capacity $P_{\mathrm{ss,theo,FCR-D}}$ may be different depending on direction. All theoretical capacities are calculated using the FCR candidate's method of choice.

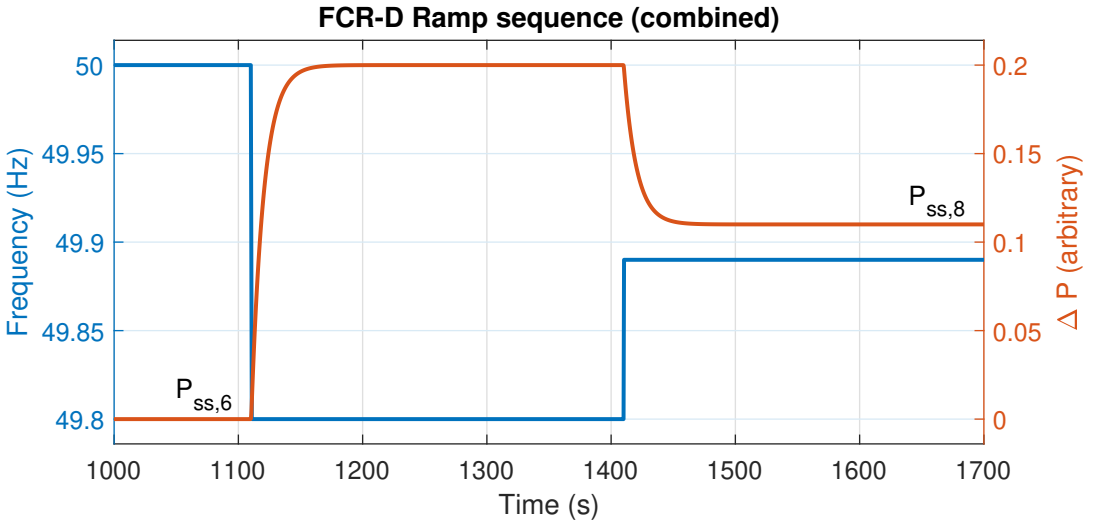

Figure A.6: Simulated frequency input for combined FCR-N and FCR-D steady state response test.

A.2 Sine Responses

In order to test the frequency domain stability and performance requirements, a set of tests includes a sinusoidally varying frequency signal, such as in Figure A.7. A sinusoid is fitted to the output power. From the amplitude and phase shift from the frequency, an approximated transfer function $F(j\omega)$ is obtained. The transfer function is normalized against the theoretical capacity. An example of what $F(j\omega)$ may look like is seen in Figure A.8

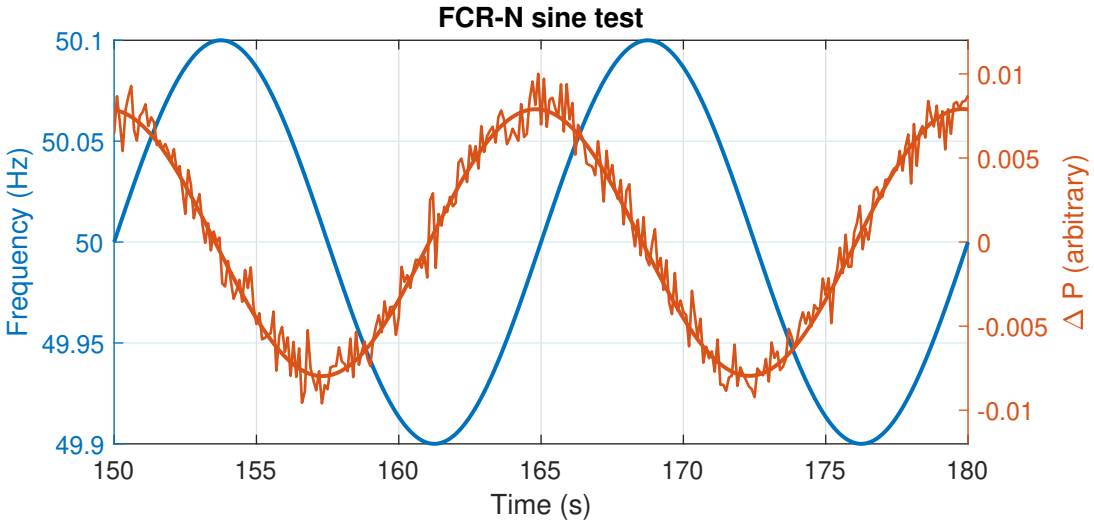

Figure A.7: Simulated frequency input for FCR-N sine test for the 15 s period.

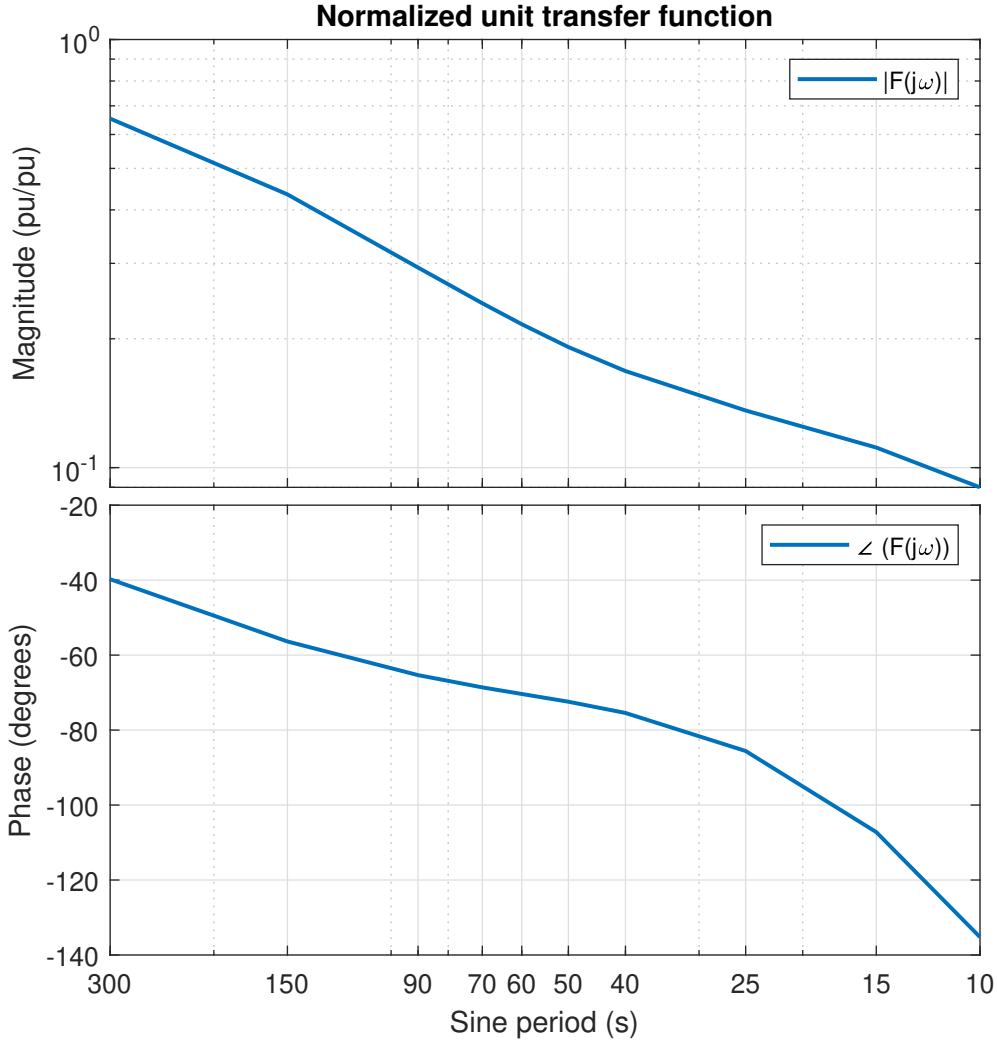

Figure A.8: Normalized transfer function of the unit, $F(j\omega) = \dfrac{\Delta\bar{P}(j\omega)}{e(j\omega)}$.

The sine tests are performed with frequency input sines with period times of 300, 150, 90, 70, 60, 50, 40, 25, 15, and 10 seconds. The frequency signal has an amplitude of 0.1 Hz and is centered around 50.0 Hz for FCR-N, 49.7 Hz for upward FCR-D and 50.3 Hz for downward FCR-D. If the upward and downward FCR-D controllers share the same parameters, the tests only need to be performed for one of the products. Further, if the high stability mode of the tested FCR-D controller has the same parameters as the FCR-N controller, the tests with period times 300, 150, and 90 seconds do not need to be repeated for FCR-D.

The open-loop results in $F(j\omega)$ are used to calculate theoretical closed-loop behavior. The closed-loop system is represented in Figure A.9. The system $G(s)$ is represented by the swing equation (2.11), and is scaled to represent the entire grid. The scaling and parameters of $G(s)$ depend on FCR product and whether stability or performance is to be evaluated. The input d_P represents a load disturbance.

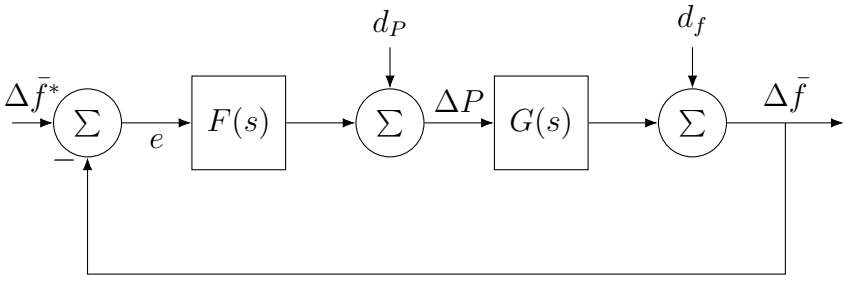

Figure A.9: Block diagram of the closed loop control system for FCR.

The open-loop transfer function from e to $\Delta\bar{f}$ is $G_o(s) = F(s)G(s)$. It is used to evaluate the stability of the closed-loop system. This is done using a Nyquist diagram such as in Figure A.10, where $G_o(j\omega)$ is plotted in the complex plane. The closest distance between the Nyquist curve for $G_o(j\omega)$ and the point $(-1, j0)$ is the stability margin, if the curve passes on the right of $(-1, j0)$, and is here represented as R. Since the closest point may be located between the frequencies for which tests are performed, the Nyquist curve is interpolated between the discrete points that are calculated. Requirement 8 mandates that

$$R > 0.95 \cdot 0.43, \tag{A.14}$$

under the condition that the Nyquist curve passes to the right side of $(-1, j0)$.

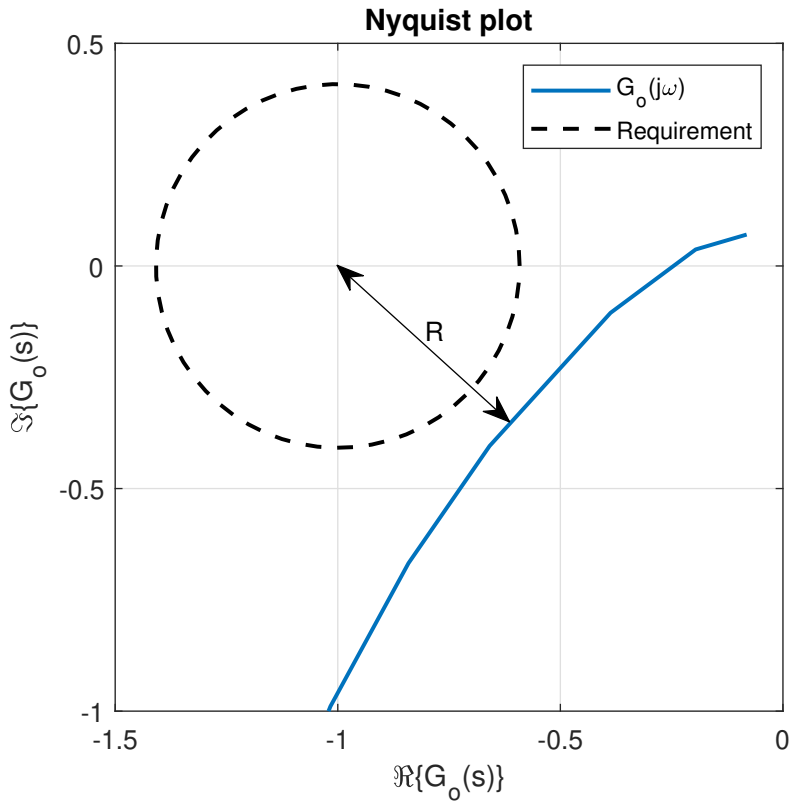

Figure A.10: Nyquist diagram for $G_o(j\omega)$. The distance R is the stability margin, checked in Requirement 8. The Nyquist curve is constructed from the open loop transfer function $\left(G_o(j\omega) = F(j\omega)G(j\omega) = \dfrac{\Delta\bar{f}(j\omega)}{e(j\omega)}\right)$.

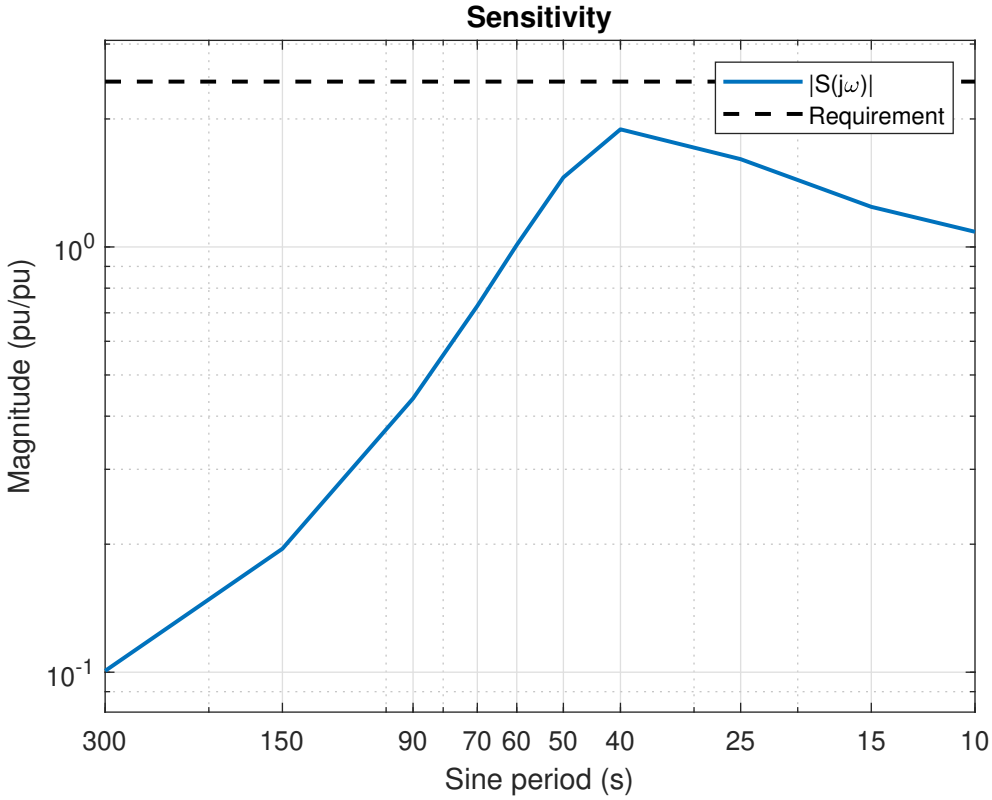

Figure A.11: Sensitivity function, $S(j\omega)$. The peak sensitivity is the inverse of the stability margin. The sensitivity function is the transfer function $\frac{1}{1+F(j\omega)G(j\omega)} = \frac{\Delta\bar{f}}{d_f}$.

For Requirement 9, the closed-loop transfer function from d_P to $\Delta\bar{f}$ is constructed as:

$$G_c(s) = K_{\text{margin}} \cdot \frac{G(s)}{1 + F(s)G(s)}, \tag{A.15}$$

where $K_{\text{margin}} = 0.95$ is a scaling factor used to ease the requirement slightly.

The disturbance d_P is represented as white noise that is low-pass filtered [31]. The low-pass filter is the disturbance profile

$$D(s) = \frac{1}{70s + 1}. \tag{A.16}$$

Requirement 9 represents that no such disturbance should result in a frequency deviation larger than 0.1 Hz [31], which due to the scaling of the transfer function can be expressed as:

$$|G_c(j\omega)| \leq \left| \frac{1}{D(j\omega)} \right| \forall\omega. \tag{A.17}$$

If the requirement is not met, a reduction factor may be applied such that

$$K_{\text{red,dyn}} \cdot K_{\text{margin}} \cdot \left|\frac{G(s)}{1+F(s)G(s)}\right| \leq \left|\frac{1}{D(j\omega)}\right| \forall\omega. \tag{A.18}$$

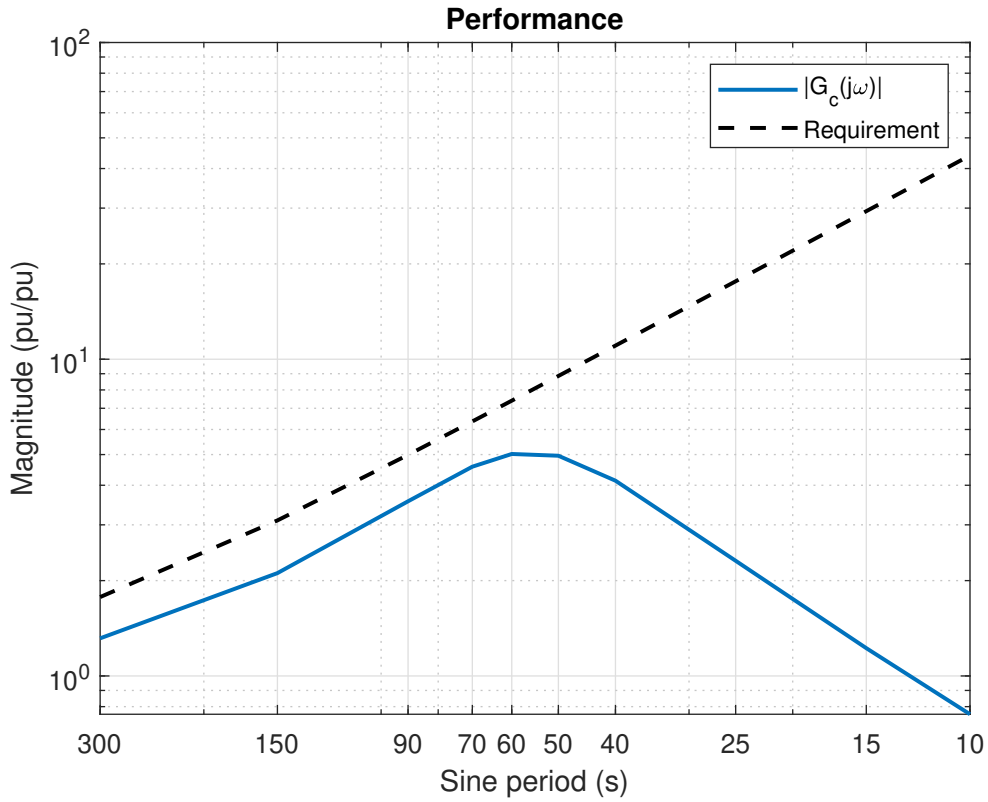

Figure A.12: Disturbance suppression, $G_c(j\omega)$, used to evaluate Requirement 9. $\left(G_c(j\omega) = \frac{G(j\omega)}{1+F(j\omega)G(j\omega)} = \frac{\Delta\bar{f}(j\omega)}{d_P(j\omega)}\right)$.

B

Specification of Prequalification Tests

In this appendix, the settings for all simulated prequalification tests are presented. All tests were simulated with a hydraulic head of 33.4 m, the mean head during the real-world tests.

Table B.1: Simulated prequalification tests.

No.	Product	Test type	Load	Droop	Period time (s)	Initial GV	Droop value	Note
1	FCR-N	Step	Low	Low		0.60	1.33%	
2			Low	High		0.50	4%	
3			High	Low		0.70	1.33%	[1]
4			High	High		0.65	1.33%	

[1] Endurance test. This is the most challenging combination of load and droop.

No.	Product	Test type	Load	Droop	Period time (s)	Initial GV	Droop value	Note
5	FCR-N	Sine	Challenging	High	300	0.75	4%	
6					150			
7					90			
8					70			
9					60			
10					50			
11					40			
12					25			
13					15			
14					10			
15	FCR-D Down	Sine	Challenging	Low	300	0.65	4%	[1]
16					150			[1]
17					90			[1]
18					70			
19					60			
20					50			
21					40			
22					25			
23					15			
24					10			

[1] Simulation only. These tests do not have to be repeated since the same controller parameters as FCR-N are used.

No.	Product	Test type	Load	Droop	Period time (s)	Initial GV	Droop value	Note
25	FCR-D Down	Ramp	Low	Low		0.65	4%	
26			Low	High		0.60	8%	[2]
27			High	Low		0.75	4%	[3]
28			High	High		0.75	8%	[2]
29	FCR-D Up	Ramp	Low	Low		0.45	4%	
30			Low	High		0.45	8%	[2]
31			High	Low		0.62	4%	[3]
32			High	High		0.70	8%	[2]

[2]Combination of FCR-D and FCR-N. FCR-N active with droop 4%

[3]Endurance test. This is the most challenging combination of load and droop.

XVI

C

Complete Results from Prequalification Simulations and Measurements

Table C.1: Descriptions of the columns in the tables of this section.

Notation	Description
Measurement	The measurements from real-world tests.
Sim A	Uses the estimated parameters for the guide vane and runner servos. The low-pass filter estimated in section 4.2.6 ($F_{\text{comp}}(s)$) is not used.
Sim B	Uses the estimated parameters for the guide vane servo. Uses default (mean of possible domains seen in Table 3.3) parameters for the runner servo. The low-pass filter estimated in section 4.2.6 ($F_{\text{comp}}(s)$) is not used.
Sim C	Uses the estimated parameters for the guide vane and runner servos. The low-pass filter estimated in section 4.2.6 ($F_{\text{comp}}(s)$) is implemented on the input to the waterways block, $\bar{G}$, with a time constant $T_{\text{comp}} = 1.2387\,\text{s}$.

C.1 FCR-N Step Tests

Table C.2: Complete results for FCR-N step tests. Further specification of test conditions in Appendix B.

			Captured value (MW)					Requirement 1			
Direction	Load	Droop	Theoretical	Measurement	Sim A	Sim B	Sim C	Measurement	Sim A	Sim B	Sim C
Upwards	Low	Low	10.465	9.068	10.176	10.176	10.176	Fail	Pass	Pass	Pass
	Low	High	3.011	3.168	2.819	2.821	2.819	Pass	Fail	Fail	Fail
	High	Low	11.700	10.667	11.460	11.467	11.460	Fail	Pass	Pass	Pass
	High	High	3.343	2.844	3.092	3.092	3.092	Fail	Fail	Fail	Fail
Downwards	Low	Low	10.465	9.797	8.905	8.905	8.905	Fail	Fail	Fail	Fail
	Low	High	3.011	2.623	2.777	2.777	2.777	Fail	Fail	Fail	Fail
	High	Low	11.700	10.154	9.662	9.663	9.662	Fail	Fail	Fail	Fail
	High	High	3.343	3.344	3.134	3.131	3.134	Pass	Fail	Fail	Fail

C.2 FCR-D Ramp Tests

Table C.3: Complete results for FCR-D steady-state tests, ΔP_{ss}. Further specification of test conditions in Appendix B.

			Captured value (MW)					Requirement 1			
Direction	Load	Droop	Required	Measurement	Sim A	Sim B	Sim C	Measurement	Sim A	Sim B	Sim C
Upwards	Low	Low	12.485	13.372	12.076	12.075	12.076	Pass	Pass	Pass	Pass
	Low	High	6.132	6.715	5.654	5.651	5.654	Pass	Fail	Fail	Fail
	High	Low	14.968	14.600	14.486	14.488	14.486	Pass	Pass	Pass	Pass
	High	High	7.963	7.705	7.425	7.431	7.425	Pass	Fail	Fail	Fail
Downwards	Low	Low	12.485	13.427	12.075	12.074	12.075	Pass	Pass	Pass	Pass
	Low	High	5.978	6.197	5.597	5.599	5.597	Pass	Fail	Fail	Fail
	High	Low	13.587	12.662	13.107	13.109	13.107	Fail	Pass	Pass	Pass
	High	High	6.728	6.474	6.227	6.225	6.227	Pass	Fail	Fail	Fail
Upwards	Low	High	3.120	3.049	3.160	3.162	3.160	Pass	Pass	Pass	Pass
(combined)	High	High	3.936	3.329	3.990	3.990	3.990	Fail	Pass	Pass	Pass
Downwards	Low	High	3.271	4.076	3.195	3.193	3.195	Fail	Pass	Pass	Pass
(combined)	High	High	3.905	2.972	3.872	3.873	3.872	Fail	Pass	Pass	Pass

Table C.4: Complete results for FCR-D fast ramp tests, $\Delta P_{7.5\text{s}}$. Further specification of test conditions in Appendix B.

			Captured value (MW)					Requirement 2			
Direction	Load	Droop	Required	Measurement	Sim A	Sim B	Sim C	Measurement	Sim A	Sim B	Sim C
Upwards	Low	Low	10.737	8.229	11.107	12.382	9.286	Fail	Pass	Pass	Fail
	Low	High	5.274	6.457	6.873	6.965	5.676	Pass	Pass	Pass	Pass
	High	Low	12.872	7.744	12.087	14.360	9.766	Fail	Fail	Pass	Fail
	High	High	6.848	5.446	8.394	8.483	6.735	Fail	Pass	Pass	Fail

			Captured value (MW)					Requirement 2			
Direction	Load	Droop	Required	Measurement	Sim A	Sim B	Sim C	Measurement	Sim A	Sim B	Sim C
Downwards	Low	Low	10.737	9.675	12.371	11.977	11.534	Fail	Pass	Pass	Pass
	Low	High	5.141	5.658	5.577	5.572	5.222	Pass	Pass	Pass	Pass
	High	Low	11.685	9.003	14.908	13.711	13.258	Fail	Pass	Pass	Pass
	High	High	5.786	6.098	7.677	7.620	6.604	Pass	Pass	Pass	Pass

Table C.5: Complete results for FCR-D fast ramp tests, $E_{7.5s}$. Further specification of test conditions in Appendix B.

			Captured value (MWs)					Requirement 3			
Direction	Load	Droop	Theoretical	Measurement	Sim A	Sim B	Sim C	Measurement	Sim A	Sim B	Sim C
Upwards	Low	Low	39.951	22.464	35.351	39.016	23.925	Fail	Fail	Fail	Fail
	Low	High	19.623	15.483	20.468	21.032	13.466	Fail	Pass	Pass	Fail
	High	Low	47.897	20.261	33.868	39.005	21.891	Fail	Fail	Fail	Fail
	High	High	25.482	11.449	21.690	22.520	13.407	Fail	Fail	Fail	Fail
Downwards	Low	Low	39.951	29.458	45.162	42.652	30.819	Fail	Pass	Pass	Fail
	Low	High	19.129	16.870	20.916	20.696	14.434	Fail	Pass	Pass	Fail
	High	Low	43.478	25.171	48.482	44.155	31.956	Fail	Pass	Pass	Fail
	High	High	21.531	14.640	23.251	22.617	15.036	Fail	Pass	Pass	Fail

Table C.6: Complete results for FCR-D deactivation tests. Further specification of test conditions in Appendix B.

			Captured value (MWs)					Requirement 4			
Direction	Load	Droop	Theoretical	Measurement	Sim A	Sim B	Sim C	Measurement	Sim A	Sim B	Sim C
Upwards	Low	Low	21.224	33.880	20.872	21.251	39.114	Fail	Pass	Fail	Fail
	Low	High	10.425	24.403	10.573	10.265	22.990	Fail	Fail	Pass	Fail
	High	Low	25.445	52.891	33.094	36.455	63.316	Fail	Fail	Fail	Fail
	High	High	13.537	63.764	23.918	23.596	63.499	Fail	Fail	Fail	Fail
Downwards	Low	Low	21.224	37.437	20.018	18.410	46.024	Fail	Pass	Pass	Fail
	Low	High	10.162	20.786	9.428	9.727	21.907	Fail	Pass	Pass	Fail
	High	Low	23.098	36.670	23.809	24.198	62.525	Fail	Fail	Fail	Fail
	High	High	11.438	29.335	12.296	12.802	33.318	Fail	Fail	Fail	Fail

C.3 Sine Tests

Table C.7: Frequency domain requirements for FCR-N and downward FCR-D, stability and performance. In order to pass the stability requirement (8), the stability margin must be over $0.43 \cdot 0.95$. In order to pass the performance requirement (9), the performance margin must be over 0.

			Performance/stability margin				Requirement			
Product	Requirement	No.	Measurement	Sim A	Sim B	Sim C	Measurement	Sim A	Sim B	Sim C
FCR-N	Stability	8	0.41	0.43	0.43	0.24	Pass	Pass	Pass	Fail
	Performance	9	-0.24	0.28	0.28	0.15	Fail	Pass	Pass	Pass
FCR-D down	Stability	8	0.46	0.65	0.65	0.52	Pass	Pass	Pass	Pass
	Performance	9	0.29	0.26	0.26	0.26	Pass	Pass	Pass	Pass

Table C.8: Frequency response from FCR-N and downward FCR-D sine tests. Further specification of test conditions in Appendix B. Equivalent to the transfer function from frequency error to active power $\left(\frac{P(j\omega)}{e(j\omega)}\right)$.

			Amplitude (MW)				Phase (degrees)			
Product	Load (pu)	Period (s)	Measurement	Sim A	Sim B	Sim C	Measurement	Sim A	Sim B	Sim C
FCR-N	0.75	300	2.353	3.117	3.117	3.116	-46.2	-39.0	-39.0	-40.4
		150	1.447	2.129	2.128	2.126	-63.5	-54.9	-54.9	-57.9
		90	0.961	1.462	1.462	1.456	-71.7	-62.9	-62.9	-67.9
		70	0.766	1.215	1.215	1.208	-74.4	-65.5	-65.4	-71.8
		60	0.679	1.093	1.093	1.084	-78.0	-66.7	-66.7	-74.1
		50	0.588	0.974	0.974	0.963	-79.0	-68.1	-68.1	-76.9
		40	0.503	0.862	0.862	0.846	-82.6	-69.9	-69.9	-80.9
		25	0.353	0.718	0.718	0.685	-94.2	-76.5	-76.5	-93.8
		15	0.265	0.640	0.640	0.568	-116.8	-92.5	-92.5	-120.0
		10	0.192	0.595	0.596	0.470	-144.6	-114.5	-114.5	-152.4
FCR-D down	0.65	300		2.223	2.222	2.222		-38.3	-38.3	-39.8
		150		1.478	1.479	1.477		-53.5	-53.5	-56.4
		90		0.999	1.000	0.995		-60.5	-60.6	-65.5
		70	0.911	0.826	0.827	0.821	-71.0	-62.4	-62.5	-68.8
		60	0.820	0.740	0.740	0.734	-74.5	-63.2	-63.2	-70.6
		50	0.736	0.656	0.657	0.648	-76.9	-63.8	-63.9	-72.7
		40	0.635	0.579	0.580	0.568	-78.4	-64.6	-64.7	-75.6
		25	0.487	0.481	0.482	0.459	-90.3	-68.5	-68.7	-85.8
		15	0.375	0.424	0.424	0.377	-110.6	-80.0	-80.3	-107.4
		10	0.295	0.386	0.385	0.305	-137.5	-97.6	-97.9	-135.5

Table C.9: Linearity of response in FCR-N and downward FCR-D sine tests. Further specification of test conditions in Appendix B. The values represent root mean square error of the sine fitted to active power, normalized with the standard deviation of the fitted sine itself. Values higher than 1 fail to meet Requirement 10.

			Normalized RMSE				Requirement 10			
Product	Load (pu)	Period (s)	Measurement	Sim A	Sim B	Sim C	Measurement	Sim A	Sim B	Sim C
FCR-N	0.75	300	0.13	0.06	0.06	0.06	Pass	Pass	Pass	Pass
		150	0.15	0.07	0.07	0.07	Pass	Pass	Pass	Pass
		90	0.15	0.08	0.08	0.08	Pass	Pass	Pass	Pass
		70	0.19	0.09	0.09	0.09	Pass	Pass	Pass	Pass
		60	0.19	0.10	0.10	0.09	Pass	Pass	Pass	Pass
		50	0.19	0.11	0.11	0.10	Pass	Pass	Pass	Pass
		40	0.23	0.12	0.12	0.10	Pass	Pass	Pass	Pass
		25	0.33	0.14	0.14	0.11	Pass	Pass	Pass	Pass
		15	0.40	0.17	0.17	0.10	Pass	Pass	Pass	Pass
		10	0.63	0.19	0.19	0.09	Pass	Pass	Pass	Pass
FCR-D down	0.65	300		0.04	0.04	0.04		Pass	Pass	Pass
		150		0.05	0.05	0.05		Pass	Pass	Pass
		90		0.08	0.08	0.07		Pass	Pass	Pass
		70	0.13	0.09	0.09	0.08	Pass	Pass	Pass	Pass
		60	0.14	0.10	0.10	0.09	Pass	Pass	Pass	Pass
		50	0.14	0.11	0.11	0.09	Pass	Pass	Pass	Pass
		40	0.18	0.12	0.12	0.10	Pass	Pass	Pass	Pass
		25	0.25	0.14	0.14	0.10	Pass	Pass	Pass	Pass
		15	0.28	0.16	0.16	0.09	Pass	Pass	Pass	Pass
		10	0.41	0.17	0.18	0.08	Pass	Pass	Pass	Pass

D

Additional Figures and Tables

D.1 Servo Parameter Estimation

Table D.1: Estimation of total GV backlash, i.e. the sum of the servo dead band and the mechanical backlash. Measurements are taken from the real-world FCR-N step tests, at points where the effects of backlash are the greatest in the upward and downward direction respectively. The equivalent change in guide vane position is calculated using interpolation of the approximated turbine characteristic.

Load	Droop	$P_{\text{ss},0}$ (MW)	$P_{\text{ss},3}$ (MW)	ΔP (MW)	Equiv. $\Delta\bar{Y}$ (pu)
Low	Low	27.17	26.47	0.70	0.0101
Low	High	19.70	19.40	0.30	0.0048
High	Low	33.43	32.86	0.57	0.0081
High	High	29.88	29.59	0.29	0.0046
			Total backlash (mean):		0.0069

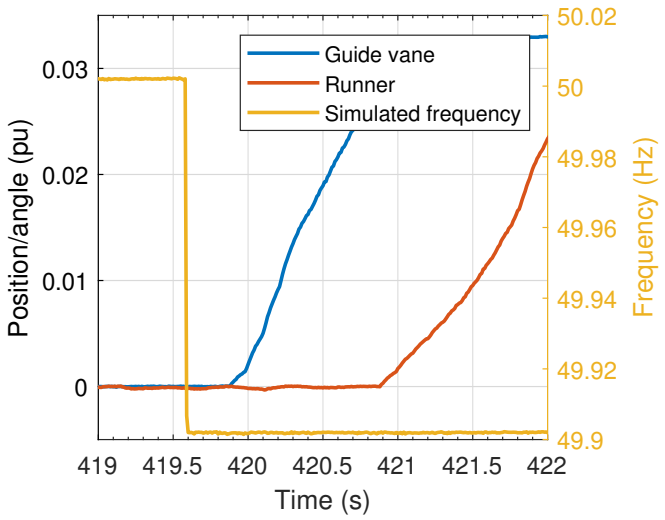

Figure D.1: Estimation of servo input delays during the real-world FCR-N step test with low load and low droop. The first movement of the guide vanes is recorded 0.2 s after the frequency step. The first movement of the runner blades is seen 1.0 s after the first movement of the guide vanes. Only the change in guide vane position/runner blade angle is shown.

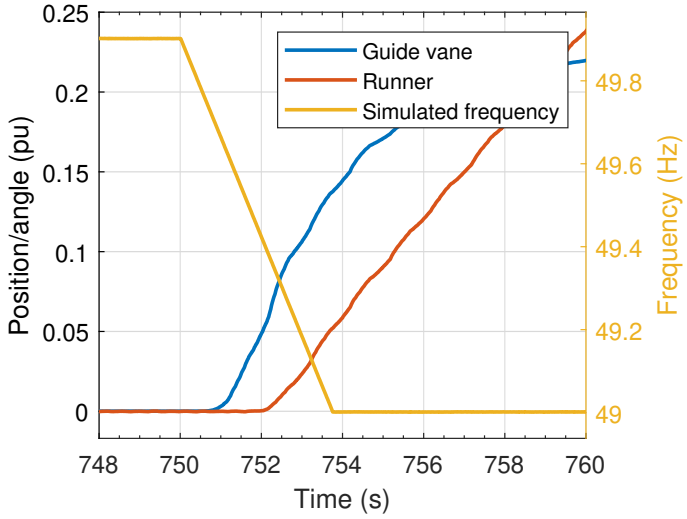

Figure D.2: Estimation of servo rate limits during the real-world upward FCR-D fast ramp test with low load and low droop. The guide vane rate limiter is not obviously saturated during any of the fast ramp tests. The rate limit is therefore conservatively estimated to be the maximum slope seen in the test, 0.05 pu/s. The runner blade angle increases linearly, clearly indicating a saturated rate limiter. The slope is limited to 0.03 pu/s. The same limits were also observed in the downward direction. Only the change in guide vane position/runner blade angle is shown.

D.2 FCR-D Ramps

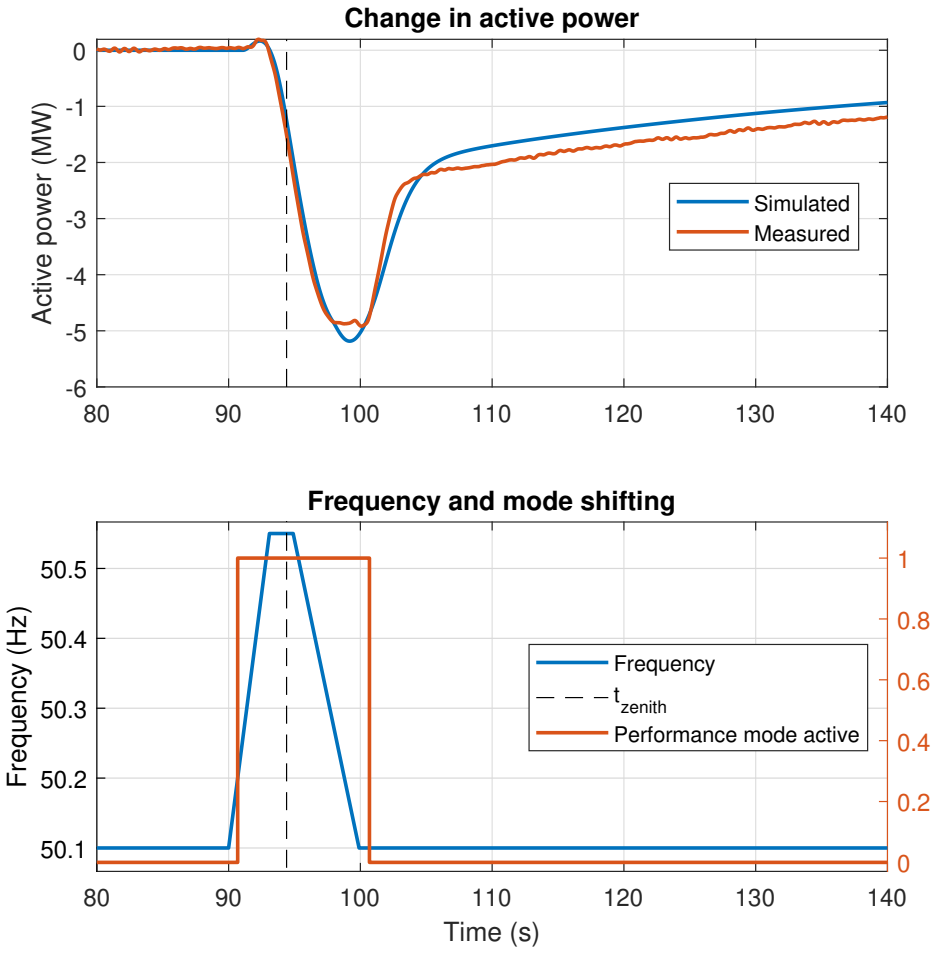

Figure D.3: FCR-D downward deactivation test for high load (initial GV 0.75 pu, ca 33 MW) and high droop (8%). With low-pass filter applied (Sim C). The nominal head of the turbine is 33 m and the nominal power is 48 MW. The actual head is 33.4 m.

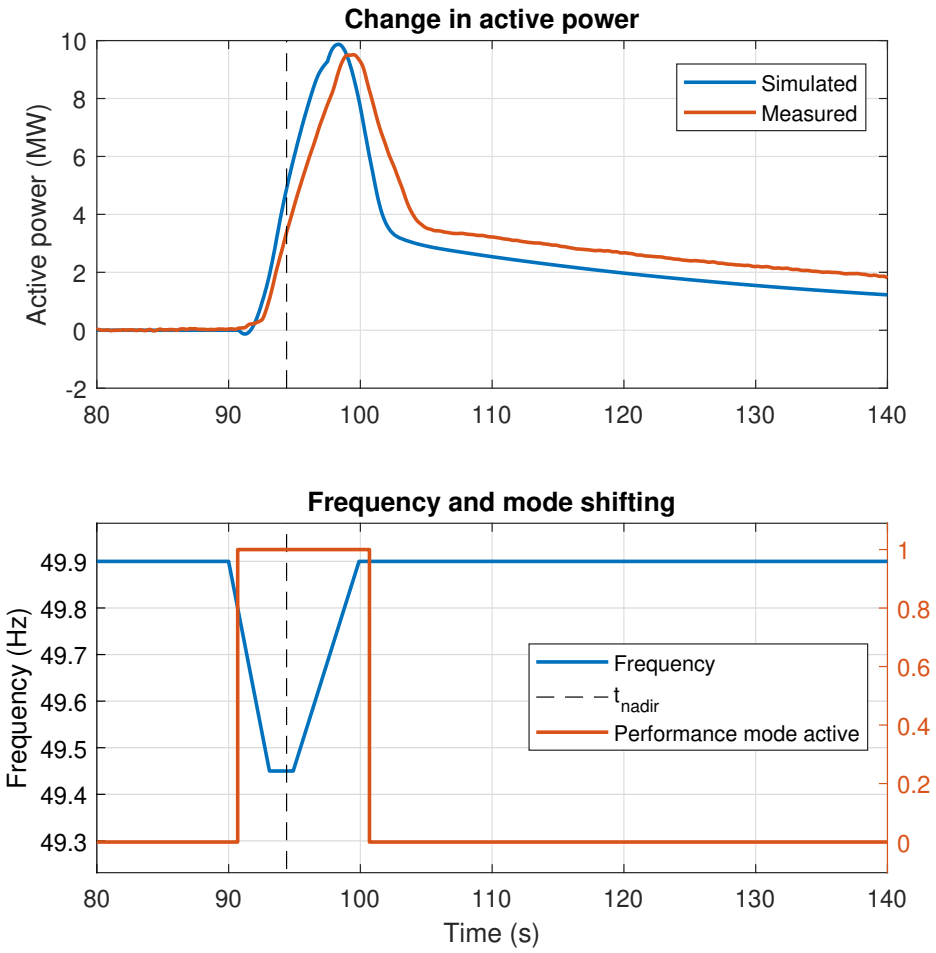

Figure D.4: FCR-D upward deactivation test for low load (initial GV 0.45 pu, ca 17 MW) and high droop (8%). (Sim A). The nominal head of the turbine is 33 m and the nominal power is 48 MW. The actual head is 33.4 m.

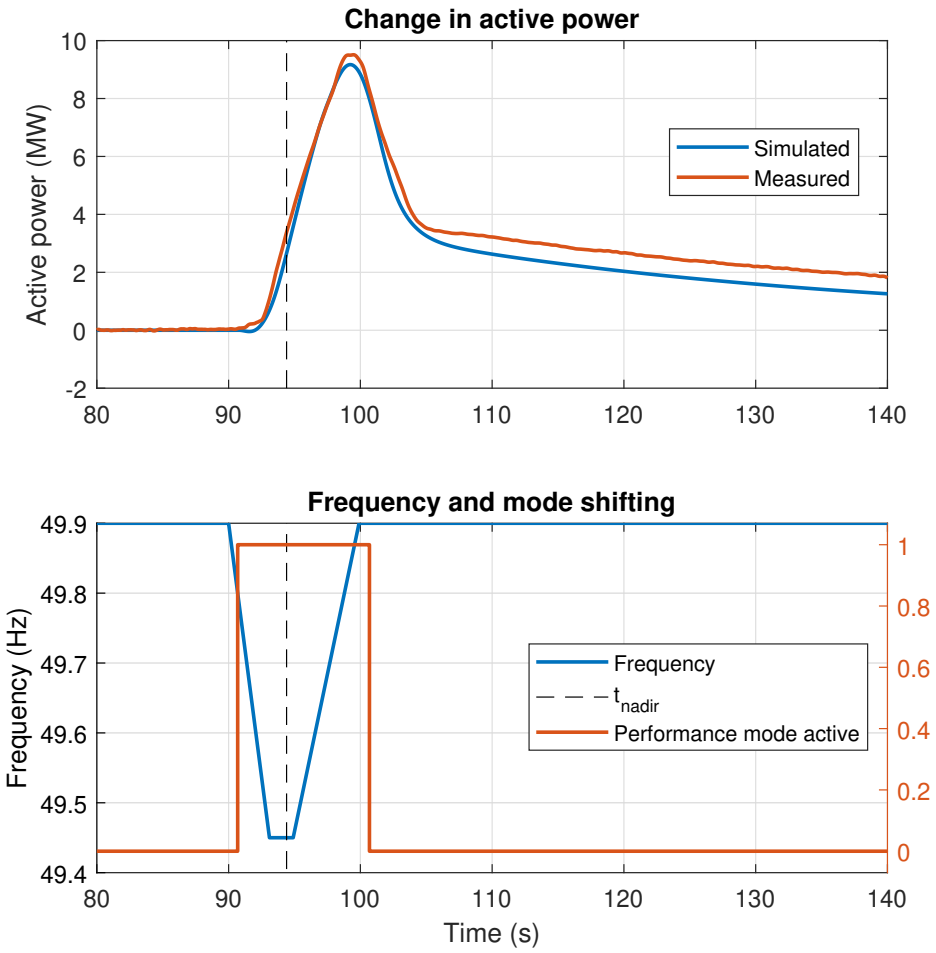

Figure D.5: FCR-D downward deactivation test for low load (initial GV 0.45 pu, ca 17 MW) and low droop (4%). With low-pass filter (Sim C). The nominal head of the turbine is 33 m and the nominal power is 48 MW. The actual head is 33.4 m.

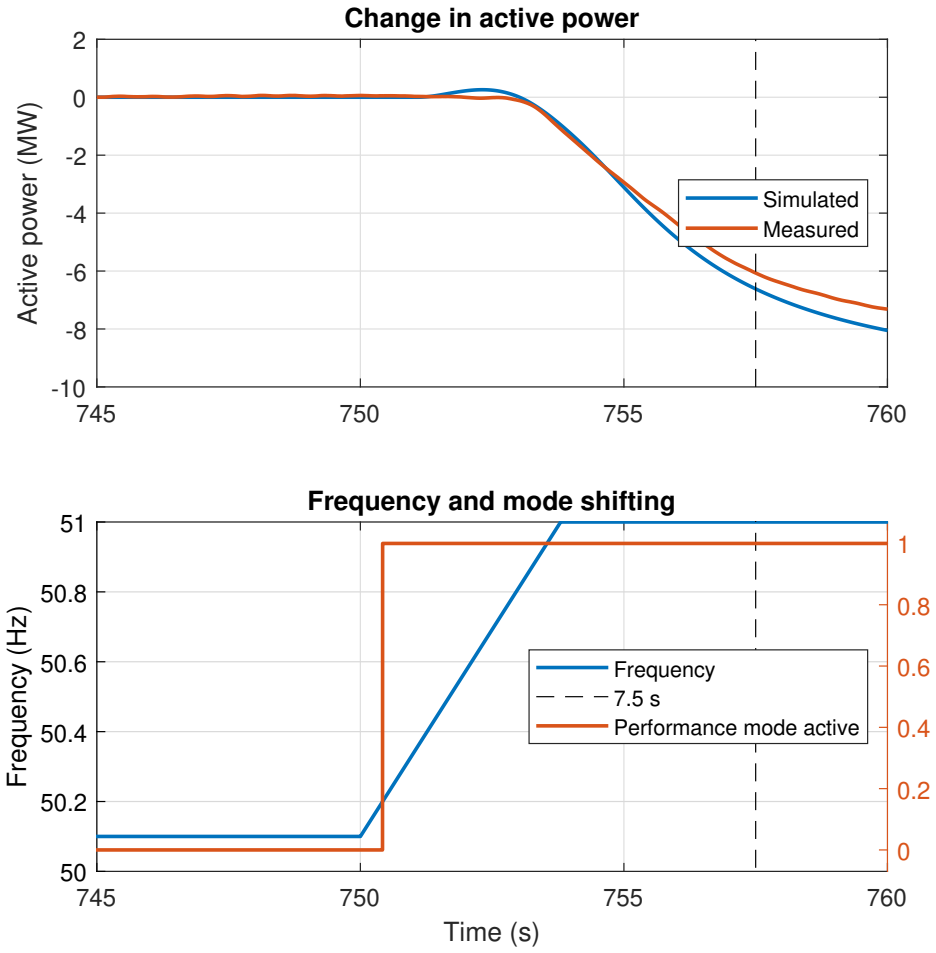

Figure D.6: FCR-D downward fast ramp test for high load (initial GV 0.75 pu, ca 33 MW) and high droop (8%). With low-pass filter applied (Sim C). The nominal head of the turbine is 33 m and the nominal power is 48 MW. The actual head is 33.4 m.

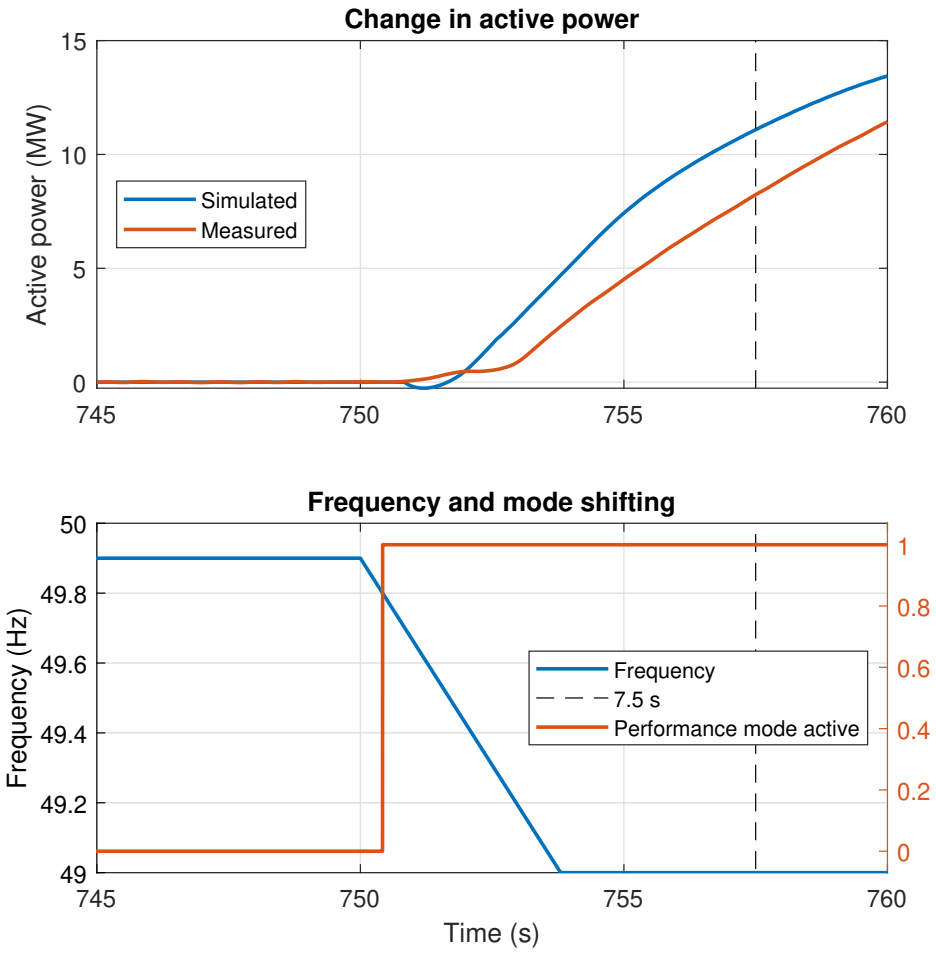

Figure D.7: FCR-D upward fast ramp test for low load (initial GV 0.45 pu, ca 17 MW) and high droop (8%). (Sim A) The nominal head of the turbine is 33 m and the nominal power is 48 MW. The actual head is 33.4 m.

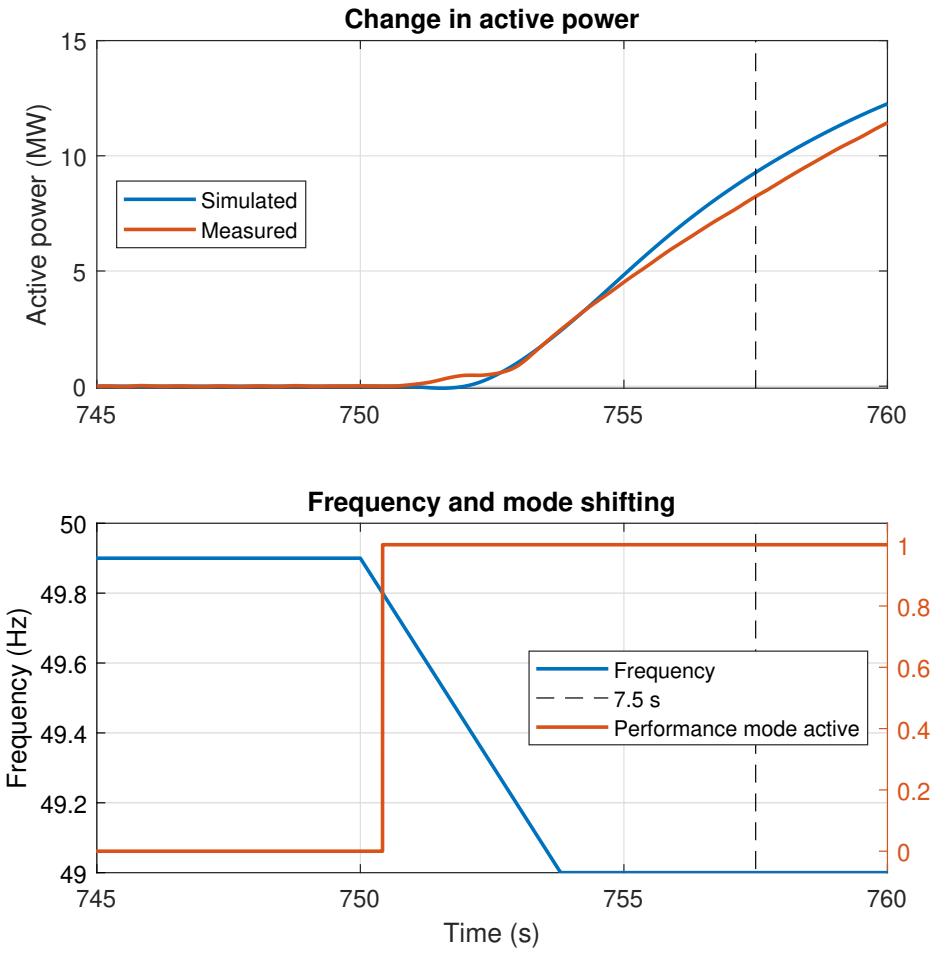

Figure D.8: FCR-D downward fast ramp test for low load (initial GV 0.45 pu, ca 17 MW) and low droop (4%). With low-pass filter (Sim C). The nominal head of the turbine is 33 m and the nominal power is 48 MW. The actual head is 33.4 m.

D.3 Sweeps of Mechanical Backlash

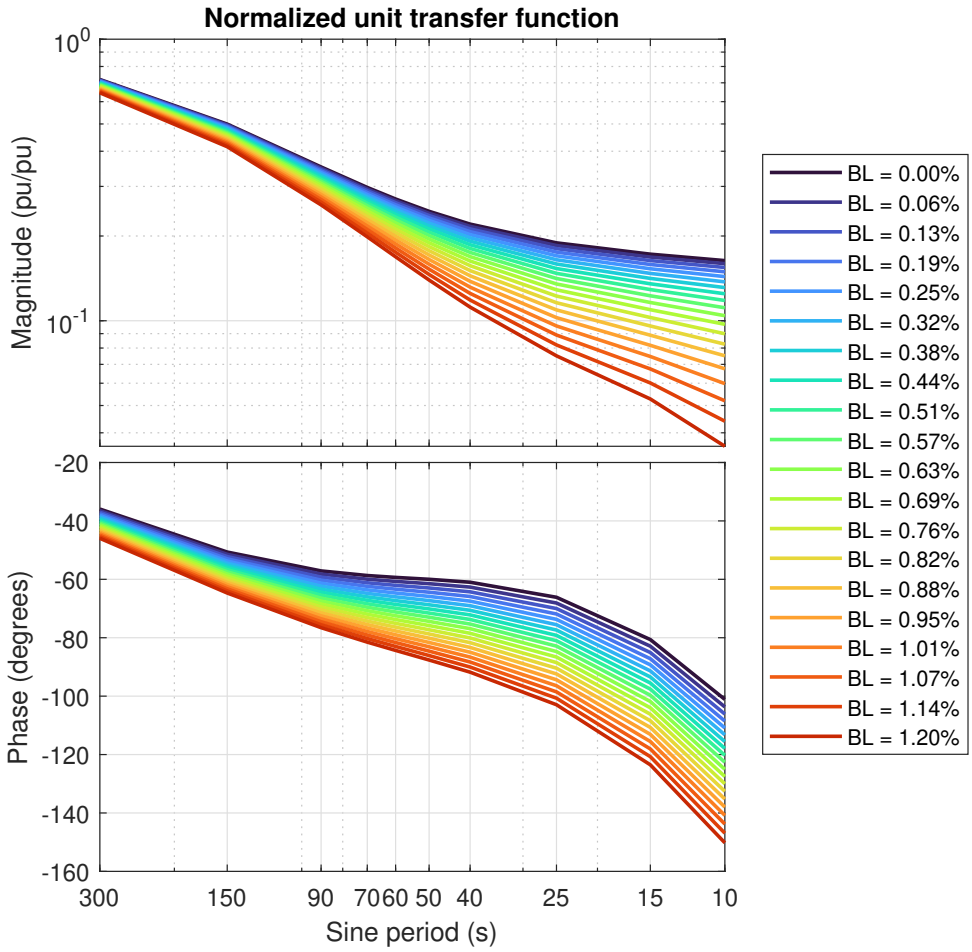

Figure D.9: Simulated frequency response of the unit during FCR-N sine tests for different values of guide vane backlash. The impact of backlash is greatest for the short sine periods, but the effect is significant, especially for the phase, even in the mid-range around 60 s.

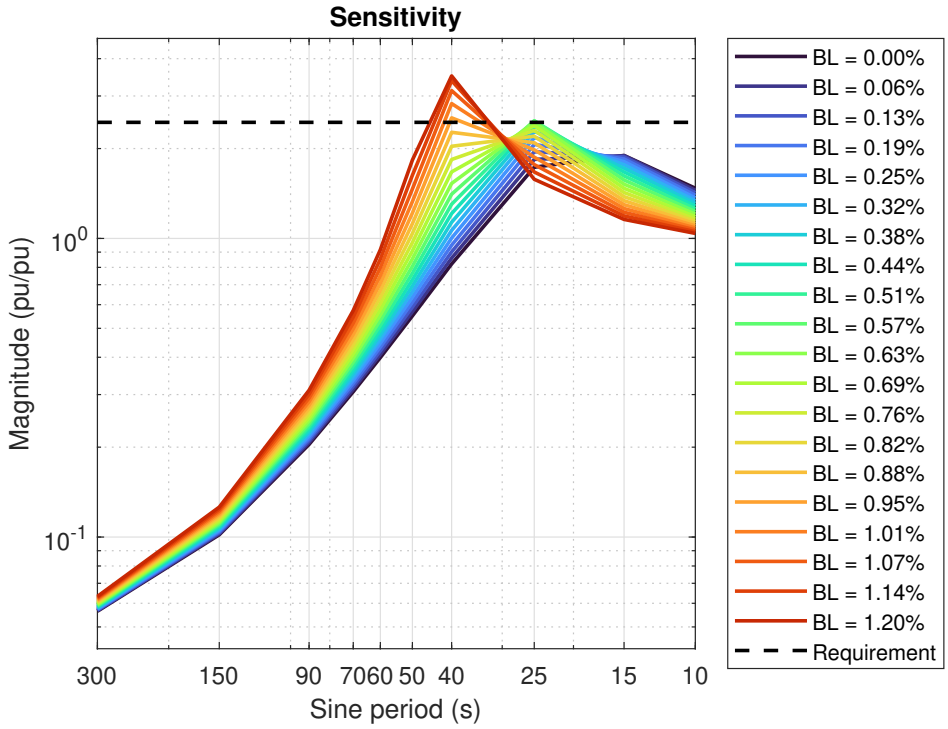

Figure D.10: Sensitivity function for FCR-N for different values of guide vane backlash. The peak sensitivity is increased by backlash, but for the very shortest periods, the sensitivity is reduced when the amplitude is decreased by backlash. The sensitivity function is the transfer function $\frac{1}{1+F(j\omega)G(j\omega)} = \frac{\Delta\bar{f}}{d_f}$.

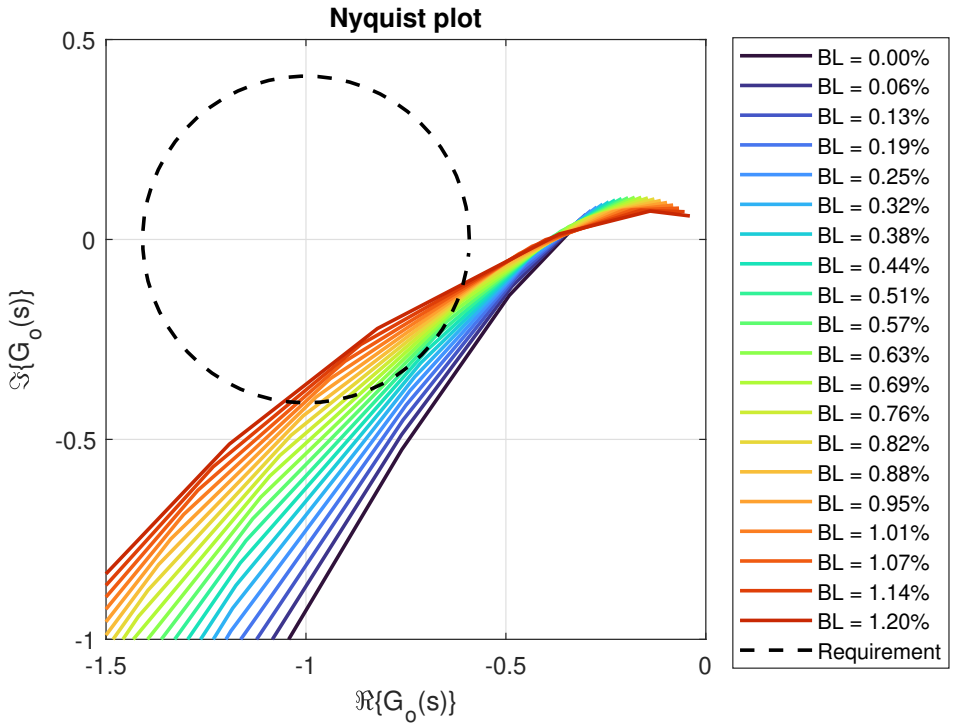

Figure D.11: Nyquist diagram for FCR-N for different values of guide vane backlash. The response near the 40 s period is critical, as seen in the sensitivity function. The stability margin is unambiguously decreased by the backlash.

D.4 Sweeps of Water Time Constant

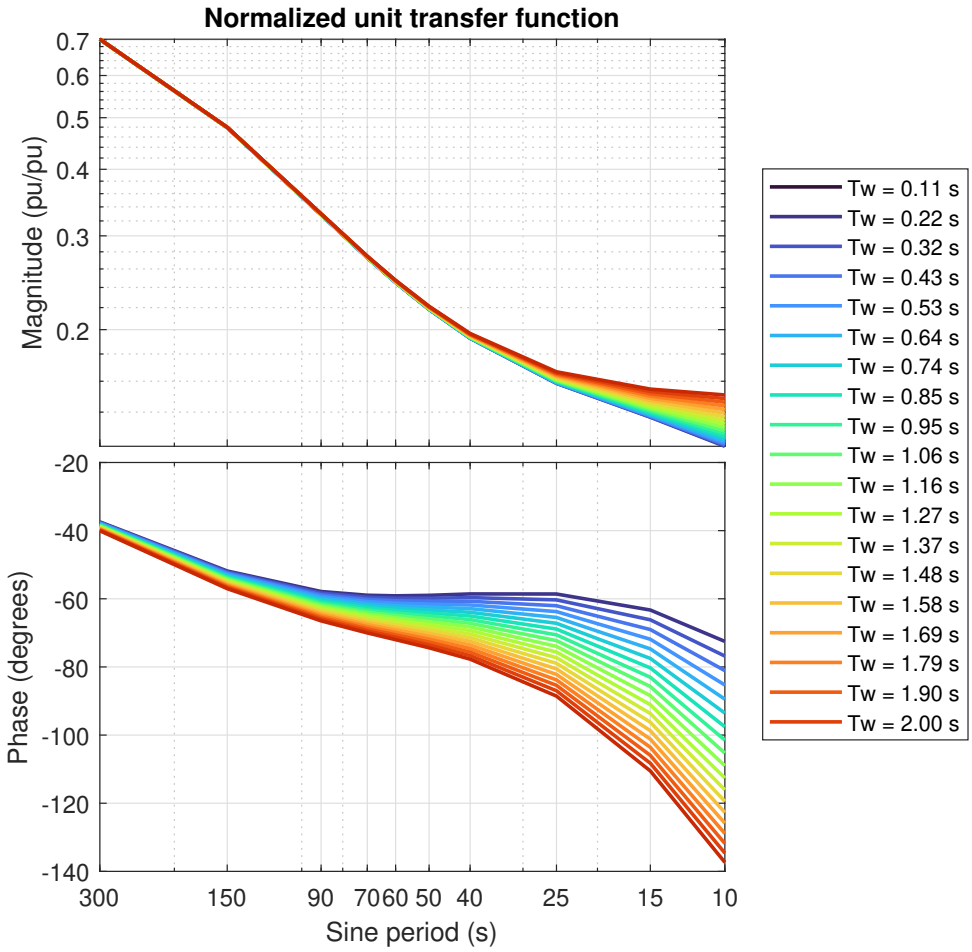

Figure D.12: Simulated frequency response of the unit during FCR-N sine tests for different values of T_W. The amplitude is only affected for very short sine periods. The phase is affected for all periods, but the effect is much greater in the shorter ones.

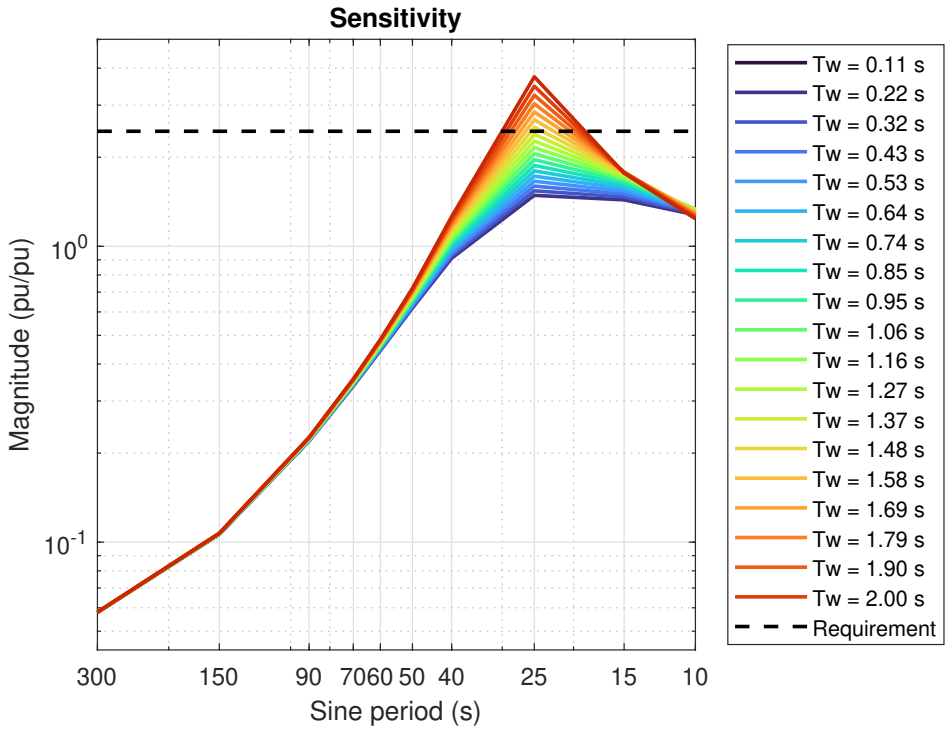

Figure D.13: Sensitivity function for FCR-N for different values of T_W. The sensitivity is most affected near the 25 s period. The sensitivity function is the transfer function $\dfrac{1}{1+F(j\omega)G(j\omega)} = \dfrac{\Delta\bar{f}}{d_f}$.

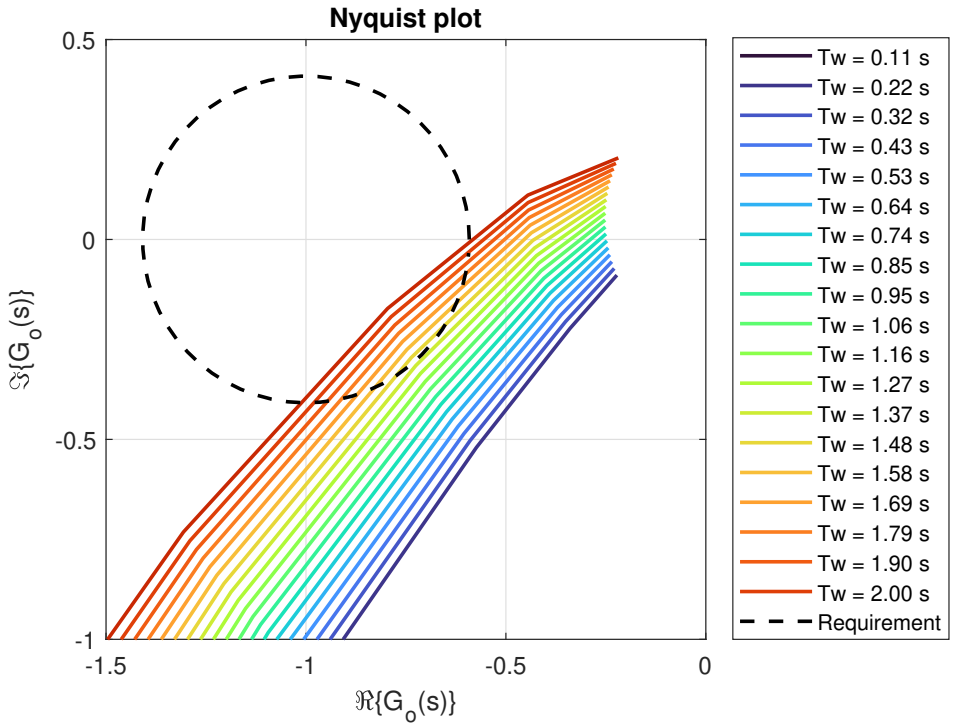

Figure D.14: Nyquist diagram for FCR-N for different values of T_W. As hinted by the sensitivity function, the closest point to -1 is near the 25 s period. The stability margin seems to be affected by T_W in an almost perfectly linear manner.

D.5 Controller Parameter Effects on Frequency Response

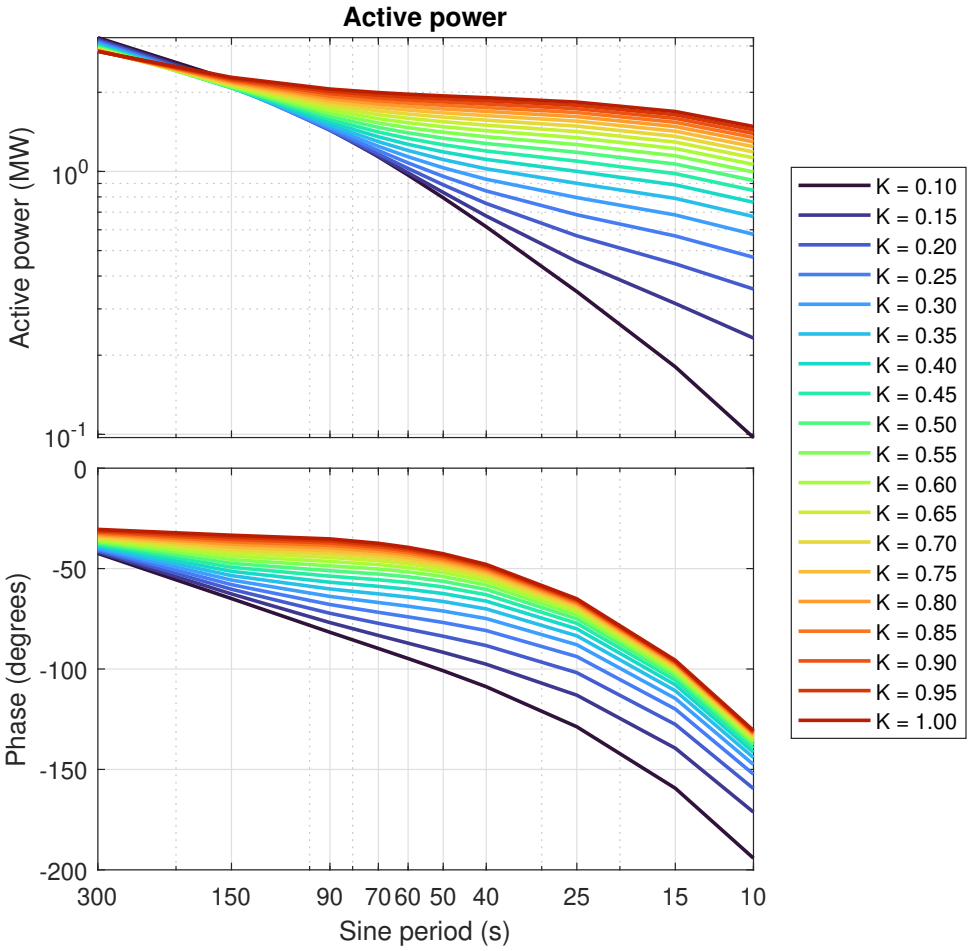

Figure D.15: Simulated frequency response of the unit during FCR-D sine tests for different values of K. T_{feedback} fixed at 31.33 s. Higher proportional gain leads to lower attenuation and phase shift for the short period times.

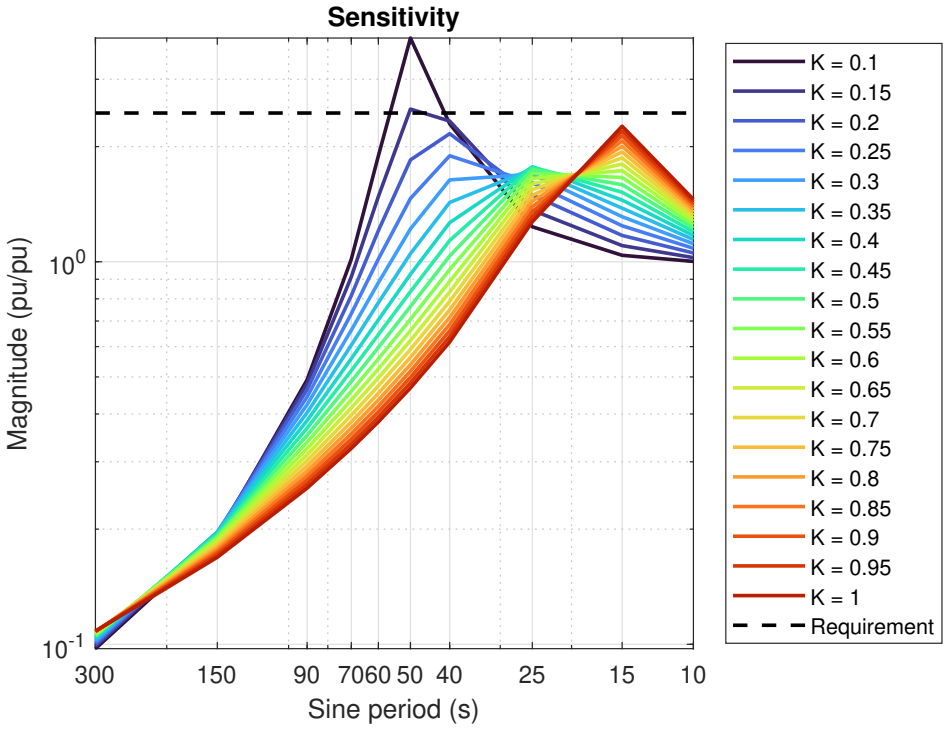

Figure D.16: Sensitivity function for FCR-D for different values of K. T_{feedback} fixed at 31.33 s. Higher proportional gain leads to better damping at intermediate period times, but larger control action at the shortest period times. The sensitivity function is the transfer function $\dfrac{1}{1+F(j\omega)G(j\omega)} = \dfrac{\Delta\bar{f}}{d_f}$.

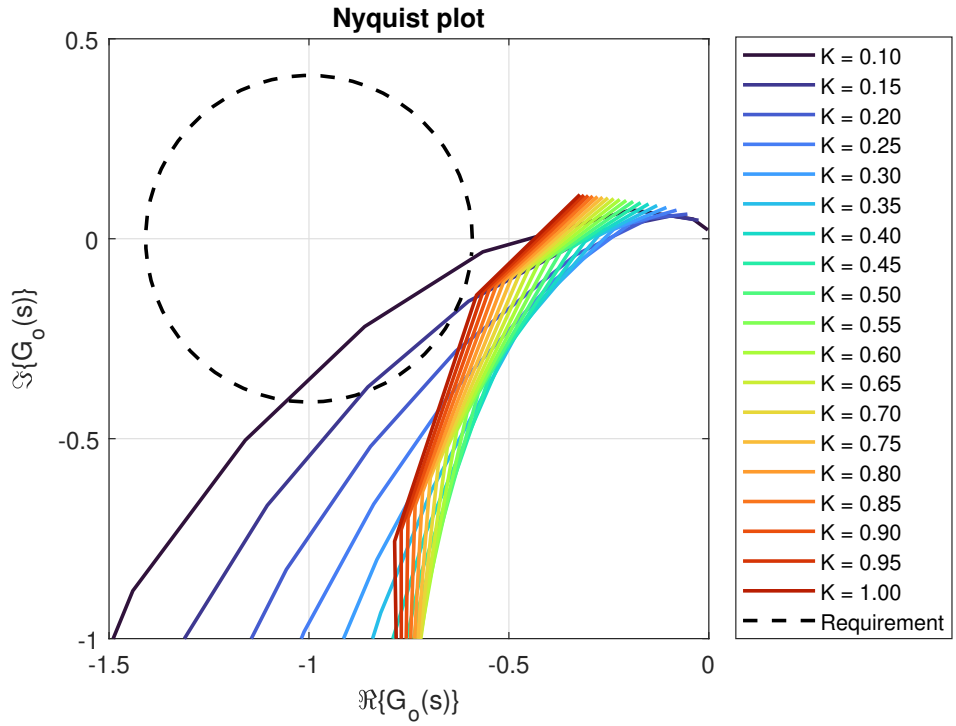

Figure D.17: Nyquist diagram for FCR-D for different values of K. T_{feedback} fixed at 31.33 s. The same effect can be seen as in the sensitivity function.

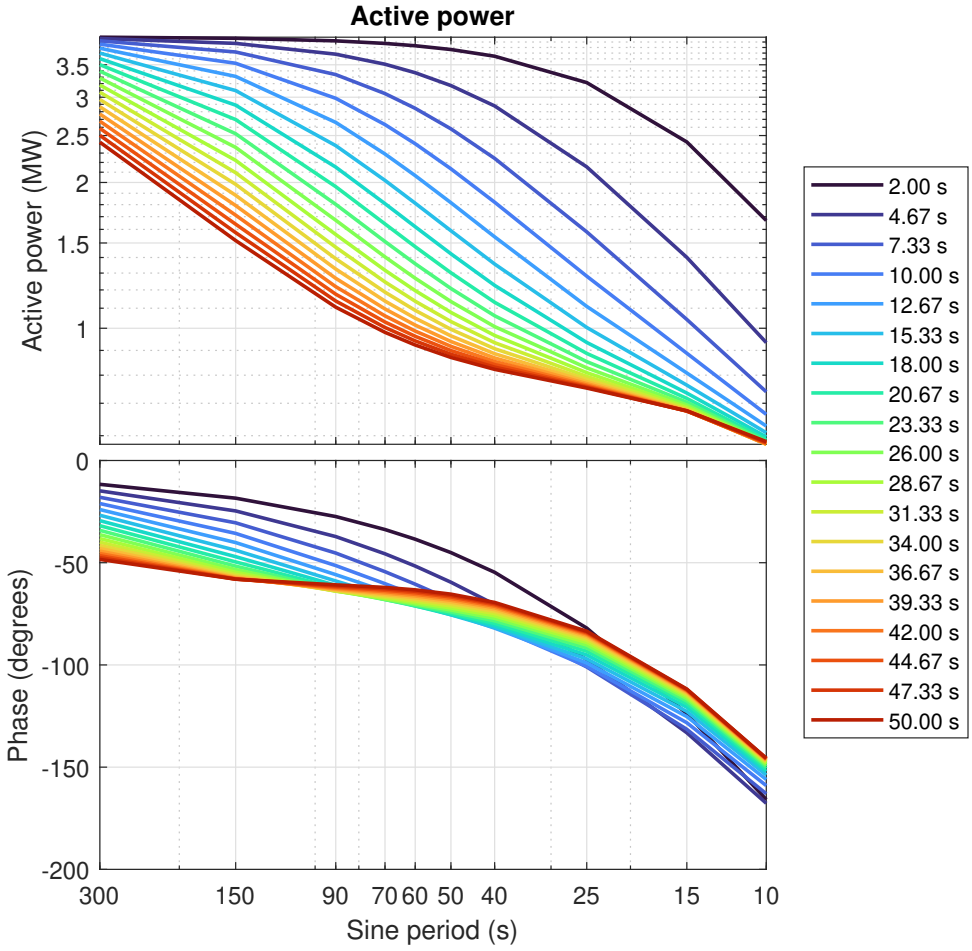

Figure D.18: Simulated frequency response of the unit during FCR-D sine tests for different values of T_{feedback}. K fixed at 0.3. A larger integral action, i.e. lower T_{feedback}, leads to larger amplitudes overall, lower phase shift for the long periods and higher phase shift for the short periods.

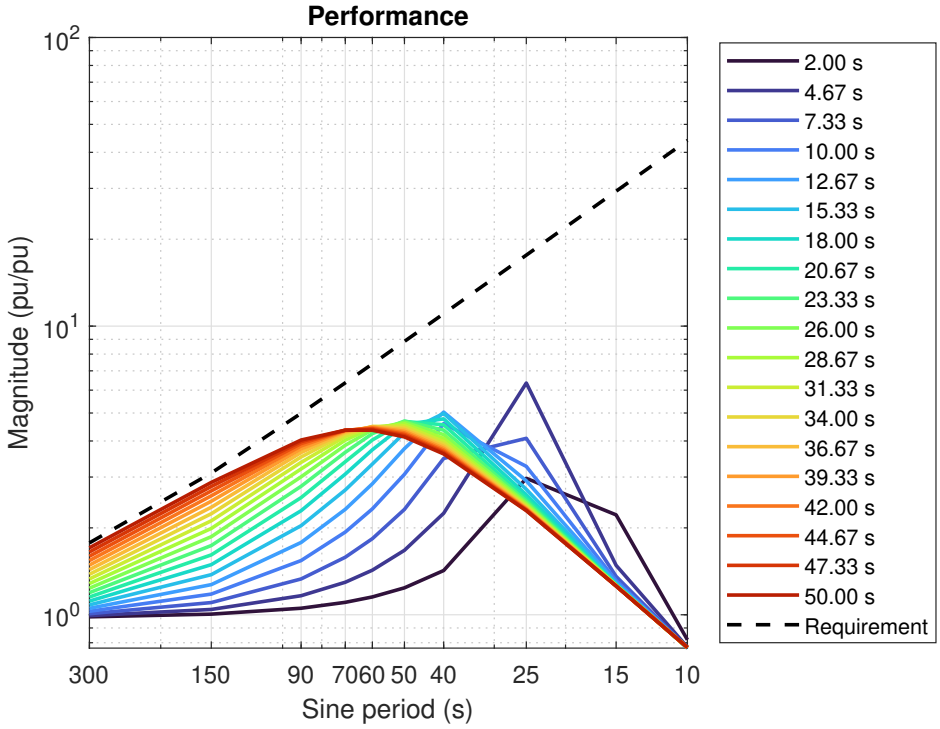

Figure D.19: Disturbance suppression for FCR-D for different values of T_{feedback}. K fixed at 0.3. A larger integral action leads to better disturbance suppression at long and intermediate periods, but introduces peaks at shorter periods. $\left(G_c(j\omega) = \dfrac{G(j\omega)}{1 + F(j\omega)G(j\omega)} = \dfrac{\Delta\bar{f}(j\omega)}{d_P(j\omega)}\right)$.

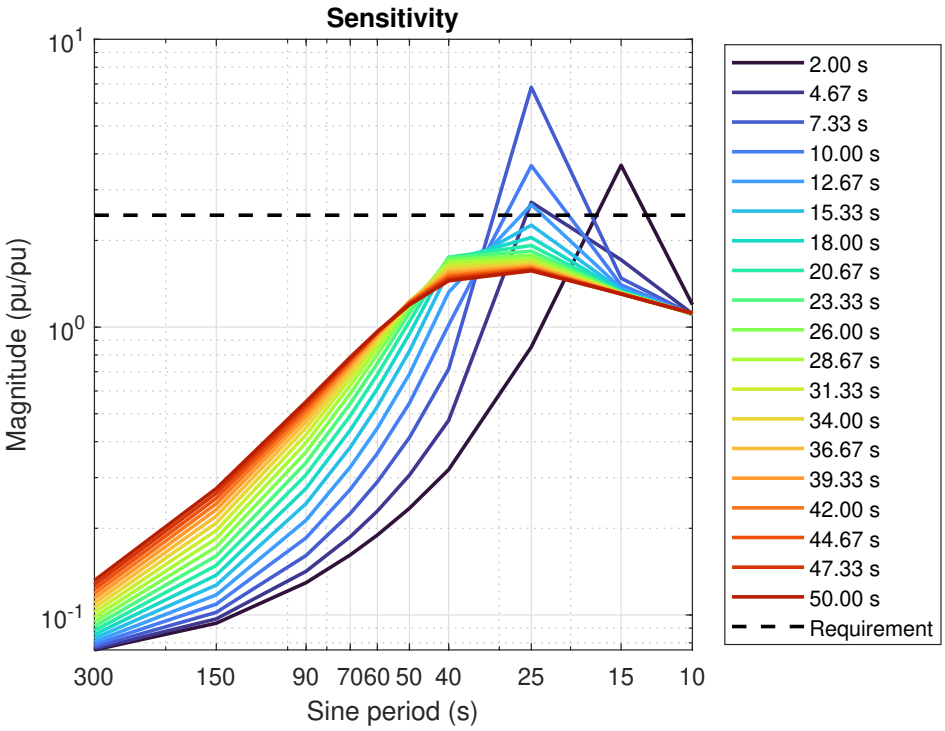

Figure D.20: Sensitivity function for FCR-D for different values of T_{feedback}. K fixed at 0.3. A larger integral action leads to increased sensitivity for the short periods. The sensitivity function is the transfer function $\frac{1}{1+F(j\omega)G(j\omega)} = \frac{\Delta\bar{f}}{d_f}$.

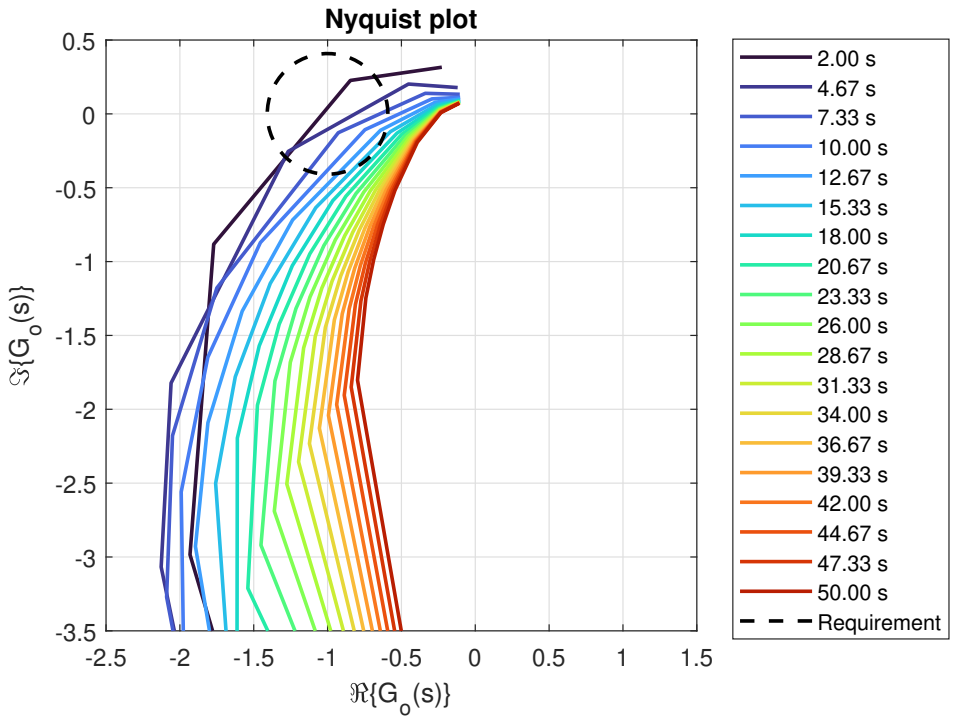

Figure D.21: Nyquist diagram for FCR-D for different values of T_{feedback}. K fixed at 0.3. A larger integral action leads to larger amplitudes and phase delays, and in turn decreased stability margins.

DEPARTMENT OF ELECTRICAL ENGINEERING
CHALMERS UNIVERSITY OF TECHNOLOGY
Gothenburg, Sweden
www.chalmers.se

CHALMERS
UNIVERSITY OF TECHNOLOGY